DETECTION AND IDENTIFICATION OF GREENHOUSE GASES USING INFRARED HYPERSPECTRAL IMAGERY

A THESIS SUBMITTED TO
THE GRADUATE SCHOOL OF INFORMATICS OF
THE MIDDLE EAST TECHNICAL UNIVERSITY
BY

YUSUF GÜR

IN PARTIAL FULFILLMENT OF THE REQUIREMENTS FOR THE DEGREE
OF MASTER OF SCIENCE
IN
THE DEPARTMENT OF INFORMATION SYSTEMS

DECEMBER 2017

DETECTION AND IDENTIFICATION OF GREENHOUSE GASES USING INFRARED HYPERSPECTRAL IMAGERY

Submitted by YUSUF GÜR in partial fulfillment of the requirements for the degree of **Master of Science in Information Systems Department, Middle East Technical University** by,

Prof. Dr. Deniz Zeyrek Bozşahin
Dean, **Graduate School of Informatics** _____

Prof. Dr. Yasemin Yardımcı Çetin
Head of Department, **Information Systems** _____

Prof. Dr. Yasemin Yardımcı Çetin
Supervisor, **Information Systems Dept., METU** _____

Examining Committee Members:

Assoc.Prof. Dr. Banu Günel Kılıç
Information System Dept., METU _____

Prof. Dr. Yasemin Yardımcı Çetin
Information System Dept., METU _____

Assoc.Prof. Dr. Selim Aksoy
Computer Engineering Dept., BİLKENT UNV. _____

Assoc.Prof. Dr. Okan Ertürk
Chemical Engineering Dept., METU _____

Assist.Prof. Dr. Ahmet Güneş
Mechatronics Engineering Dept., ATILIM UNV. _____

Date: *14 December 2017*

I hereby declare that all information in this document has been obtained and presented in accordance with academic rules and ethical conduct. I also declare that, as required by these rules and conduct, I have fully cited and referenced all material and results that are not original to this work.

Name, Last name: Yusuf GÜR

Signature : _____

ABSTRACT

DETECTION AND IDENTIFICATION OF GREENHOUSE GASES USING INFRARED HYPERSPECTRAL IMAGERY

GÜR, YUSUF

MSc., Department of Information Systems

Supervisor: Prof. Dr. Yasemin YARDIMCI ÇETİN

December 2017, 99 pages

Recently, one of the most critical global environment problems is human and ecological exposure to hazardous wastes from urban, agricultural, industrial and military activities. These wastes often include greenhouse gases like water vapor, carbon dioxide, methane, nitrous oxide, ozone and other organic chemicals. To protect the environment from those gases, hyperspectral imaging can be applied due to its ability to extract large amount of spatial and spectral information. Detection of gases emitted into the atmosphere is a widely studied problem. These studies generally use external information about the scene to determine missing parameters in order to detect and identify gases. In this study, unsupervised detection and identification possibility of different greenhouse gases emitted from various sources in selected regions with infrared hyperspectral imagery will be investigated.

Keywords: Gas Detection, Hyperspectral Imagery, Detection & Identification, Greenhouse Gases.

ÖZ

KIZILÖTESİ HİPERSPEKTRAL GÖRÜNTÜLEME KULLANILARAK SERA GAZLARININ TESPİTİ VE TANIMLANMASI

GÜR, YUSUF

Yüksek Lisans, Bilişim Sistemleri Bölümü

Tez Yöneticisi: Prof. Dr. Yasemin YARDIMCI ÇETİN

Aralık 2017, 99 sayfa

Son zamanlarda, insanların ve ekolojinin maruz kaldığı en kritik küresel sorunlardan birisi yaşam alanı, tarım, sanayi ve askeri faaliyetlerden kaynaklanan tehlikeli atıklardır. Bu atıklar genellikle su buharı, karbon dioksit, metan, azot oksit ve ozon gibi sera gazları ve diğer organik kimyasallar içerir. Doğayı korumak için, bu gazların tespiti ve tanımlanması amacıyla sahnenin çok miktarda konumsal ve spektral bilgisini elde etmek için hiperspektral görüntülemeyi kullanabiliriz. Atmosfere yayılan gazların tespiti çokça çalışılmaktadır. Bu çalışmalarda gazların tespit ve tanımlanması amacıyla sahne hakkında dışarıdan elde edilen bilgiler ile eksik parametreleri belirlenmeye çalışılmaktadır. Bu çalışmada, kızılötesi hiperspektral görüntüleri ile seçilen bölgelerdeki, farklı kaynaklardan salınan sera gazlarının tespiti ve tanımlanması imkânı araştırılacaktır.

Anahtar Sözcükler: Gaz Tespiti, Hiperspektral Görüntüleme, Tespit & Tanımlama, Sera Gazları.

To My Lovely Family

ACKNOWLEDGMENTS

First of all, I would like to express my grateful and my respect to my thesis advisor Prof. Dr. Yasemin YARDIMCI ÇETİN for her priceless guidance, encouragement, continuous support to make this research possible.

I also thank my thesis jury members, Assoc. Prof. Dr. Selim AKSOY, Assoc. Prof. Dr. Okan ERTÜRK, Assoc. Prof. Dr. Banu GÜNEL and Assist. Prof. Dr. Ahmet GÜNEŞ for their suggestions and reviewing my work.

Besides my supervisor, special thanks to my friends Didem ÖZIŞIK BAŞKURT and Fatih ÖMRÜUZUN for their endless support, encouragement, technical support and suggestions since the beginning of this research.

I also thank to my friend Dr. Orhan FIRAT for his support during my research. Also, I am thankful to İsa Cem EKEN and Okan Bilge ÖZDEMİR for their support and friendship.

Special thanks to my family for their endless love, moral support and trust.

Also thanks to my lovely unique daughter Yaren GÜR who gave me the feeling of being a father and the meaning of my life.

Finally, I would like to express my deepest gratitude to my wife Sinem Diken GÜR for her love, encouragement and support in all my life. This thesis would not have been written without her.

TABLE OF CONTENTS

LIST OF TABLES

LIST OF FIGURES

LIST OF ABBREVIATIONS

AHI	Airborne Hyperspectral Imager
CBRN	Chemical Biological Radiological and Nuclear
DIRSIG	Digital Imaging and Remote Sensing Image Generation
FIRST	Field-portable Imaging Radiometric Spectrometer Technology
FTIR	Fourier Transform Infrared
IFTS	Infrared Fourier Transform Spectrometer
LWIR	Longwave Infrared
MODTRAN	Moderate Resolution Atmospheric Transmission
MWIR	Mid-wave Infrared
NIST	National Institute of Standards and Technology
PNNL	Pacific Northwest National Labs
SWIR	Shortwave Infrared
UDI	Undersecretariat For Defense Industries
VNIR	Visual and Near Infrared

CHAPTER 1

INTRODUCTION

1.1. Motivation

The developments in sensor technology have enabled hyperspectral sensors operating in different regions of the electromagnetic spectrum with high spectral and spatial resolutions to be utilized in different sectors including quality inspections, remote sensing and biomedicine. Spatial and spectral resolution of these sensors are improving continuously, providing detailed information related to the energy absorption, reflection and emission characteristics of materials present in the scene. In this way, the energy (light or heat) emission or reflection characteristics of objects in the scene can be examined in detail as compared to multispectral or panchromatic sensors.

This information density in the spectral domain increases the automatic identification accuracy of the investigated objects in the scene. In recent years, in addition to solid and liquid substances, examination of compounds in gaseous-form by hyperspectral sensors is an emerging research area. Determination and identification of gaseous compounds especially by infrared hyperspectral imagery is showing high promise. As different gases depict characteristic energy absorption features in the infrared region, identification and quantification of the absorption becomes feasible. These hyperspectral imageries include environmental pollution, greenhouse gases as well as various gases that can be used in CBRN (Chemical, Biological, Radiological and Nuclear) assaults. Hyperspectral imagery, especially obtained from infrared bands, are preferred for gas detection applications as an alternative to in-site analyzes for power plants, the manufacturing industry and the transportation sector due to cost and time advantages.

1.2. Scope of the Thesis

Within the scope of this thesis, detection and identification of pollutants and greenhouse gases with hyperspectral sensors operating in the LWIR and MWIR band is targeted. In spite of liquids and solids radiate different amount of light in VNIR/SWIR region; gases depict different characteristic energy absorption features in the infrared region. Detection, classification and identification of these gases with remote sensing techniques in addition to traditional on-site inspections methods with Hyperspectral imagers operating in LWIR and MWIR are intended. The target gases are Sulfur Hexafluoride (F_6S), Ethylene (C_2H_4), Butane (C_4H_{10}), Methanol (CH_3OH) and Carbon Dioxide (CO_2). Nitrous Oxide (N_2O) a greenhouse gas, is not investigated as we do not have real hyperspectral remote sensing images including Nitrous Oxide. The main objective of this study is to detect and identify mentioned gases automatically on hyperspectral remote sensing images.

1.3. Outline of the Thesis

This document is organized as five chapters including introduction, background, methodology, experiments and conclusion. After general information about gas detection and remote sensing, the aim of this thesis is stated in this chapter. Chapter 2 defines IFTS camera and explains radiance model used in gas detection problems. Chapter 2 also presents the gas detection and identification studies in the literature. Chapter 3 explains the proposed gas detection method in detail. Chapter 4 gives information about data sets and presents the experimental gas detection results by comparing the proposed algorithm and literature. Finally, the research is concluded with a summary of our contributions and future works are mentioned in Chapter 5.

CHAPTER 2

BACKGROUND

2.1. Hyperspectral Imaging

Regular grayscale cameras create images as a function of two spatial coordinates x and y (Intensity). We see the scenes by combining the intensity of appropriate red, green and blue spectral bands in the visible spectrum. Therefore, color scenes consist of the intensity I (x, y, λ) depending on two spatial coordinates and spectral band λ. Multispectral and hyperspectral cameras are providing capability of using more spectral bands for identification of different materials. Actually, there is no explicit difference between hyperspectral and multispectral imagery (see(Hagen & Kudenov, 2013)). Multispectral imagery has more than three and less than ten spectral bands whereas, hyperspectral imagery has more than ten spectral bands which are contiguous. In this thesis, hyperspectral imagery will be used for detection and identification of gases.

Hyperspectral imaging sensors provide data cubes that includes both spectral and spatial information of a scene. These data cubes can be used for detection of targets in many military and civilian applications. Every material reflects, absorbs or emits some amount of radiation (radiance) that varies along a large number of continuous spectral bands. It is aimed to detect target materials by using hyperspectral imagery in appropriate spectral bands. Basically, a hyperspectral imaging systems consist of the radiation source (generally sun), the atmospheric path, the imaged surface and the imaging sensor. With considering sun as a radiation source, sun's emitted energy as a function of wavelength is termed the solar spectrum. The solar energy propagates from sun to the target surface through the atmosphere. This energy interacts with the surface and according to the material it is reflected/transmitted/absorbed. It passes back through the atmosphere and reaches to the imaging sensor where it is converted to the digital form as named radiance spectrum (see in Figure 1).

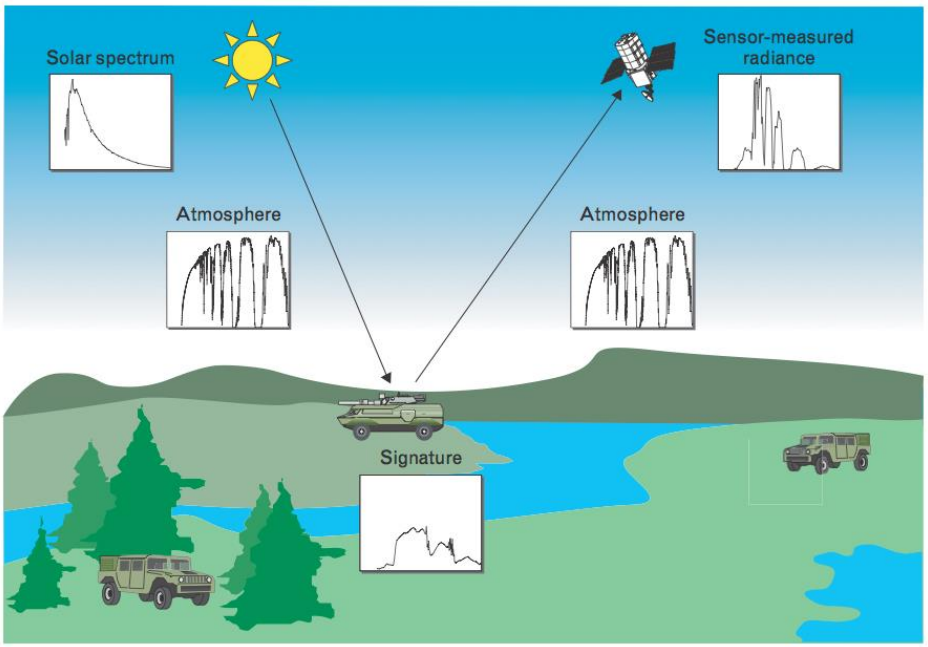

Figure 1 Hyperspectral Imagery (taken from [Manolakis et. al.])

Hyperspectral sensors provide degraded spatial resolution to improve spectral resolution. Therefore, it can be easily used if spectral information of target is more reliable than shape information (see (Manolakis, Marden, & Shaw, 2003)). Hyperspectral data cubes are three-dimensional data structures formed as spatial-spatial-spectral components (see Figure 2). We can plot a single pixel on data cube to get spectral signature or we can visualize a single band to observe specific material view.

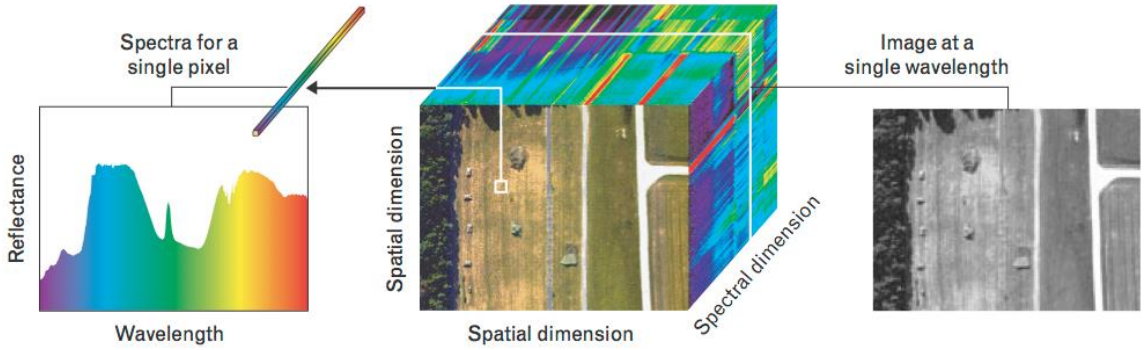

Figure 2 Hyperspectral Data Cube (taken from [Manolakis et. al])

2.2. FTIR

Hyperspectral sensors provide extensive spectral information in the sense of energy emission and reflection characteristics of the targeted objects in different regions of the electromagnetic spectrum. This specialty makes them useful for gas detection applications as well as solid and liquid materials detection issues. Hyperspectral images especially in infrared spectral region is preferable for gas detection problems as gases reveal significant emission and absorption characteristics in these regions.
Information about devices used in hyperspectral remote sensing are mentioned in the literature (see (Hagen & Kudenov, 2013)). Specifically, two types of devices,

operating in mentioned spectral regions, used for detection of gases can be distinguished (see (Systems, Measurement, Mariusz Kastek, Tadeusz Piątkowski, 2011)). One of them is a typical thermal camera additionally equipped with a filter system, thermal camera with a tunable filter or thermal camera and a set of optical filters. The other type is based on Fourier spectroscopy principles. Camera plus filters has constant imaging windows identified by filter amount and has slow operation period through filter rotation issues as disadvantage; on the contrary, if high spectral resolution is not required (dedicated for detecting specific gas) it is a cost-effective solution. Camera with tunable filters has complicated optical design. The product of its resolution and transmission is higher than camera plus filters but lower than Fourier-transform devices. Also, its acquisition rate is higher while its spectral resolution is lower. Fourier-transform devices have comparable resolution with previous types but it has a complicated data processing technique through mainly used for research and development systems.

FTIR devices provide high resolution with equal cost and the absence of mismatches of various color images due to movement of platform in camera with tunable filters. FTIR technique, used to obtain spectral information, is an interference based technique that uses a Michelson interferometer for mixing an incoming signal with the same signal with different discrete time delays and produce an interferogram which is a time domain waveform related to the power spectrum Fourier transform of the scene. The schematic diagram regarding to the used layout of a Michelson interferometer used by Imaging Fourier transform spectroradiometer HyperCam is shown in Figure 3.

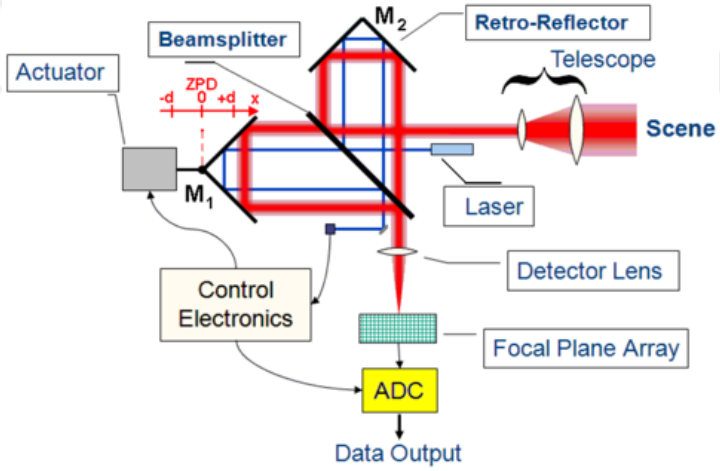

Figure 3 Block diagram of imaging Fourier-transform spectroradiometer. (taken from [Kastek et. al.])

2.2. Radiance Model

2.2.1. Measured Energy At Sensor

In remote sensing problems, there are three ways for calculating a sensor radiance according to energy conservation rules in Kirchhoff Law (see Figure,4-6).

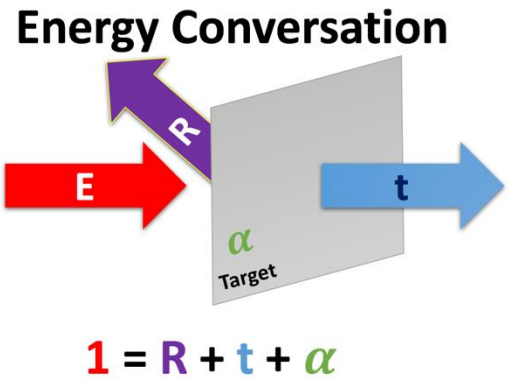

Figure 4 Energy Conversation

Symbol R stands for reflection, symbol t stands for transmission and symbol α stands for absorption where the absorption/emission ratio is constant and expressed by emissivity (ε).

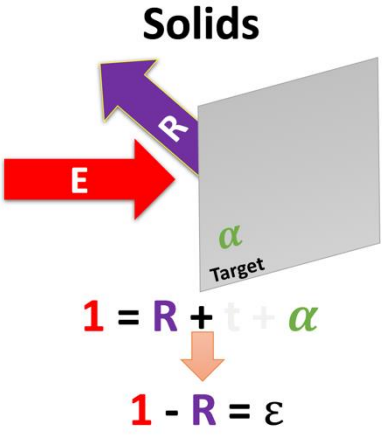

Figure 5 Energy Conversation of Solids

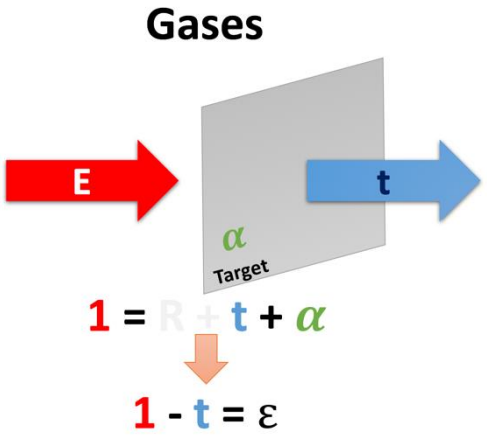

Figure 6 Energy Conversation of Gases

The measurements for gas monitoring applications, implemented in a controlled environment, are capable in obtaining absorbance and transmittance values of target gases. FTIR cameras only collect radiation from the scene occurred by the energy of the vibrating gas molecules, so they are not able to measure these values directly and cannot be directly used in remote sensing applications of gases. We need to obtain the transmittance or absorbance characteristics of the target gases from the radiance data of the scene for the remote sensing of gas purposes.
In this thesis, measurement from a ground-based platform is concerned as physical problem of interest. The model of the gas emission/absorption scene of interest in Figure 7 is given in the literature(see (Tremblay et al., 2010)).

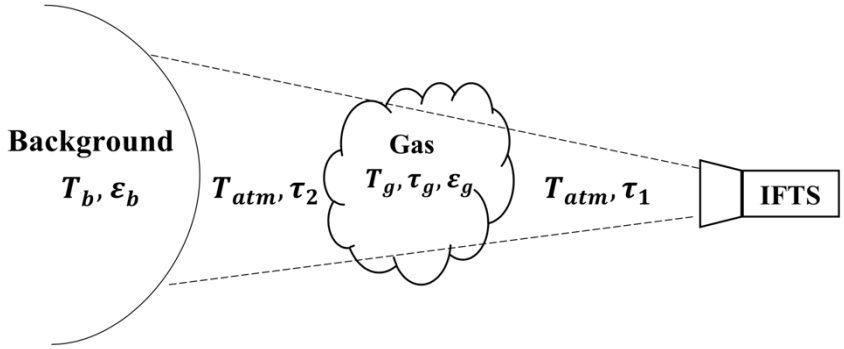

Figure 7 The Gas Radiance Model

The general formula given in the literature is

$$L(\lambda) = L_g(\lambda) + L_{b+g}(\lambda) + L_{atm}(\lambda), \quad (2.1)$$

where: $L(\lambda)$ is the radiance value of the gaseous pixel, $L_g(\lambda)$ is the self-emitted gas plume radiance, $L_{b+g}(\lambda)$ is the self-emitted background radiance through the plume, and $L_{atm}(\lambda)$ is self-emitted atmospheric effects at wavelength λ.

The self-emitted gas plume radiance can be given as:

$$L_g(\lambda) = \tau_1(\lambda)\ \varepsilon_g(\lambda)B(\lambda, T_g), \quad (2.2)$$

where: $\tau_1(\lambda)$ is the transmittance of atmosphere between gas plume and camera, $\varepsilon_g(\lambda)$ is the emissivity value of gas, and $B(\lambda, T_g)$ is the Blackbody Radiance of the gas at temperature value T_g of the gas plume in Kelvin at wavelength λ.

The self-emitted background radiance can be given as:

$$L_{b+g}(\lambda) = \varepsilon_b(\lambda)B(\lambda, T_b)\tau_1(\lambda)\tau_2(\lambda), \quad (2.3)$$

where: $\tau_2(\lambda)$ is the transmittance of atmosphere between background and gas plume, $\varepsilon_b(\lambda)$ is the emissivity value of background, and $B(\lambda, T_b)$ is the Blackbody Radiance of the temperature value T_b of the background in Kelvin at wavelength λ.

According to formulas (2.1 - 2.3) the general radiance formula can be expressed as:

$$L(\lambda) = \tau_1(\lambda)\left[\varepsilon_g(\lambda)B(\lambda, T_g) + \tau_2(\lambda)\tau_g(\lambda)\varepsilon_b(\lambda)B(\lambda, T_b)\right] + L_{atm}(\lambda, T_{atm}) \quad (2.4)$$

Beer's Law

In order to reveal the transmissivity characteristic of the gas, firstly the energy (photon number) emitted from the light source is measured in the absence of gas (I_0), then the gas sample is released between the light source and the detector and amount of the energy coming from the light source reaches to the spectrophotometer is measured. The ratio of these two measurements is called transmissivity.

$$Transmissivity = \frac{\mathrm{I}}{I_0} \quad (2.5)$$

where: I_0 is the value measured by the spectrophotometer without the gas sample, and I is the value measured when the gas sample is present.

The absorption signature of the gas sample can be obtained by using the obtained transmissivity data with the following equation,

$$Absorption = -\log(Transmissivity) \quad (2.6)$$

In addition to all of these, the gas cloud's transmission τ_g can be computed from the spectral properties of the included chemical species with Beers' Law,

$$\tau_g(\lambda) = \exp(-\sum \alpha_i(\lambda) C_i d) \quad (2.7)$$

where: C_i is the average concentration of the targeted chemical compound (i) over the path length d and $\alpha_i(\lambda)$ is the wavenumber-dependent absorption coefficient.

Likewise, we can compute the gas cloud's emissivity ε_g, which is equal to its absorption, with the following equation.

$$\varepsilon_g(\lambda) = 1 - \tau_g(\lambda) \quad (2.8)$$

If the plume is optically-thin, the Beer's law relationship (see (Eq.2.7)), can be calculated by its first-order linear approximation as given below(see(Niu, Golowich, Ingle, & Manolakis, 2011)):

$$\varepsilon_g(\lambda) = 1 - \tau_g(\lambda) = 1 - \exp(-\alpha_i(\lambda) C_i) \quad (2.11)$$

Additionally, thermal equilibrium condition is a very common situation in real world situations (see (Niu, 2013)) as T_p of every plume approaches T_{atm} and they become equal after sufficient time. Moreover, the atmospheric terms are negligible or same for all objects in the scene as the objects in scene are relatively close to the camera and the up welled radiance may be dropped since the term is also minimal(see (Kastek, Piatkowski, & Polakowski, 2011))

The advantages of these assumptions are both efficient and easy to implement for understanding the remote sensing of gas problem. With all of the assumption mentioned above, general equation of gas detection problem (see (Eq.2.4)) becomes:

$$L(\lambda) = \tau_1(\lambda)\left[(1 - \alpha_i(\lambda) C_i d) B(\lambda, T_g) + (\alpha_i(\lambda) C_i d)\varepsilon_b(\lambda) B(\lambda, T_b)\right] \quad (2.12)$$

In gas detection problems, it is important to understand terms given in equation (2.12). Temperature values of background and gas materials are important as gases appear in either emission or absorption depending on temperature contrast between the background and the gas components in the scene. Actually, we receive background radiance at sensor as disrupted by gases in the scene like given below (see Figure 8-

10). Scenario 1 demonstrates detection by gas absorption situation (see Figure 8), scenario 2 demonstrates non-detection situation (see Figure 9) and scenario 3 demonstrates detection by gas emission situation (see Figure 10).

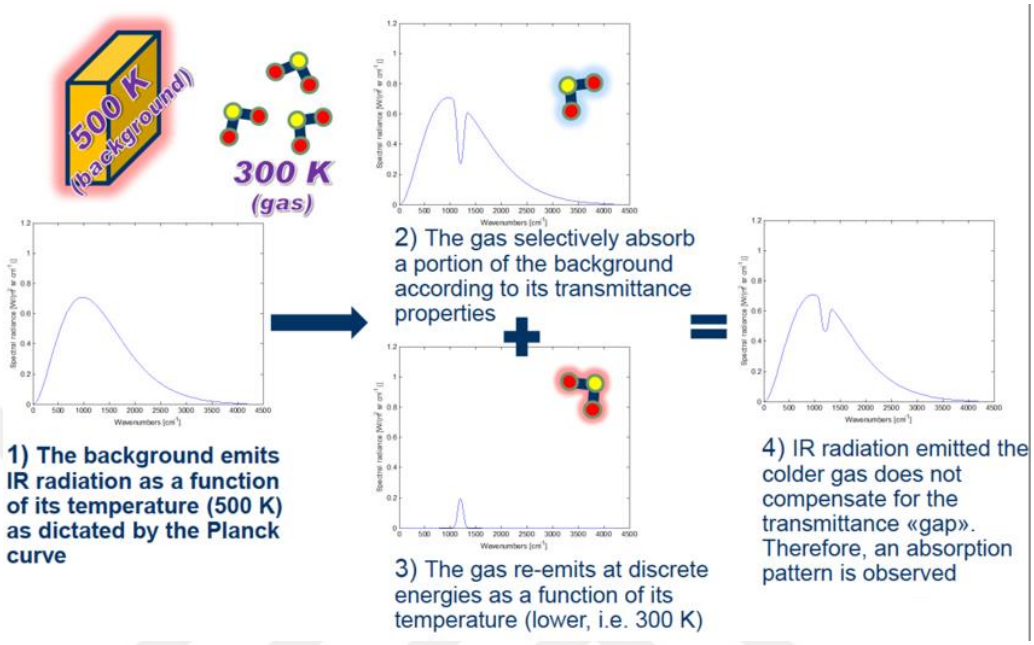

Figure 8 Detection by Absorption (taken from [Telops Hypercam Training 2014])

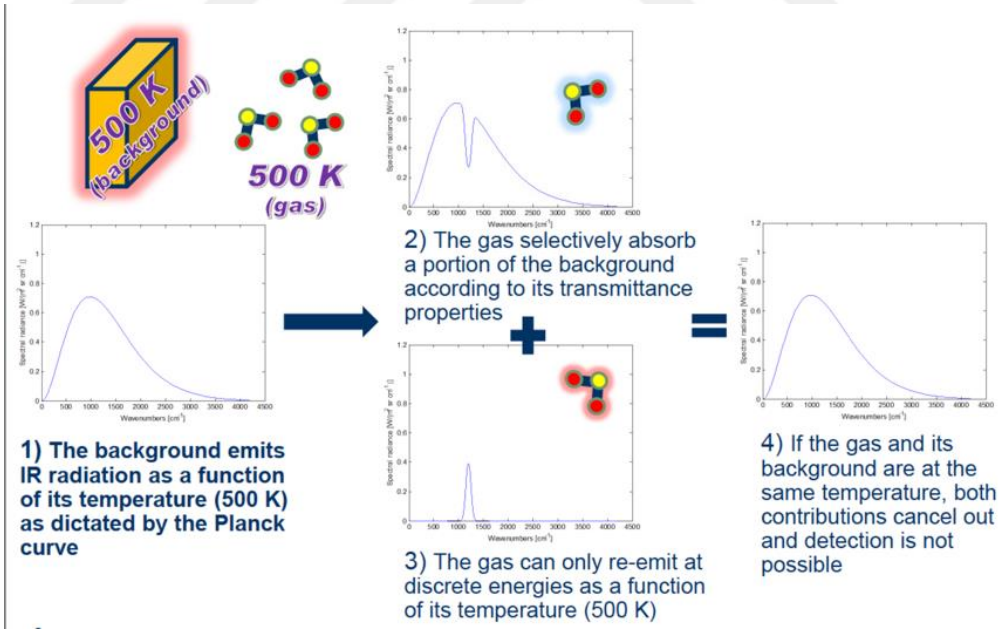

Figure 9 Non-detection (taken from [Telops Hypercam Training 2014])

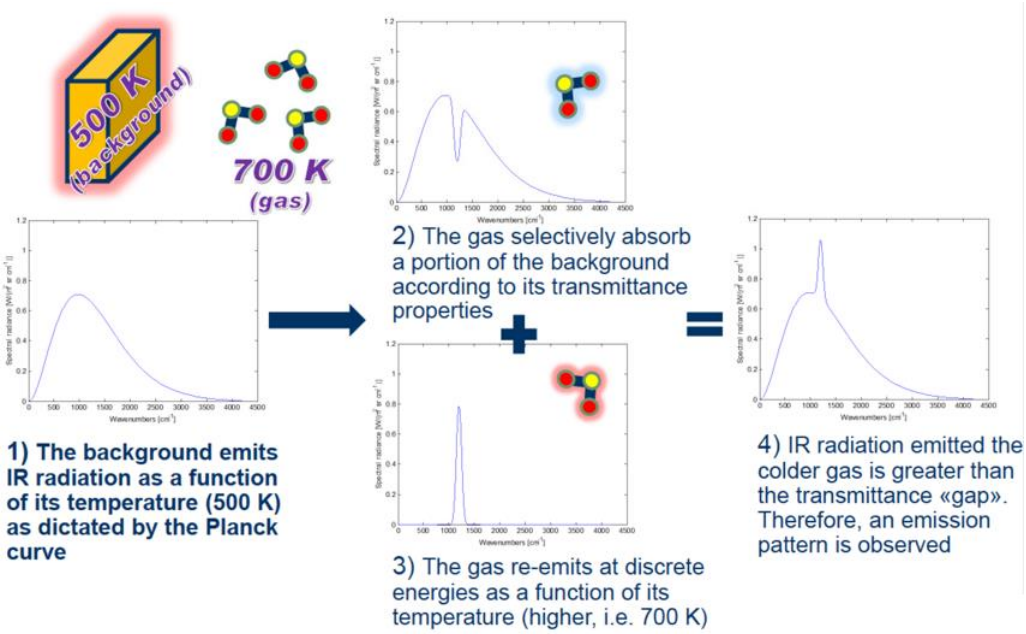

Figure 10 Detection by Emission (taken from [Telops Hypercam Training 2014])

2.3. Literature Survey

In this section, we provide an overview about the gas detection, identification and quantification methods. Several methods for remote sensing of gas plumes are presented in the literature. Both active and passive methods are implemented for this purpose. In all methods, there are some common parts such as the need of temperature, atmospheric conditions and background reflectance specifications for physical implementations; on the other hand, machine learning implementations need information about possible reference signatures and information of the spatial coordinates of gas pixels.

Pogorzala (see (Pogorzala, 2004)) presents an algorithm that identifies the pre-detected gas pixels in effluent plumes by using linear least-squares regression techniques in DIRSIG synthetic images for gases including NH_3 and Freon-114. DIRSIG images are generated under the following three assumptions; first of all, the plume is spatially constructed by using the gas concentration. This concentration follows an exponential decay it the downwind direction therewithal the width increases as the plume travels further and follows a Gaussian distribution in the across-track direction. Two steps methodology used; firstly for unmixing, matrix regression is implemented then for detection phase unconstrained stepwise linear regression and F-test are conducted.

Vallières (see (Vallières et al., 2005)) presents detection/identification and quantification algorithms which are used for hyperspectral imagers that operate in the thermal infrared region. Telops FIRST-LW Sensor Data with 4 cm^{-1} spectral resolution is used for gases include CH_3OH, SF_6, O_3, FREON, CG, NH_3, DMMP, CWA, TEP and H_2O. Three steps methodology used; firstly, data is converted to brightness temperature map and background sign is removed, then clutter match filter / spectral angle mapper is implemented on the data and lastly 2-d bi-dimensional convolution with a boxcar-shaped filtering is used by finishing with thresholding.

Farley (see (Farley et al., 2007)) presents remote sensing of chemical results obtained

by FIRST (Field-portable Imaging Radiometric Spectrometer Technology) sensor which is developed by Telops. Telops FIRST-LW Sensor Data with 4 cm^{-1} spectral resolution used for gases include SF_6, NH_3, SF_6-NH_3 mixed, TEP, DMMP and SO_2. Four steps methodology is used; firstly, radiance data is converted to brightness temperature and background removal algorithm implemented, then clutter matched filter/spectral angle mapper procedures are used for discriminating gas containing pixels, then boxcar-shaped filtering is used for 2-d bi-dimensional convolution and finally, thresholding is applied on resulting data.

Spisz and his friends (see (Spisz et al., 2007)) present a usable standoff detection/identification algorithm for varied chemical compounds by the use of various field measurements. Telops FIRST-LW Sensor Data with 4 cm^{-1} spectral resolution used for gases include AA, SF_6, NH_3, mix of SF_6 and NH_3, Phosgene, TEP and DMMP. Three steps methodology is used; firstly, pre-release data cube is taken before the release of gases and implemented principal components analysis to find background vectors, then match filter and spectral angle mapper scores of data is computed and finally, for gas detection/identification step-wise regression is conducted.

Rotman and his friends (see (Sagiv, Rotman, & Blumberg, 2008)) analyzed existing algorithms and composed a remote sensing application which involves detection/identification and quantification of different effluent gases on Telops FIRST-LW Sensor Data with SO_2 and CO_2 gases at distances of 400m and 1700m. Three steps methodology is used; firstly critical wavelengths are localized, then correlation coefficient metric is used to detect highly concentrated pixels, then matched filter is used with the new reference signature for detection of target gases and finally, a least square model is used for generating relative pixel content by curve fitting the detected gases signature to the data pixel.

Tremblay (see (Tremblay et al., 2010)) present gas detection/identification and quantification algorithms used for identifying the gas released by distant stacks and for quantifying their mass flow rates with an IFTS. They used Telops FIRST-LW Sensor Data with 4 cm^{-1} spectral resolution for gases released from a chimney. Three steps methodology is used; firstly, plume free pixels are selected on the center of chimney to estimate atmospheric parameters, then plume free pixels are selected to estimate background signature and lastly plume is localized in the image by physical model given in paper.

Hirsch and Agassi (see (Hirsch & Agassi, 2010)) present a unique algorithm which does not need clear background information to detect/identify the target gaseous plumes. Telops FIRST-LW Sensor Data with 4 cm^{-1} spectral resolution for gases include CHF_3 and SF_6 which are in about 60m distance is used. Five steps methodology used; firstly, divisive hierarchical spectral-spatial decomposition with K-means and spatial segmentation is implemented on data, then each segment's spectral analysis is conducted, then a physical model is used for calculating the transmission of each segment, then correlation between calculated transmission and target gas signature is calculated and finally, thresholding is applied on calculated correlation results.

Rotman (see (Feinmesser & Rotman, 2010)) uses Sagiv's (see(Sagiv et al., 2008)) algorithm and add new procedure to enhance performance. This procedure uses the

"stepwise regression" method combined with detection/identification methods. Telops FIRST-LW Sensor Data with 225 spectral bands for gases include CO_2, F_{12}, F_{114}, H_2O, N_2O, NH_3, O_3, SO_2 and NO_2 is used. Three steps methodology is used; firstly, in order to find gases step-wise regression is used, then black body radiation is processed on signatures and step-wise regression is implemented again, then shift fitting method is used to identify gases and finally compare results with signatures of target gases.

Kastek and his friends (see (Systems, Measurement, Mariusz Kastek, Tadeusz Piątkowski, 2011)) presents a usable method for detecting gases in turbulent stack plumes by using Telops FIRST-LW Sensor Data with 4 cm^{-1} spectral resolution for gases include NO_2, CO_2 and mix of Propane and Butane. Four steps methodology is used; firstly, apparent temperature of each pixel is calculated, then for each pixel Planck's blackbody curve is generated by using the highest result of temperature values, then each pixel value is divided by calculated blackbody curve, finally, general physical model is used for detection of gases.

Rotman and Kuflik (see (Kuflik & Rotman, 2012)) present a study that aims to find the needed minimal number of spectral bands for detecting a specific gas in a hyperspectral cube, in order to develop a hyperspectral gas sensor in the future. Synthetic data is created with CO_2 in the study by using three steps; firstly, they created five different cubes using various triangle shaped background vectors in different pixels, then created images are multiplied by a random uniformly distributed constant in the interval (0,1) in order to represent different effects and finally they added a random normally distributed constant for each pixel. After creating synthetic data constrained energy minimization and correlation from non-gas pixels are implemented for detection.

Sabbah and his friends (see (Sabbah et al., 2012)) presents a detection/identification algorithm that combines spectral and spatial information without the need of background signature. HI 90 data with methane and SF_6 gas is used. Five steps methodology is used; at the beginning, data is converted to brightness temperature map, then a Gaussian filter with size 3X3 pixels and full width half maximum 5 pixels is applied, then the temporal averages of each pixel on brightness temperature map is calculated by using multiple images regarding the same scene, then correlation coefficient of the gas signatures with the signatures on the image are calculated and finally, threshold is implemented on results.

Messinger (see (Messinger, n.d.)) presents a study that extends O'Donnell's (see (O'Donnell, 2004)) work by using real hyperspectral images of complex industrial facilities. Airborne Hyperspectral Imager (AHI) data for gases including methane, propane, butane, ethane, sulfur dioxide, ethylene, propylene and benzene is used. Four steps methodology employed; firstly, MODTRAN software is used for estimating the surface temperature through the identification of "background" region, then target gas signatures are calculated for every combination of temperature contrast and concentration path length, then geometric projection scheme is used for reducing number of signatures and finally, in attempt to detection maximum distance method (MaxD) is used.

CHAPTER 3

METHODOLOGY

In this section, proposed algorithm to be used in this thesis will be mentioned with its steps.

3.1. Proposed Method

The frequently used gas model given in (Tremblay et al., 2010) is utilized for detection of gases in the literature. However, some parameters required in the model cannot be obtained easily in remote sensing applications causing the model to be impractical and some solutions require user interaction. Therefore, we propose to estimate some of these parameters in order to improve the reference model.

Proposed method begins with brightness-temperature map generation and Planck curve computation. Then, current radiance data value is converted to emissivity value by black-body radiation curve compensation algorithm as preprocessing step discussed in Section 3.2.1. The method continues with hierarchically clustering and segmentation discussed in Section 3.2.2. MinCEntropy clustering algorithm is used for dividing the data into two clusters by distinguishing pixels according to their spectral similarity with using classification algorithms. This step is followed by a connected components analysis for segmentation. The iterative clustering and segmentation process continues until all segments' sizes are smaller than a threshold determined before test. As discussed in Section 3.2.3 all segments are considered as potential gas and background pairs. The gas and background segment pairs highly correlated with the reference signature are selected as the detected gas emission region. The flowchart of the proposed system is demonstrated in Figure 11.

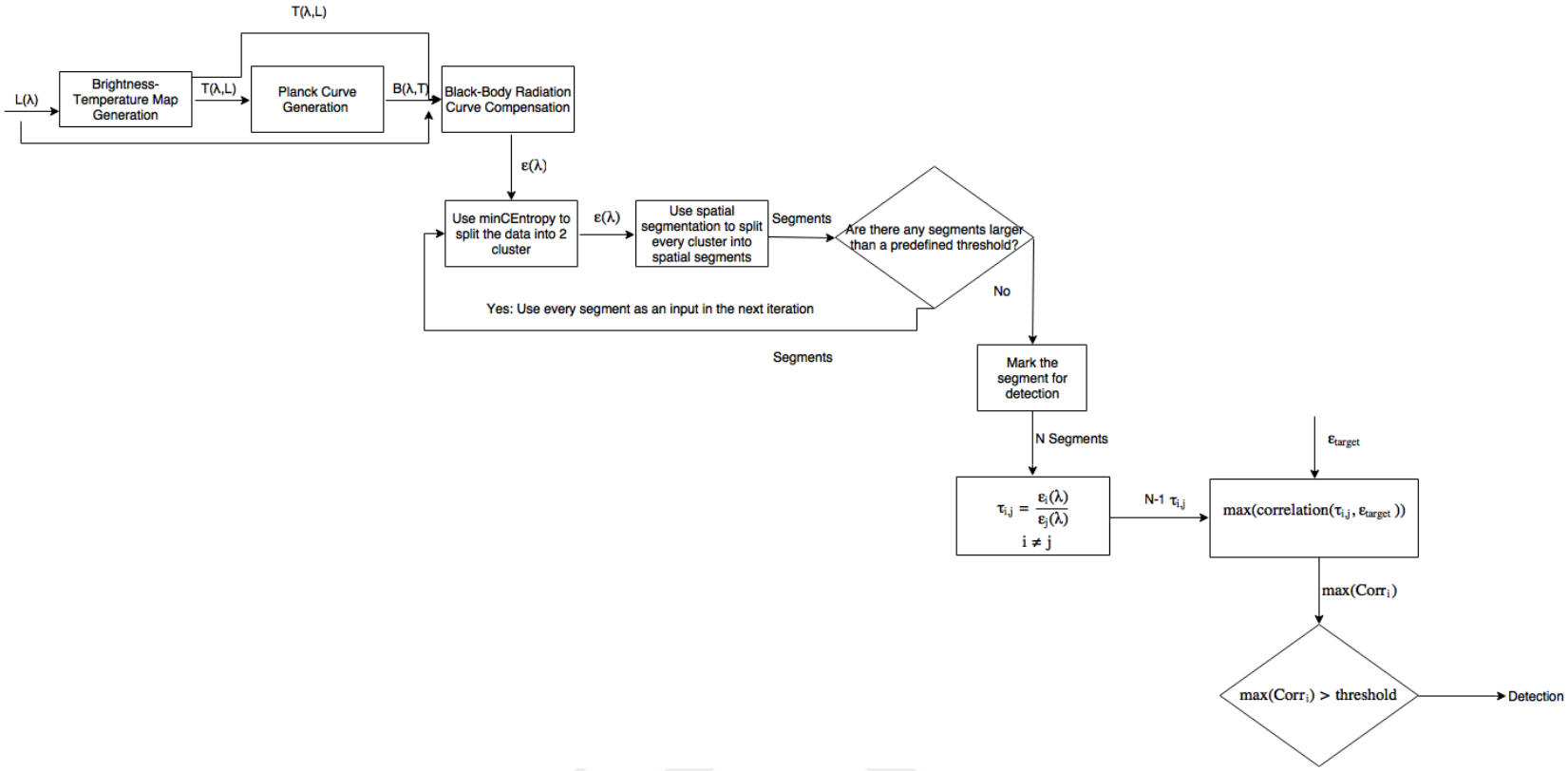

Figure 11 Proposed Method Flowchart

3.1.1. Pre-Processing

3.1.1.1.Brightness Temperature

In the literature, most of the studies use radiance information of hyperspectral data for gas detection and quantification applications. However Harig and Matz (see (Harig & Matz, 2001)) suggest that using brightness temperature map of the data instead of radiance data is more suitable for remote sensing of gas purposes. In the meantime, radiance spectrum of the hyperspectral data does not have fixed margins as a baseline. This makes signature based detection algorithms more difficult. On the other hand, the emission spectra of many surfaces are high and nearly constant in the range of 650 cm^{-1} − 1500 cm^{-1} so they are almost similar with the spectrum of brightness temperature and the spectrum of the blackbody of these objects are nearly fixed. Also, the background spectrum becomes the baseline of the brightness temperature spectrum of the relevant hyperspectral data. Based on these descriptions, brightness temperature of the data is generated by the following equation:

$$\mathrm{T}(\lambda, L) = \frac{c_2 \lambda}{\ln(\frac{c_1 \lambda^3}{L} + 1)} \tag{3.1}$$

where c_1 and c_2: constants, λ: wavenumber, L: radiance data.

*3.1.1.2.*Planck Curve

The theory of heat radiation (see (Planck, 1914)) reveals that the radiance data is affected by the temperature on thermal radiation in LWIR bands that is entitled as Planck's curve and it figures the theoretical blackbody curve obtained from Planck's formula given below:

$$\mathrm{B}(\lambda, T) = \frac{c_1 \lambda^3}{\exp\left(\frac{c_2 \lambda}{T}\right) - 1} \tag{3.2}$$

where c_1 and c_2: constants, λ: wavenumber.

*3.1.1.3.*Black-Body Radiation Curve Compensation

In order to detect the target gases, we need to compensate the atmospheric effects in the In order to detect the target gases, we need to compensate the Black-Body Radiation Curve in regarding to compensate atmospheric effects in the data due to existence of various gases characteristics in LWIR and MWIR region. For this purpose, Black-Body Radiation Curve Compensation algorithm (see (Omruuzun & Yardimci Cetin, 2015)) will be used. According to mentioned algorithm, a theoretical black body curve is constructed by the ambient temperature value provided from hyperspectral imagery header file and this curve is used for eliminating radiance values changes by means of temperature effects with formula given below:

$$C_\lambda = \frac{\mathrm{BB}_{max}}{\mathrm{B}(\lambda, T)} S_\lambda \tag{3.3}$$

where ; λ: wavenumber and C_λ : Corrected radiance value at λ, BBmax : Maximum radiance value on the Black-Body curve, $B(\lambda, T)$: Black-Body radiance value at λ, and S_λ : Radiance value measured by the hyperspectral sensor at λ.

3.1.2. Clustering and Segmentation

3.1.2.1.Clustering By Using minCEntropy

As mentioned in Chapter 2.2, the gaseous pixels radiance in the data cube includes background emissivity and it is also affected by the temperature of the background. Therefore, separating background from the emission region becomes crucial in gas detection problems. We predicate our clustering approach according to a study on detection of gaseous plumes and background by using hierarchical clustering (see (Hirsch & Agassi, 2010)). The algorithm divides the data into two clusters in each iteration, and forwards the clusters to the segmentation step explained in Chapter 3.1.2.2. The segments larger than a predefined threshold are sent back to the clustering step. This iteration provides using of a fixed number of clusters in the clustering method. Hirsch et al. implements k-means (see (Zhang & Rudnicky, 2002)) algorithm for clustering, assumes the data is linearly separable, that selects the central points and assign the data according to their distances to the centers by using minimization of the sum of squares of the Euclidean distance between the samples and the cluster centers. However, this approach is not applicable for real-life problems because of the high dimensionality of the hyperspectral imagery. Additionally, if k-means algorithm is executed repeatedly, different results will be obtained. In this thesis for clustering part minCEntropy (see (Vinh & Epps, 2010)) clustering algorithm, an objective-function-oriented approach, is being used. MinCEntropy assigns the data according to their similarity to the cluster members by maximizing of the sum of average similarities judged by Gaussian kernel between the cluster members and the sample. Main distinctness of minCEntropy is that it makes no assumption on data distribution used despite being built upon information measures and suggests heuristic to set the kernel and quality-diversity trade-off parameter. Results of minCEntropy on the same data are very decisive and do not change.

3.1.2.2.Segmentation

After clustering the data in each iteration, each cluster is spatially segmented according to their connectivity (see (Jähne, 1991)) with the assumption that the real-life gas emission region, the connected pixels of the gas including pixels, must be in the same segment. All the segments smaller than the predefined threshold is labeled and remaining segments are sent back to clustering step. Successive clustering and segmentation continues iteratively until all the segments found are smaller than the threshold value. Concurrently, background of the emission is labeled as a segment.

3.1.3. Detection and Identification

After clustering and segmentation step, detection and identification of target gases start. Several hypotheses are created by searching all segments as background and gas

emission region pairs. For each segment, by assuming that segment contains gas and all the other segments contain background, the transmittance value is calculated with equation 3.4. Therefore, for each segment segmentCount-1 number of different transmittance value is calculated with equation 3.4 which is derived from equation 2.12. As the emissivity values of pixels are used in the algorithm, the temperature related variables are dropped from the formula and equation 3.4 is derived. Subsequently the correlations between the calculated transmittance values and reference gas signature is measured (see (Gatti & Donati, 1971)) in order to determine the most correlated pair with the equation given in 3.5

$$\tau_{target} = \frac{\varepsilon_i(\lambda)}{\varepsilon_j(\lambda)} \tag{3.4}$$

where τ_{target}: transmittance value of target segment, $\varepsilon_i(\lambda), \varepsilon_j(\lambda)$: emissivity values of target segment and other segments.

$$corr = \frac{\sum_x \sum_y (A_{xy} - \overline{A})(B_{xy} - \overline{B})}{\sqrt{(\sum_x \sum_y (A_{xy} - \overline{A})^2)(\sum_x \sum_y (B_{xy} - \overline{B})^2}} \tag{3.5}$$

where A: target segment transmittance value, B: reference gas signature transmittance value, $\overline{A}$ and $\overline{B}$ are mean values of regarding vectors.

Maximum correlation value of the pixels is labeled as the detection rate of target gas. The final detection is implemented with Otsu thresholding (see (Otsu, 1979)) method which determines appropriate threshold point TP that maximizes the given expression by

$$Ratio\ (TP) = \frac{(\overline{\mu}.\omega(TP) - \mu(TP))^2}{\omega(TP).\mu(TP)} \tag{3.6}$$

where $\omega(TP) = \sum_{i=0}^{TP} P_i,\ \mu(TP) = \sum_{i=TP+1}^{N} P_i,\ \overline{\mu} = \sum_{i=0}^{N} P_i$ while N is the maximum possible quantization levels. N = 255 for 8-bit image components and P_i is the probability of pixels in the hyperspectral image.

CHAPTER 4

EXPERIMENTS

In this section, spectral libraries used in this thesis and data cubes used as Data Sets will be introduced first. Then proposed algorithm results will be presented by comparing frequently used gas detection results.

4.1. Sources of Data

4.1.1. Spectral Library

In this thesis, the Pacific Northwest National Labs (PNNL) infrared reference database and the U.S. National Institute of Standards and Technology (NIST) infrared reference database are used as spectral libraries through they are designed for hyperspectral imagery, commonly used in hyperspectral community and publicly available at http://nwir.pnl.gov and http://webbook.nist.gov/chemistry.
In this thesis five gases are chosen based on three criteria:

1. The gas must have samples as detected by the TELOPS Hypercam.
2. The gas must be present in the FTIR datasets provided by UDI.
3. The gas must be present in PNNL/NIST Infrared Spectral Library.

These gases are Sulfur Hexafluoride (F_6S), Ethylene (C_2H_4), Butane (C_4H_{10}), Methanol (CH_3OH) and Carbon Dioxide (CO_2). PNNL and NIST spectra of target gases are given in Figures 12-16. Unfortunately, detection of Nitrous Oxide cannot be conducted as we do not have real hyperspectral imagery including Nitrous Oxide.

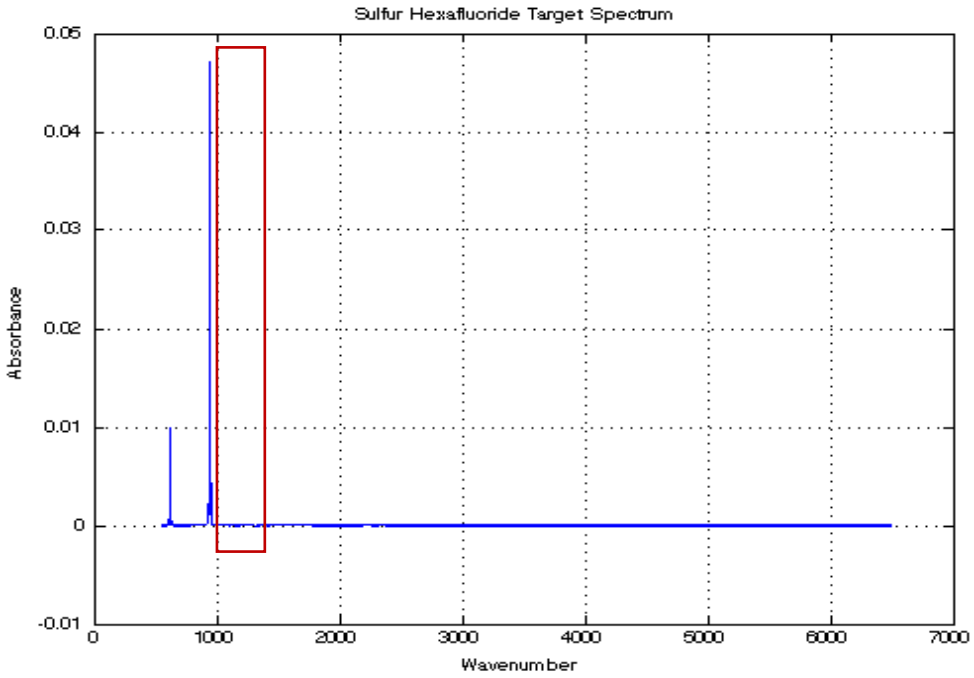

Figure 12 Sulphur Hexafluoride PNNL Absorption Spectra

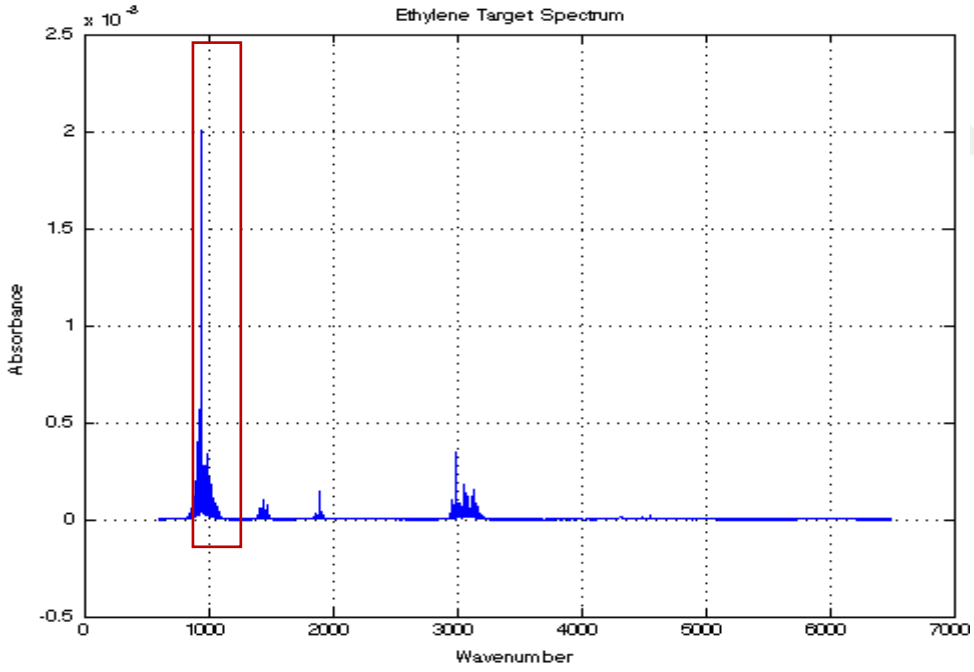

Figure 13 Ethylene PNNL Absorption Spectra

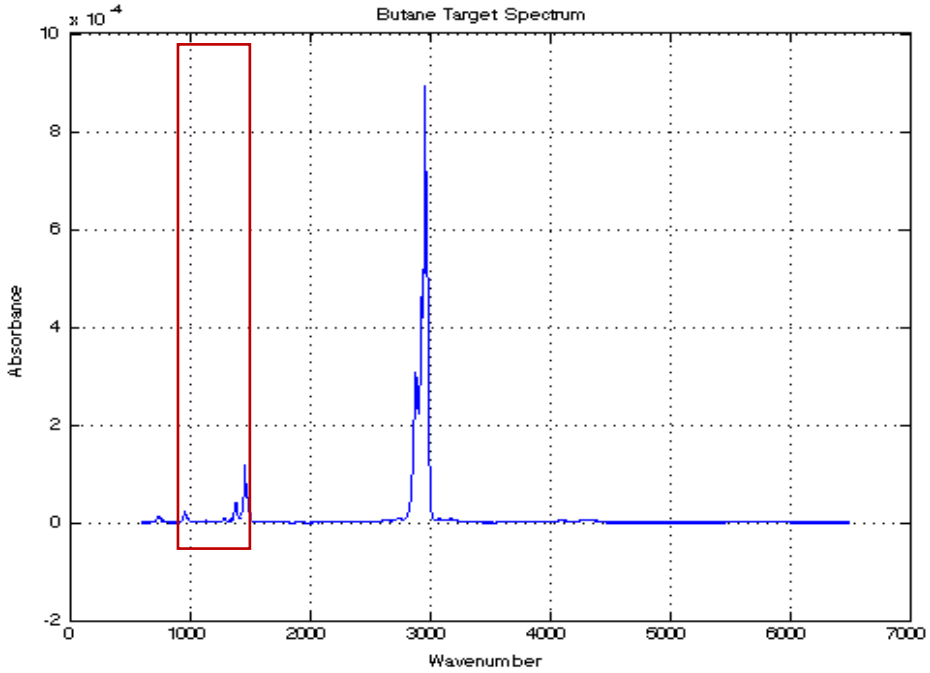

Figure 14 Butane PNNL Absorption Spectra

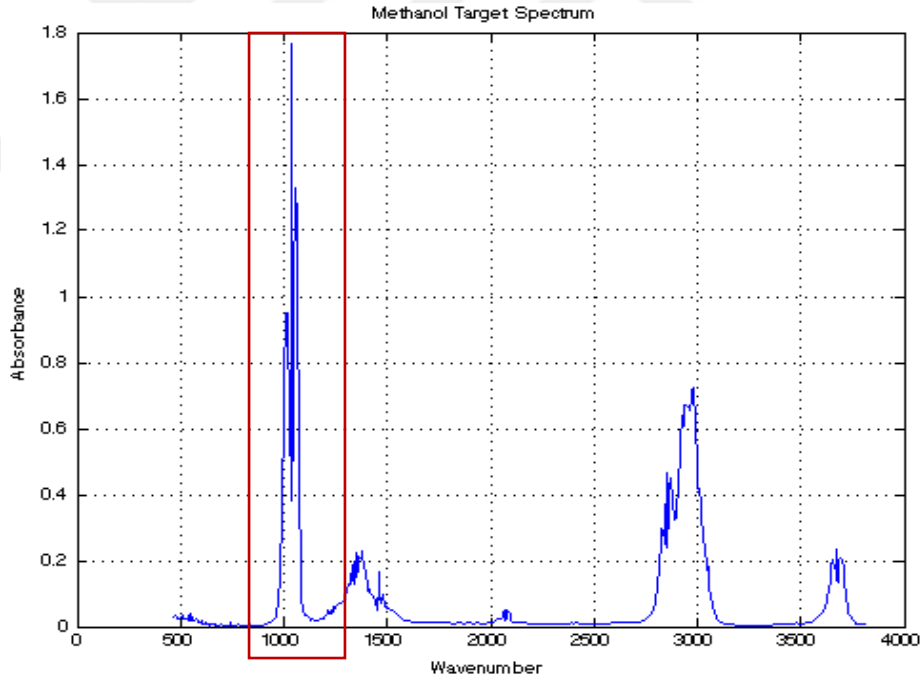

Figure 15 Methanol NIST Absorption Spectra

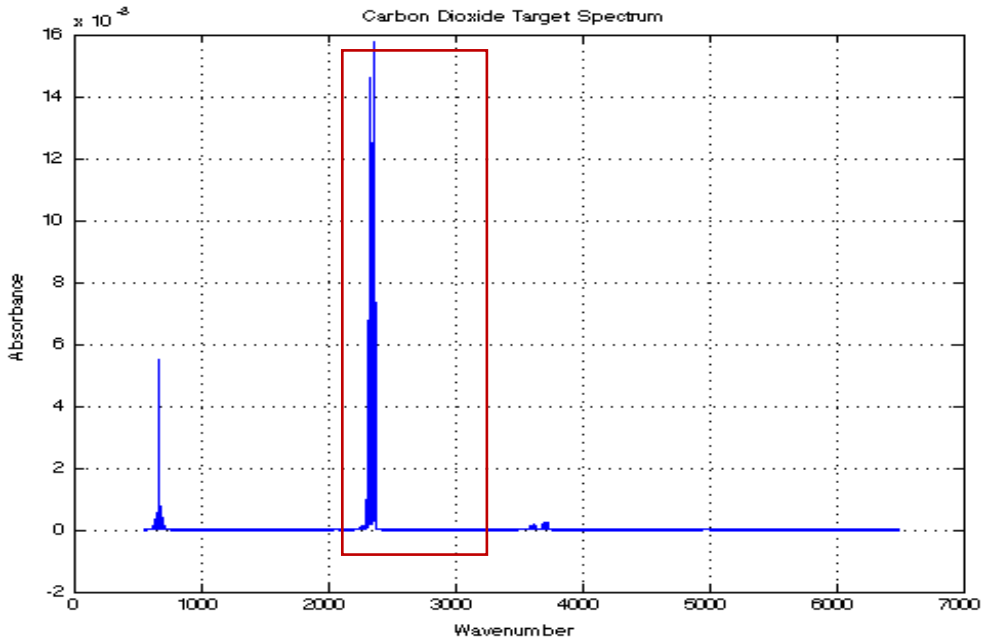

Figure 16 Carbon Dioxide PNNL Absorption Spectra

4.1.2. Data Sets

In this study, existing data sets are provided by UDI which are taken with Telops FTIR Camera mentioned in Section 2.1.2. There are 6 different data cubes containing Methanol, Sulphur Hexafluoride-Ethylene, two scenes with CO_2, one Butane and one data cube which has same scene as butane containing data cube but no gases exhaled. Data cube information are obtained from the header files provided by FTIR Camera.

4.1.2.1. *Data Cube 1*

Spectral Range : 877 cm^{-1}-1285 cm^{-1}
Band Number : 124 Bands
Ambient Temperature : 300 °K
Width * Height : 200 * 200 pixel
Spectral Resolution : 4 cm^{-1}
Distance : ~2-3m
Gas Types : Methanol

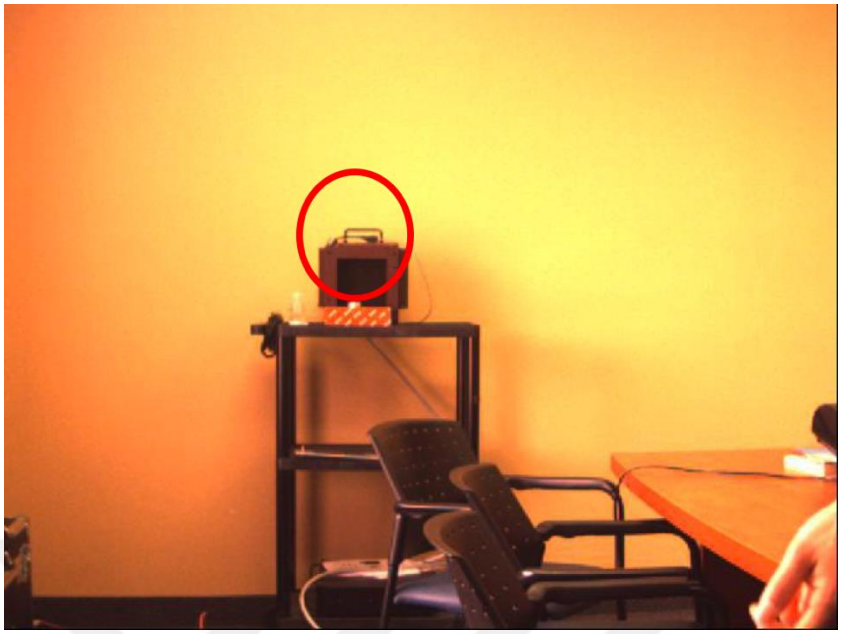

Figure 17 Data Cube 1

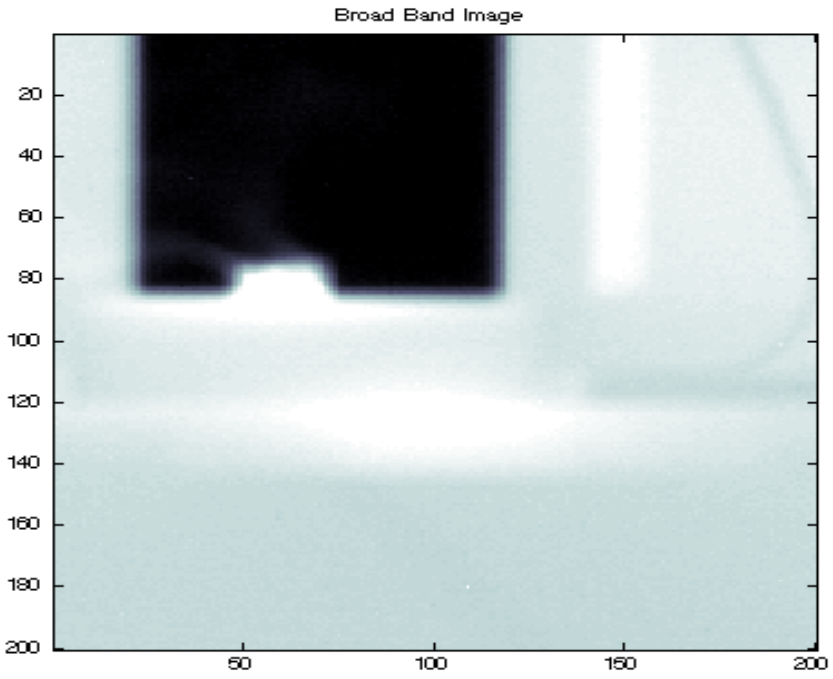

Figure 18 Data Cube 1 Broadband Image

4.1.2.2.*Data Cube 2*

Spectral Range	: 851 cm^{-1}-1288 cm^{-1}
Band Number	: 171 Bands
Ambient Temperature	: 302 °K
Width * Height	: 200 * 200 pixel
Spectral Resolution	: 4 cm^{-1}
Distance	: ~2-3m
Gas Types	: Sulfur - Ethylene

Figure 19 Data Cube 2

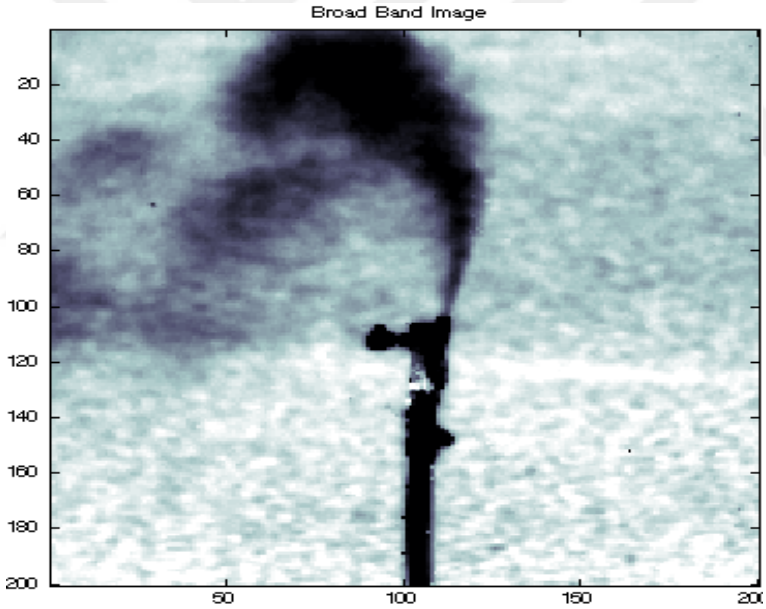

Figure 20 Data Cube 2 Broadband Image

4.1.2.3.*Data Cube 3*

Spectral Range : 876 cm^{-1}-1285 cm^{-1}
Band Number : 124 Bands
Ambient Temperature : 310 °K
Width * Height : 128 * 128 pixel
Spectral Resolution : 4 cm^{-1}
Distance : ~2-3m
Gas Types : Butane

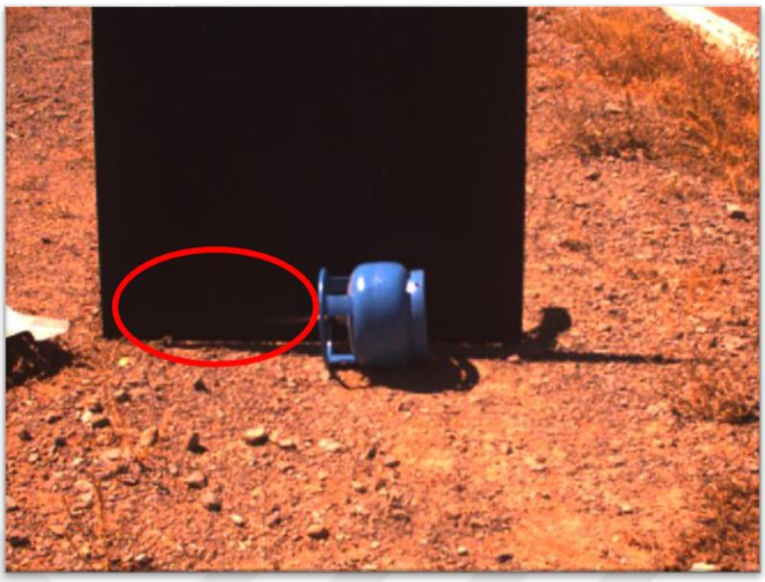

Figure 21 Data Cube 3

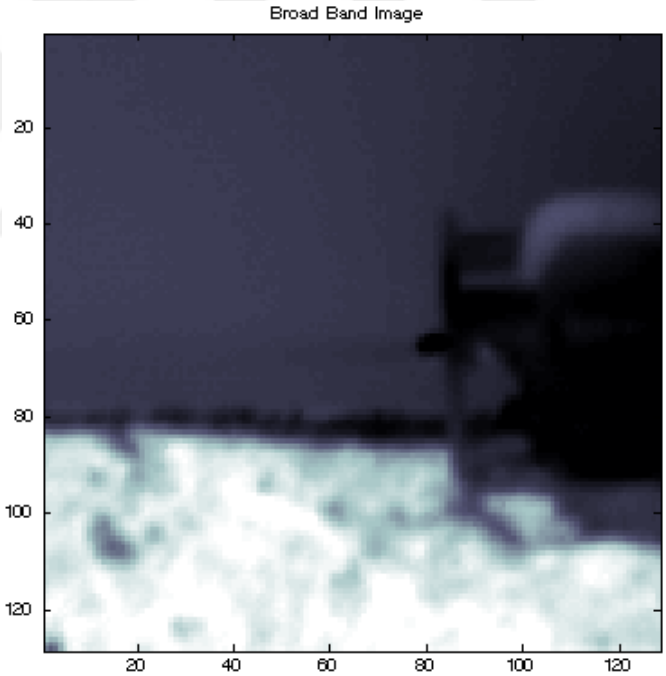

Figure 22 Data Cube 3 Broadband Image

4.1.2.4.*Data Cube 4*

Spectral Range	: 876 cm^{-1}-1285 cm^{-1}
Band Number	: 124 Bands
Ambient Temperature	: 310 °K
Width * Height	: 128 pixel * 128 pixel
Spectral Resolution	: 4 cm^{-1}
Distance	: ~2-3m
Gas Types	: No gas

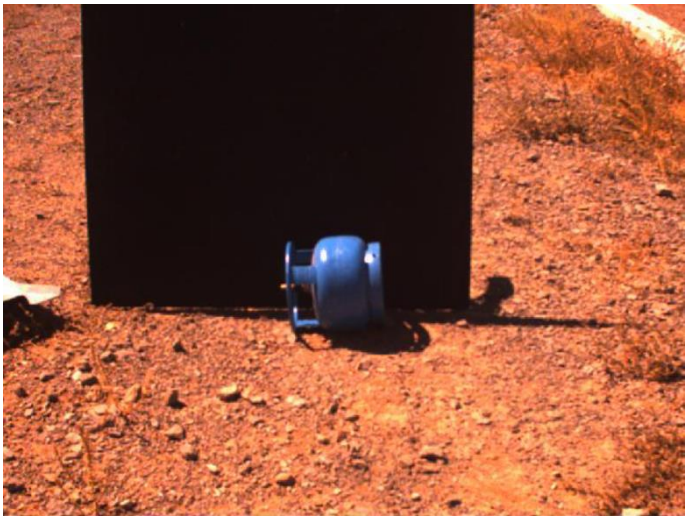

Figure 23 Data Cube 4

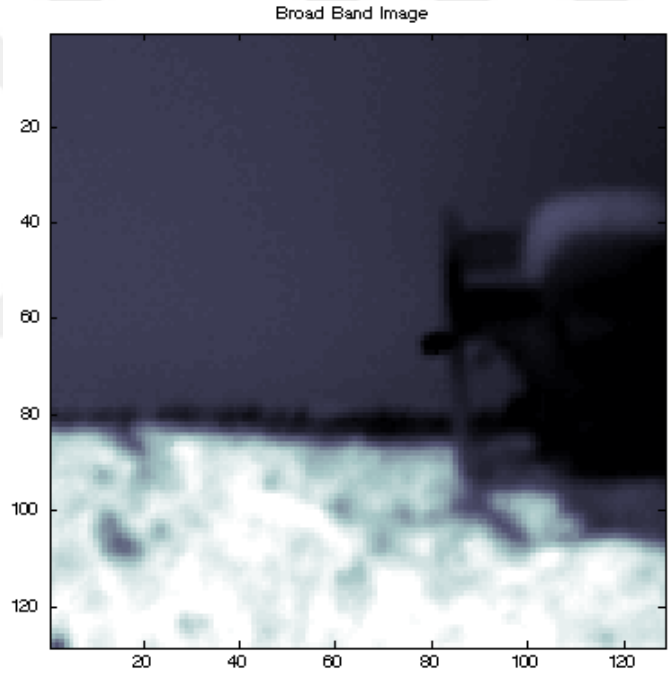

Figure 24 Data Cube 4 Broadband Image

4.1.2.5.*Data Cube 5*

Spectral Range	: 1799 cm^{-1}-3345 cm^{-1}
Band Number	: 797 Bands
Ambient Temperature	: 291 °K
Width * Height	: 320 pixel * 256 pixel
Spectral Resolution	: 2,3 cm^{-1}
Distance	: 5m
Gas Types	: Carbon Dioxide

Figure 25 Data Cube 5

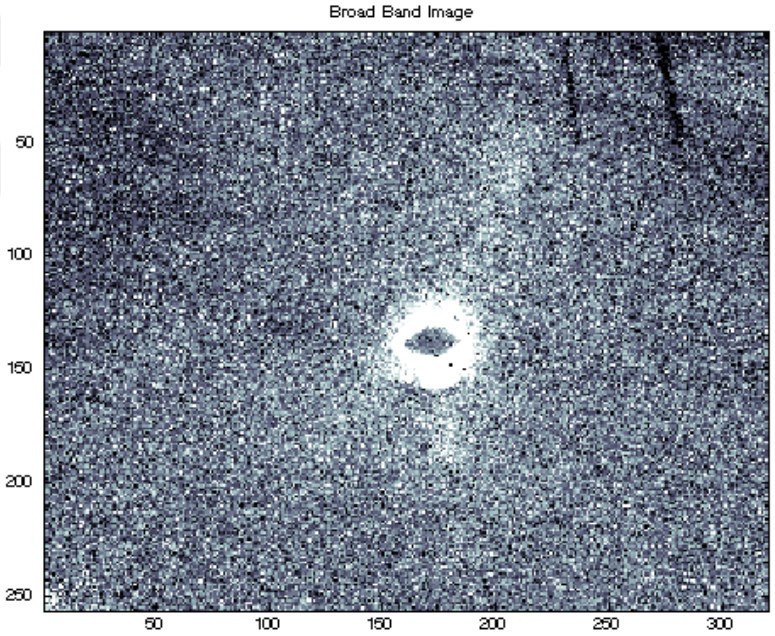

Figure 26 Data Cube 5 Broadband Image

4.1.2.6.*Data Cube 6*

Spectral Range	: 2022 cm^{-1}-2869 cm^{-1}
Band Number	: 255 Bands
Ambient Temperature	: 394 °K
Width * Height	: 320 pixel * 256 pixel
Spectral Resolution	: 4 cm^{-1}
Distance	: ~5m
Gas Types	: Carbon Dioxide

Figure 27 Data Cube 6

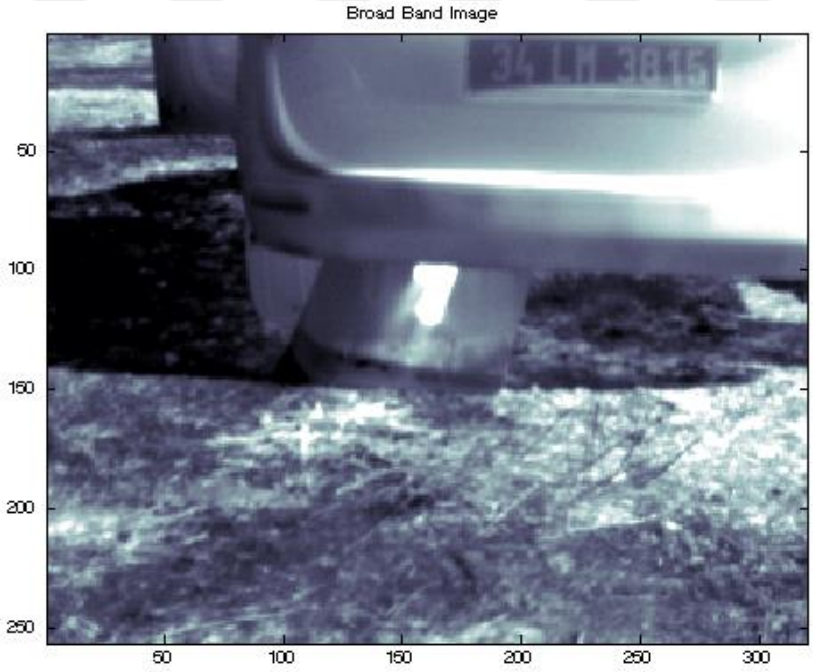

Figure 28 Data Cube 6 Broadband Image

4.2. Experimental Results

In this section proposed method and state of the art method in literature will be compared visually. Firstly, all the data cubes are processed with the proposed method by setting cluster size 50,250,500 and 1000 pixels. Then all the data cubes are processed with the algorithm used frequently in the literature which takes background region of data cube as an input to implement equation 2.12 on the data cube pixels. Henceforth, proposed method herein referred to as Algorithm 1; state of the art method taken from literature herein referred to as Algorithm 2.

The flowchart of the Algorithm 2 is demonstrated in Figure XX. Algorithm 2 firstly

converts radiance data to brightness temperature map as pre-processing step, then data and referred gas signature are cropped according to the spectral channels that referred gas shows distinct characteristics. Afterwards background region is selected by the user manually to determine background signatures. After all the steps transmittance values calculated by using equation 2.12. Finally, correlation coefficient is calculated by using equation 3.5 for each pixel.

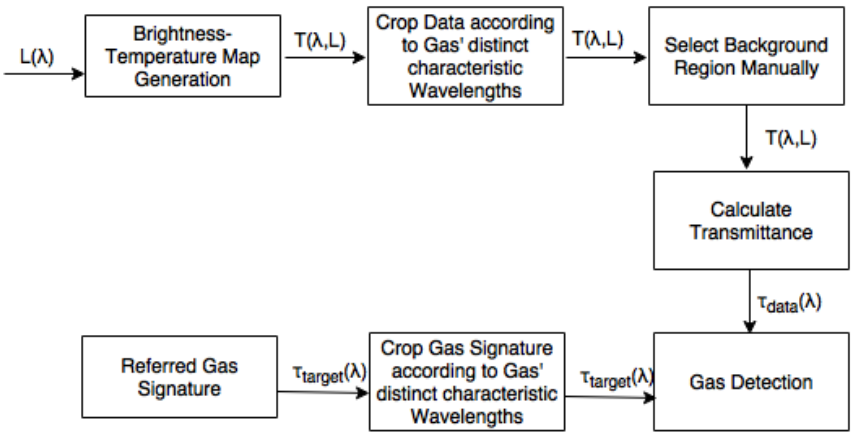

Figure 29 Algorithm 2 Flowchart

For each data set, clustering results and detection results of Algorithm 1 both colored, Otsu implemented and Histogram of each result, detection results of Algorithm 2 both colored and Otsu implemented, cropped target gas spectrum, gas and background including pixels spectrum and transmittance and absorbance values calculated with equation 2.12 from gas including pixels are presented. In gas detection problems, it is difficult to determine and get exact ground truth as gas materials propagate in the scene according to different variables and cannot be observed in IR images or RGB images directly. Therefore, detection results will be interpreted and compared visually. In colored images, hot colors represent high detection results therewithal in Otsu implemented images, light colors represent high detection results.
During the experiments atmospheric transmittance characteristics, a sample given in Figure 30, is not considered as a variable but especially in carbon dioxide detection problem it is seen that this variable directly affects the results.

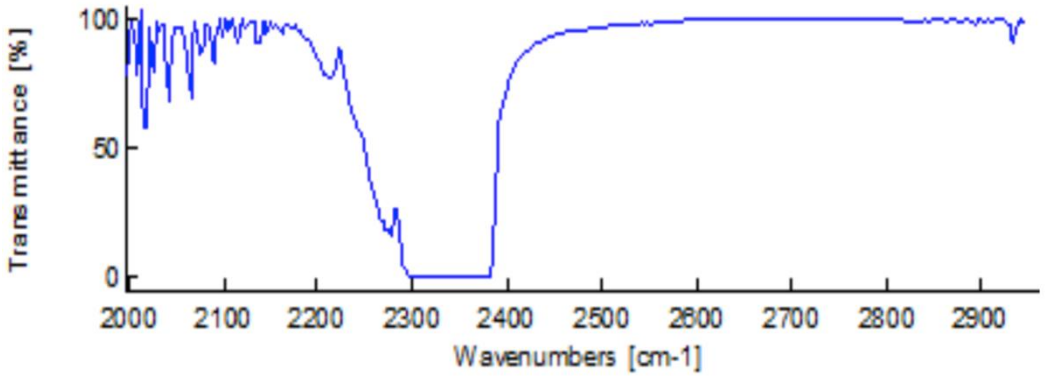

Figure 30 Sample Atmospheric Transmittance Spectrum ([taken from Gagnon et al.])

4.2.1. Data set 1

In experiment 4.2.1, methanol is oscillated as controlled.

Number of segments according to the threshold values are given below:

Threshold size 50 => 10118 Threshold size 250 => 7095

Threshold size 500 => 6051 Threshold size 1000 => 5080

As seen in detection results, results of algorithm 1 does not significantly differentiate between 250 segments result and 500 segments result. It can be observed that algorithm 1 is successful in detection of methanol gas in the scene. When compared with algorithm 1, algorithm 2 has similar detection results in detection of methanol gas in the scene.

4.2.1.1.Algorithm 1

Table 1 Data cube 1 minCEntropy Results Comparison

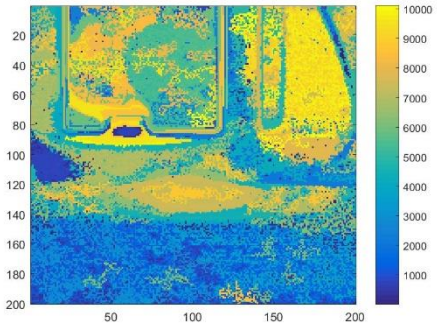

Figure 31 Data cube 1 minCEntropy Results with Threshold 50

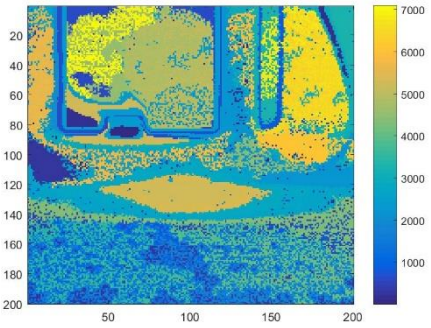

Figure 32 Data cube 1 minCEntropy Results with Threshold 250

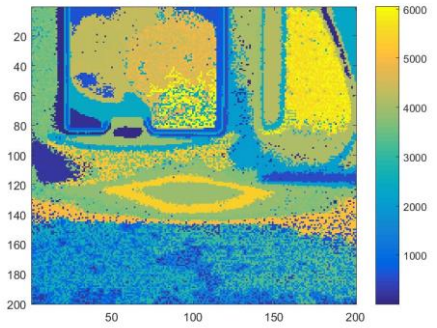

Figure 33 Data cube 1 minCEntropy Results with Threshold 500

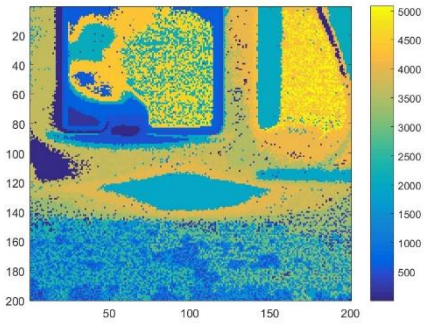

Figure 34 Data cube 1 minCEntropy Results with Threshold 1000

Table 2 Data cube 1 Detection Results Comparison

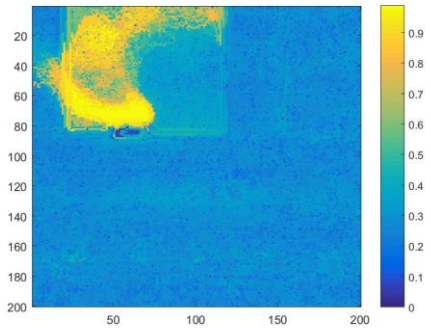

Figure 35 Data cube 1 Detection Results with Threshold 50

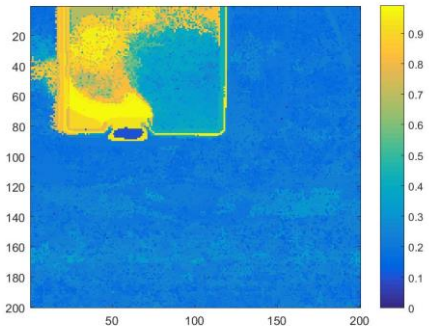

Figure 36 Data cube 1 Detection Results with Threshold 250

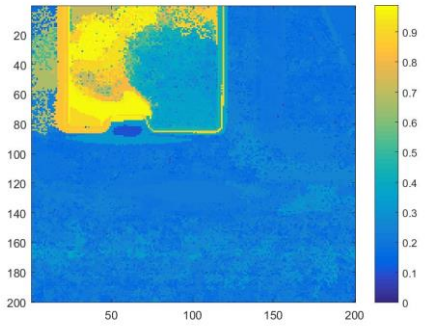

Figure 37 Data cube 1 Detection Results with Threshold 500

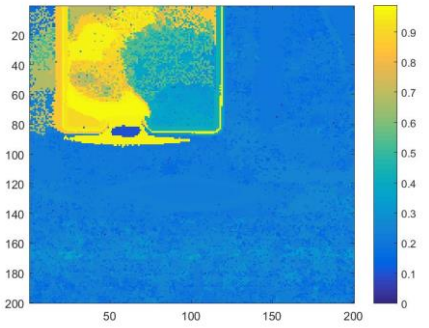

Figure 38 Data cube 1 Detection Results with Threshold 1000

Table 3 Data cube 1 Detection Results Comparison (Otsu)

Figure 39 Data cube 1 Detection Results with Threshold 50 (Otsu)

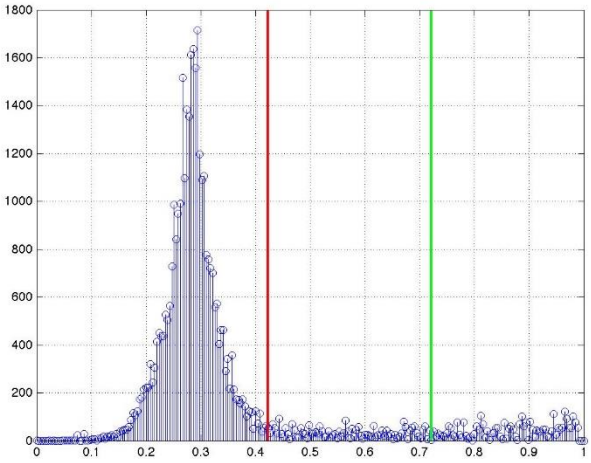

Figure 40 Data cube 1 Detection Results with Threshold 50 (Histogram)

Figure 41 Data cube 1 Detection Results with Threshold 250 (Otsu)

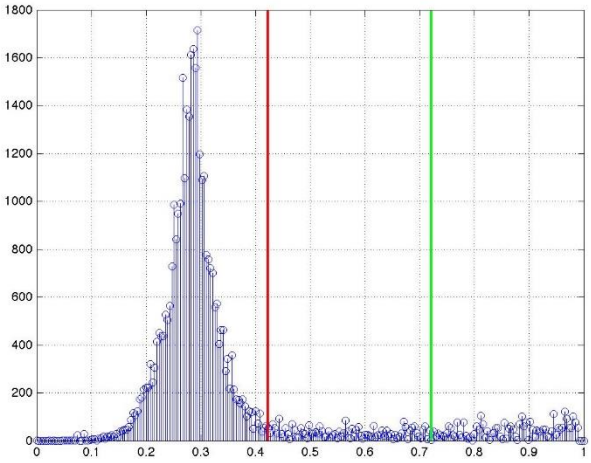

Figure 42Data cube 1 Detection Results with Threshold 250 (Histogram)

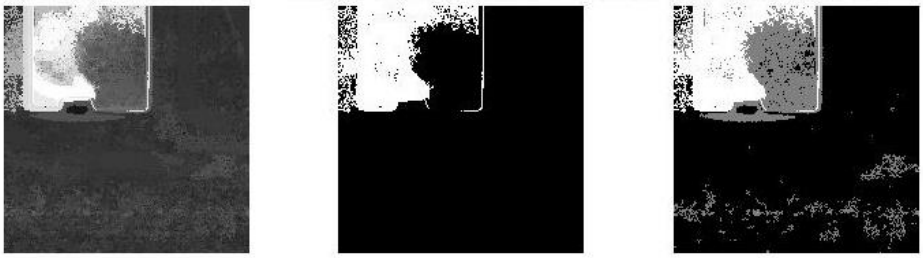

Figure 43 Data cube 1 Detection Results with Threshold 500 (Otsu)

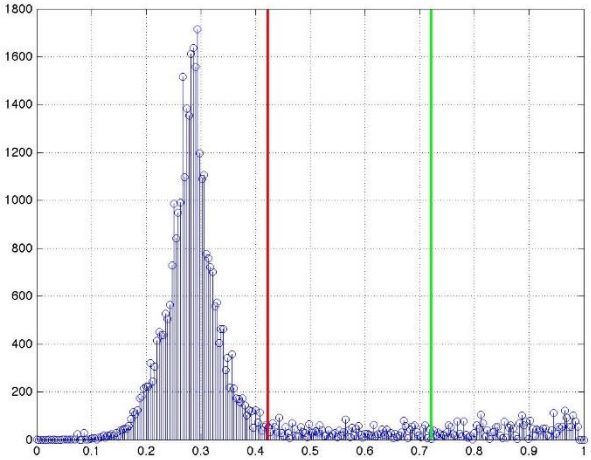

Figure 44 Data cube 1 Detection Results with Threshold 500 (Histogram)

Figure 45 Data cube 1 Detection Results with Threshold 1000 (Otsu)

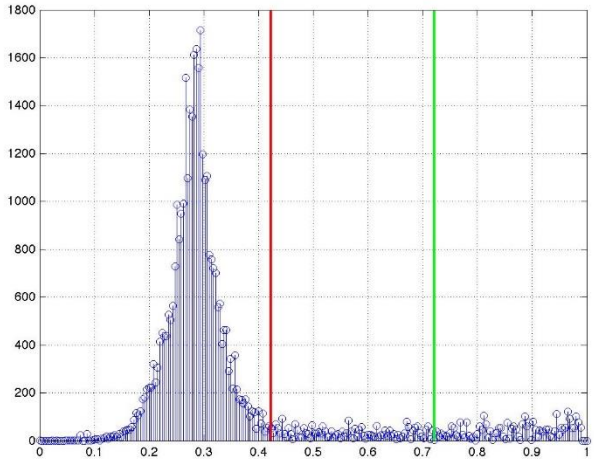

Figure 46 Data cube 1 Detection Results with Threshold 1000 (Histogram)

4.2.1.2.Algorithm 2

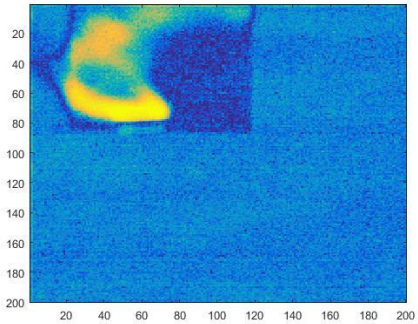

Figure 47 Data cube 1 Detection Results with Algorithm 2

Figure 48 Data cube 1 Detection Results with Algorithm 2 (Otsu)

4.2.1.3.Cropped Target Gas Spectrum

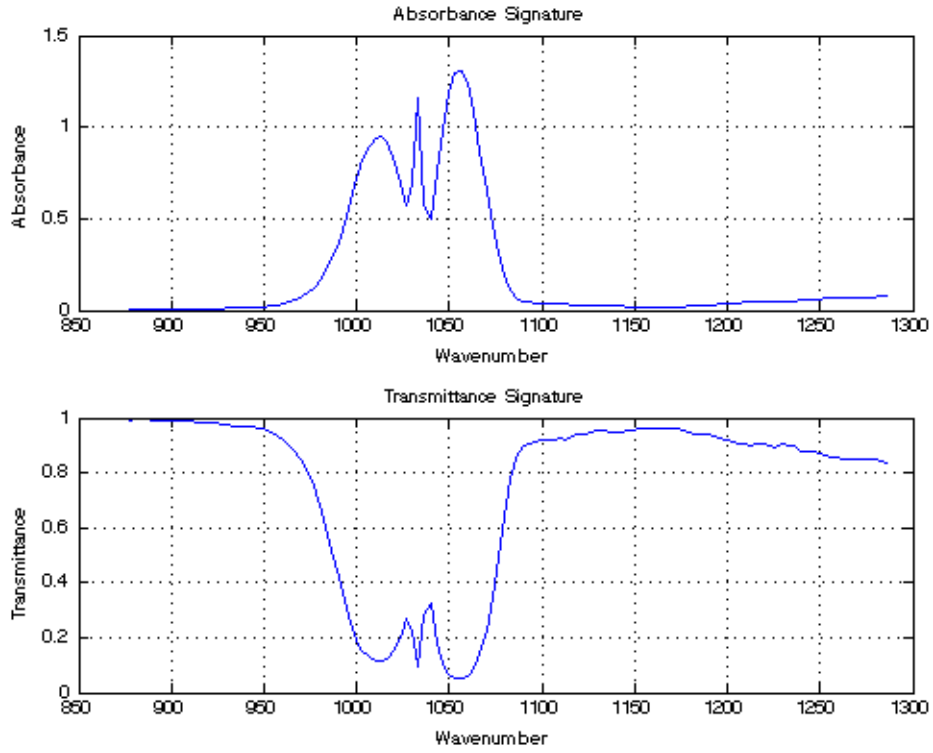

Figure 49 Cropped Target Gas Spectrum

4.2.1.4.Background-Gas Including Pixel Spectrums

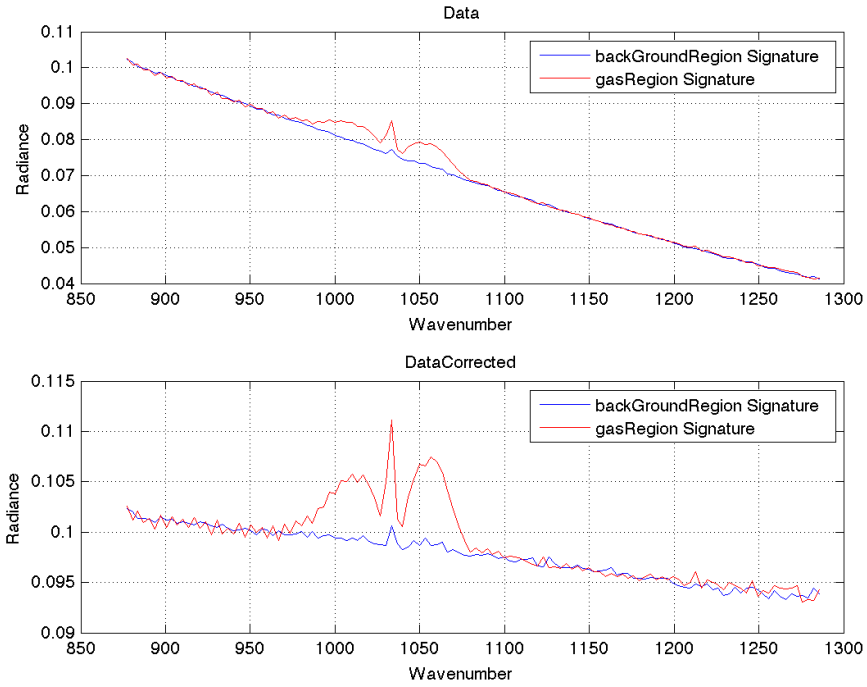

Figure 50 Background&Gas Including Pixel Spectrums

4.2.1.5.Calculated Transmittance and Absorbance Values of Gas Including Pixels

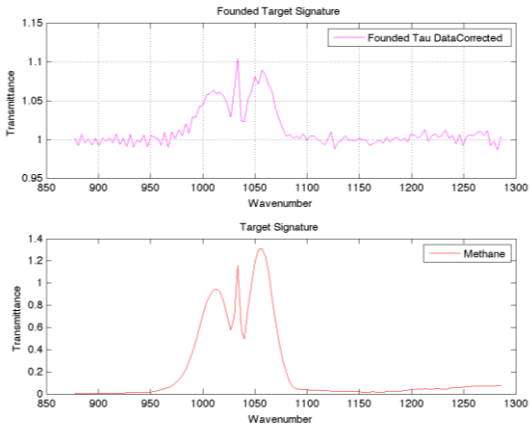

Figure 51 Data cube 1 Calculated Gas Transmittance

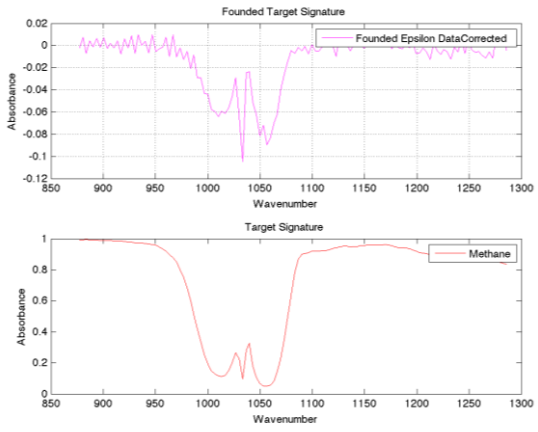

Figure 52 Data cube 1 Calculated Gas Absorbance

4.2.2. Data set 2

In experiment 4.2.2, Sulfur Hexafluoride and Ethylene are oscillated as controlled.

Number of segments according to the threshold values are given below:

Threshold size 50 => 6056 Threshold size 250 => 3971

Threshold size 500 => 3476 Threshold size 1000 => 3007

As seen in detection results, Algorithm 1 results does not significantly differentiate between 250 segments result and 500 segments result for Sulfur Hexafluoride and Ethylene. It can be observed that algorithm 1 is successful in detection of both Sulfur Hexafluoride and Ethylene gases in the scene. When compared with algorithm 1, algorithm 2 is not as successful as algorithm 1 as hot colors scattered too much in detection of both Sulfur Hexafluoride and Ethylene gases in the scene.

4.2.2.1.Algorithm 1

Table 4 Data cube 2 minCEntropy Results Comparison

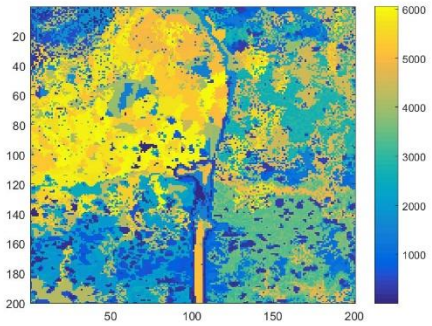

Figure 53 Data cube 2 minCEntropy Results with Threshold 50

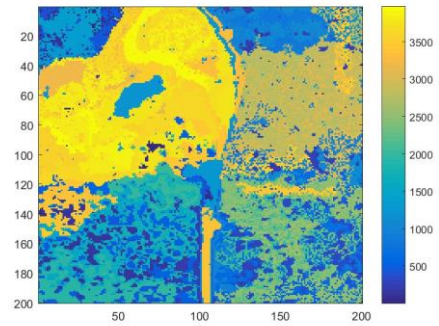

Figure 54 Data cube 2 minCEntropy Results with Threshold 250

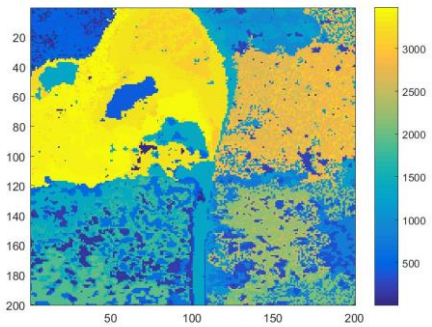

Figure 55 Data cube 2 minCEntropy Results with Threshold 500

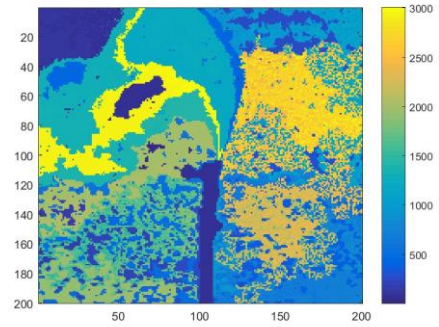

Figure 56 Data cube 2 minCEntropy Results with Threshold 1000

Table 5 Data cube 2 Detection Results Comparison (Sulfur)

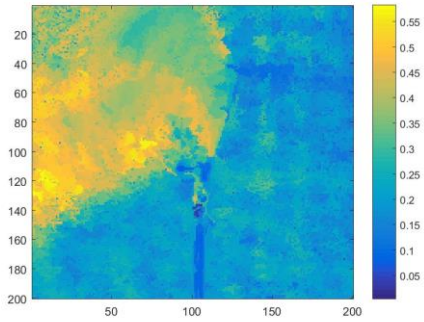

Figure 57 Data cube 2 Detection Results with Threshold 50 (Sulfur)

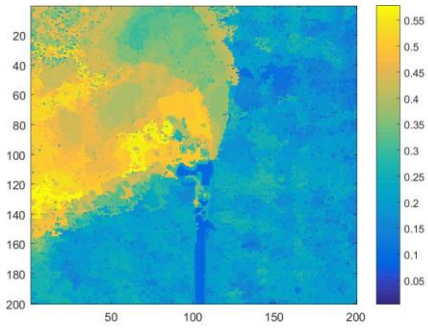

Figure 58 Data cube 2 Detection Results with Threshold 250 (Sulfur)

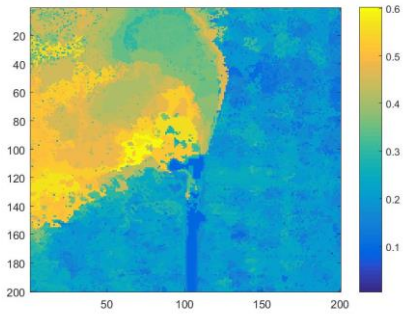

Figure 59 Data cube 2 Detection Results with Threshold 500 (Sulfur)

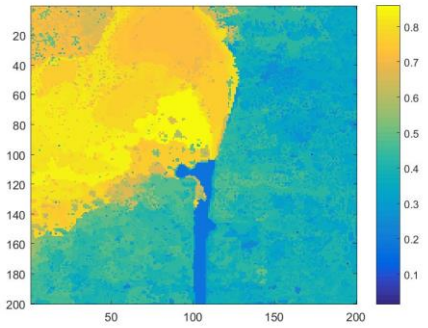

Figure 60 Data cube 2 Detection Results with Threshold 1000 (Sulfur)

Table 6 Data cube 2 Detection Results Comparison (Otsu) (Sulfur)

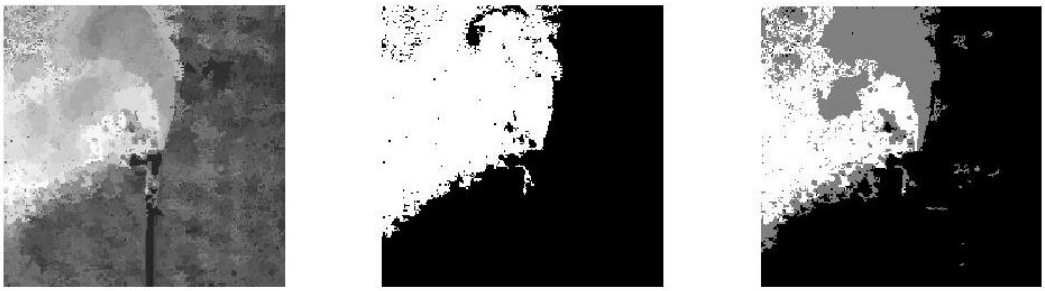

Figure 61 Data cube 2 Detection Results with Threshold 50 (Otsu) (Sulfur)

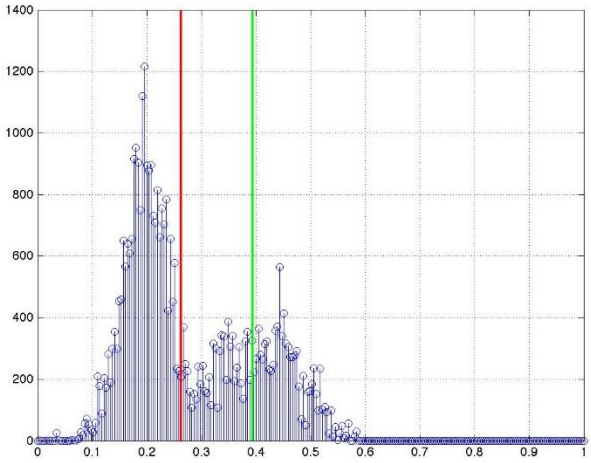

Figure 62 Data cube 2 Detection Results with Threshold 50 (Histogram) (Sulfur)

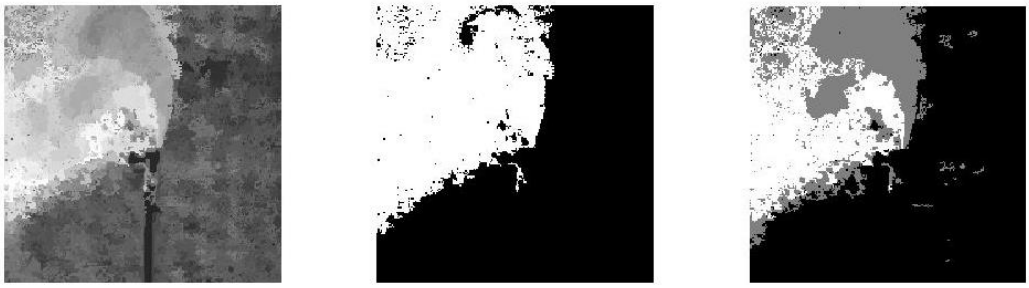

Figure 63 Data cube 2 Detection Results with Threshold 250 (Otsu) (Sulfur)

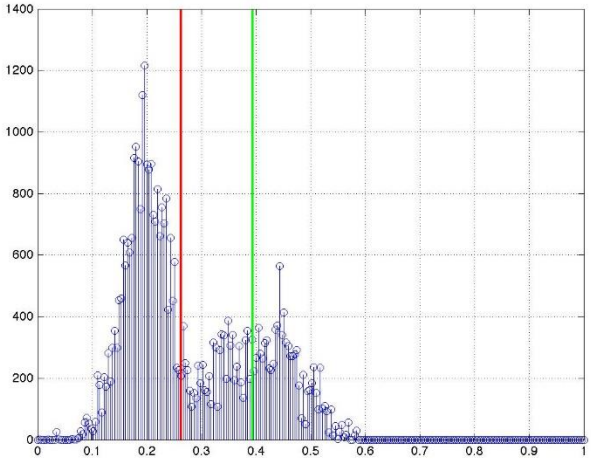

Figure 64 Data cube 2 Detection Results with Threshold 250 (Histogram) (Sulfur)

Figure 65 Data cube 2 Detection Results with Threshold 500 (Otsu) (Sulfur)

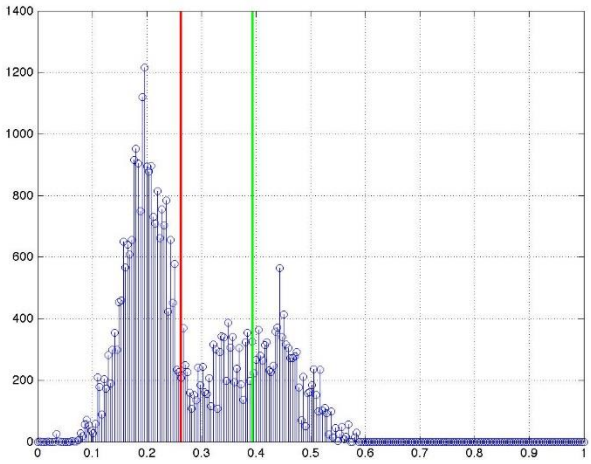

Figure 66 Data cube 2 Detection Results with Threshold 500 (Histogram) (Sulfur)

Figure 67 Data cube 2 Detection Results with Threshold 1000 (Otsu) (Sulfur)

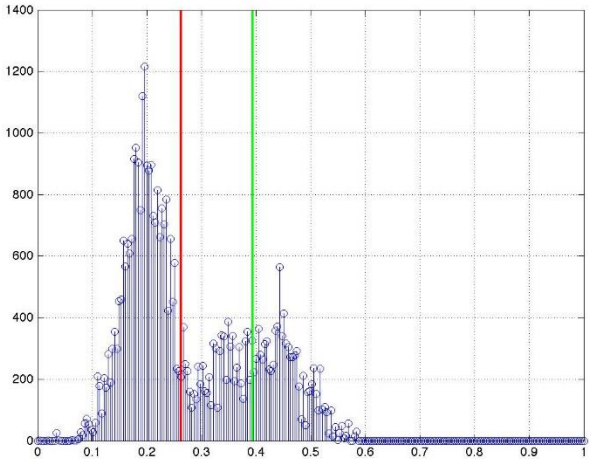

Figure 68 Data cube 2 Detection Results with Threshold 1000 (Histogram) (Sulfur)

Table 7 Data cube 2 Detection Results Comparison (Ethylene)

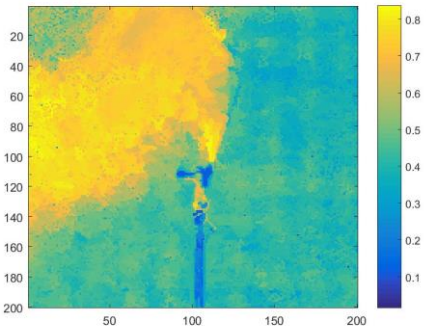

Figure 69 Data cube 2 Detection Results with Threshold 50 (Ethylene)

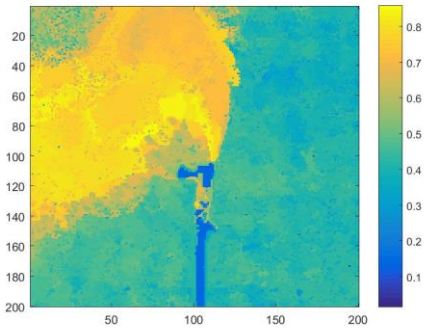

Figure 70 Data cube 2 Detection Results with Threshold 250 (Ethylene)

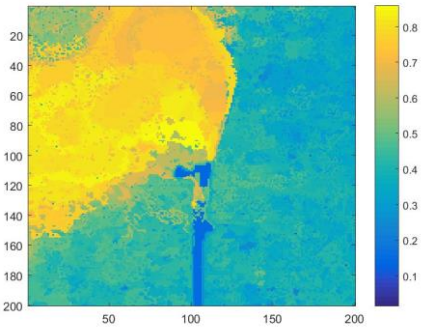

Figure 71 Data cube 2 Detection Results with Threshold 500 (Ethylene)

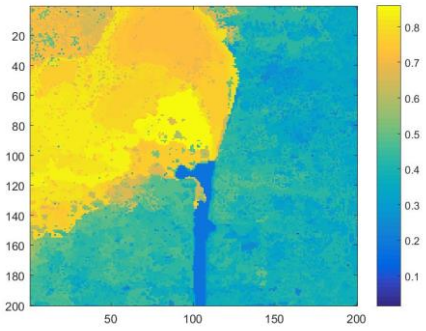

Figure 72 Data cube 2 Detection Results with Threshold 1000 (Ethylene)

Table 8 Data cube 2 Detection Results Comparison (Otsu) (Ethylene)

Figure 73 Data cube 2 Detection Results with Threshold 50 (Otsu) (Ethylene)

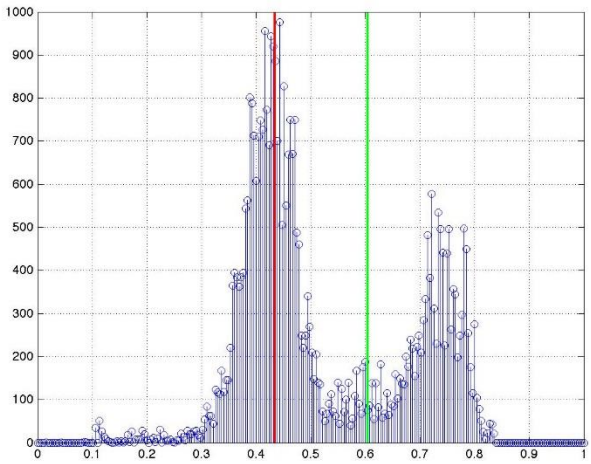

Figure 74 Data cube 2 Detection Results with Threshold 50 (Histogram) (Ethylene)

Figure 75 Data cube 2 Detection Results with Threshold 250 (Otsu) (Ethylene)

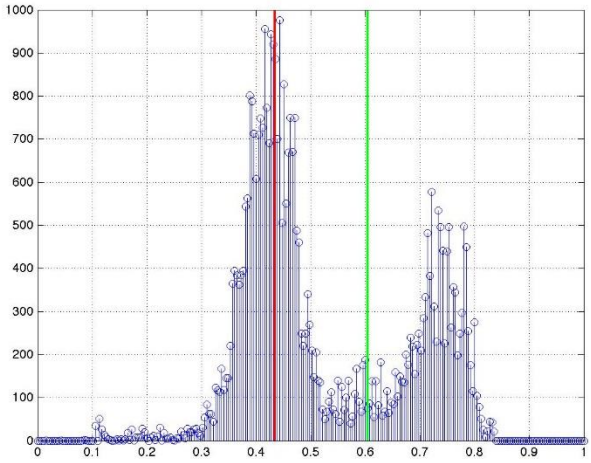

Figure 76 Data cube 2 Detection Results with Threshold 250 (Histogram) (Ethylene)

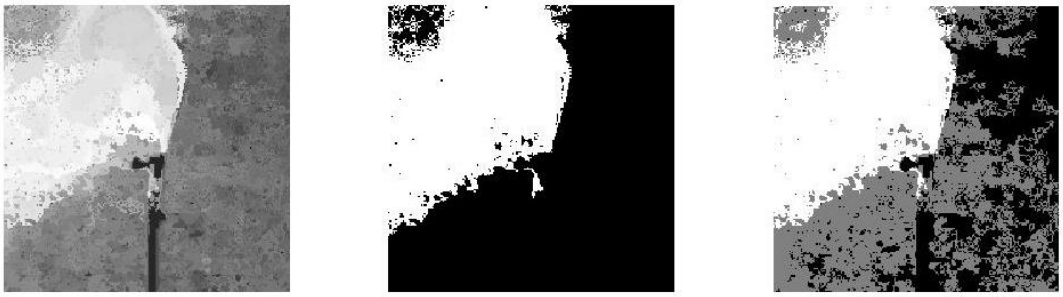

Figure 77 Data cube 2 Detection Results with Threshold 500 (Otsu) (Ethylene)

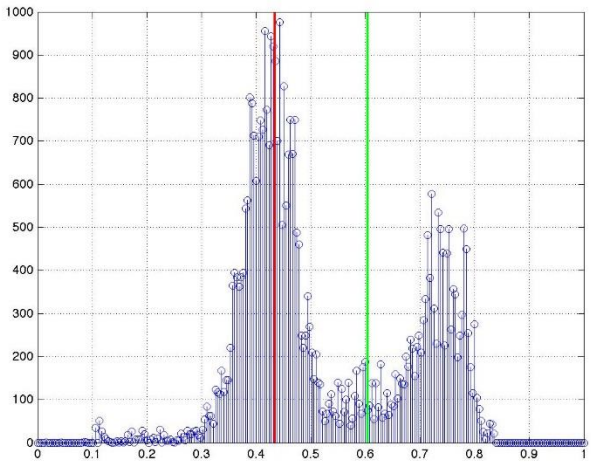

Figure 78 Data cube 2 Detection Results with Threshold 500 (Histogram) (Ethylene)

Figure 79 Data cube 2 Detection Results with Threshold 1000 (Otsu) (Ethylene)

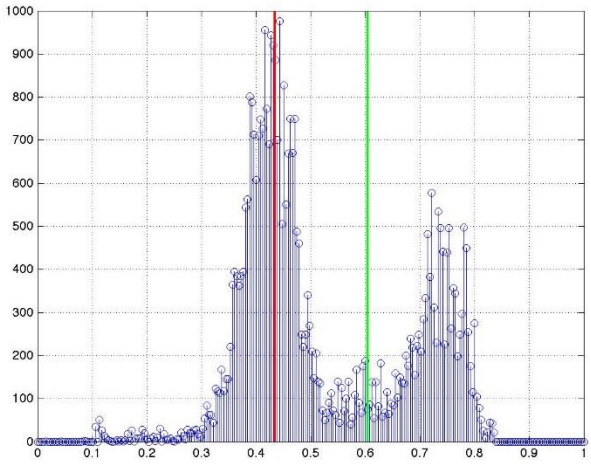

Figure 80 Data cube 2 Detection Results with Threshold 1000 (Histogram) (Ethylene)

4.2.2.2.Algorithm 2

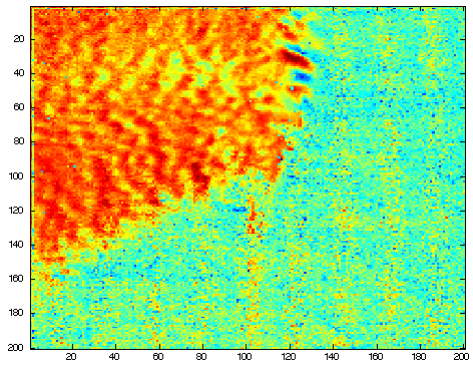

Figure 81 Data cube 1 Detection Results with Algorithm 2 Sulfur Hexafluoride

Figure 82 Data cube 1 Detection Results with Algorithm 2 **Sulfur Hexafluoride** (Otsu)

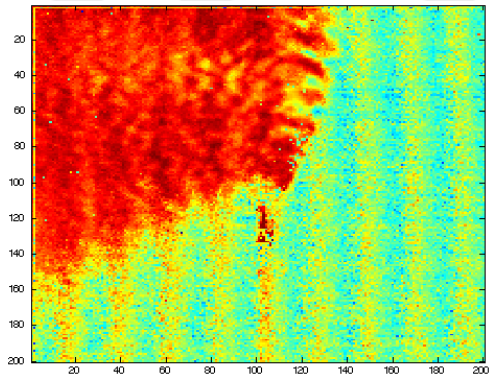

Figure 83 Data cube 2 Detection Results with Algorithm 2 Ethylene

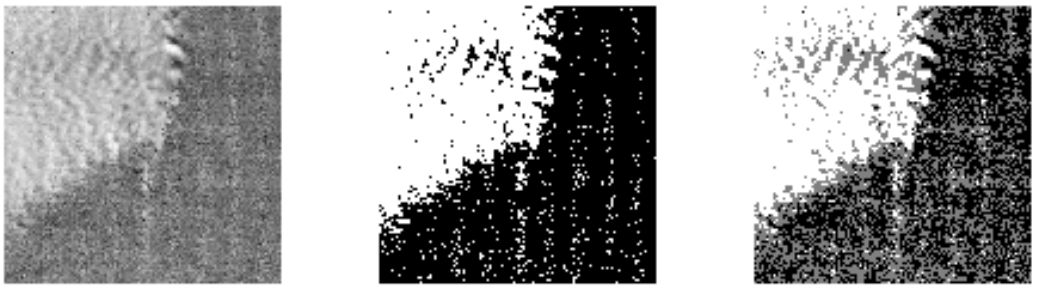

Figure 84 Data cube 2 Detection Results with Algorithm 2 Ethylene (Otsu)

4.2.2.3.Cropped Target Gas Spectrum

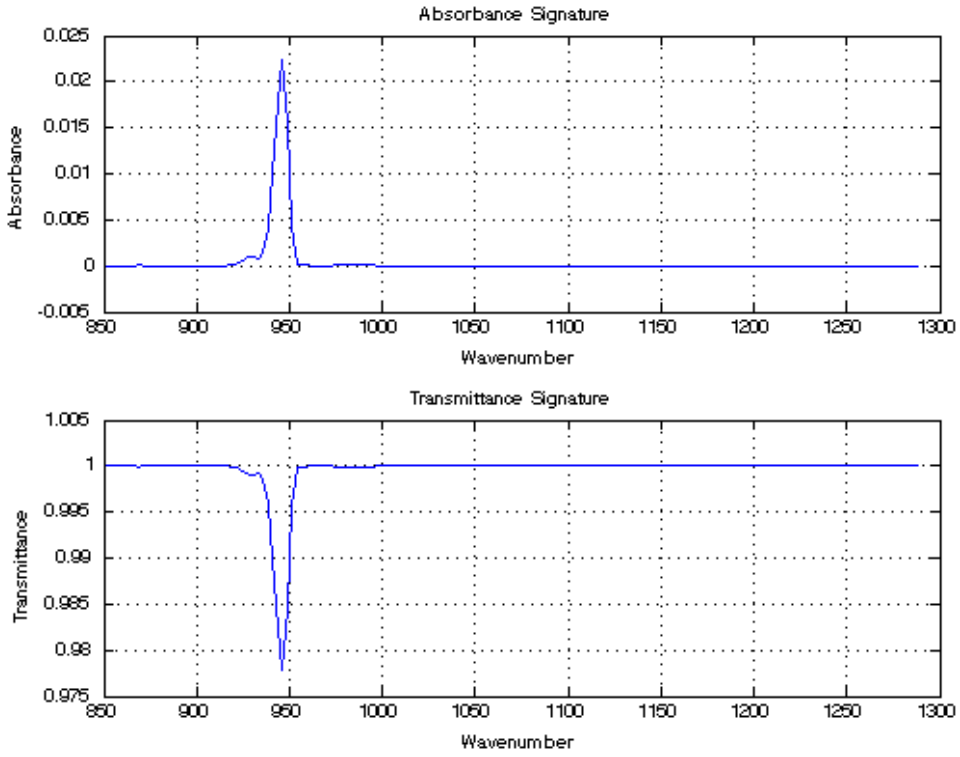

Figure 85 Cropped Target Gas Spectrum Sulfur Hexafluoride

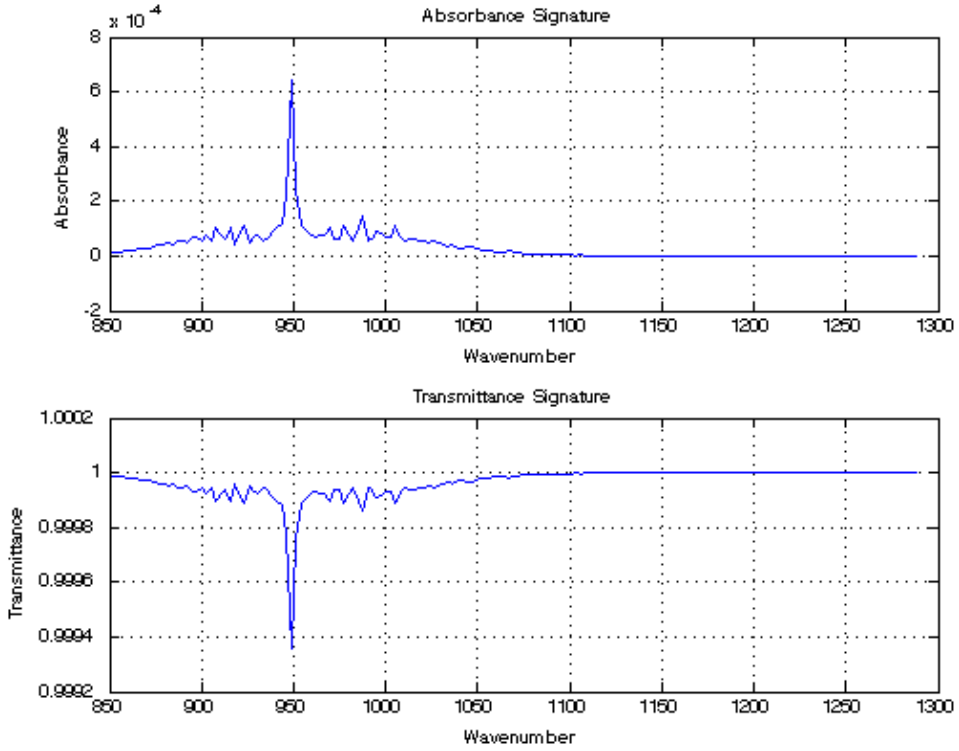

Figure 86 Cropped Target Gas Spectrum Ethylene

4.2.2.4.Background-Gas Including Pixel Spectrums

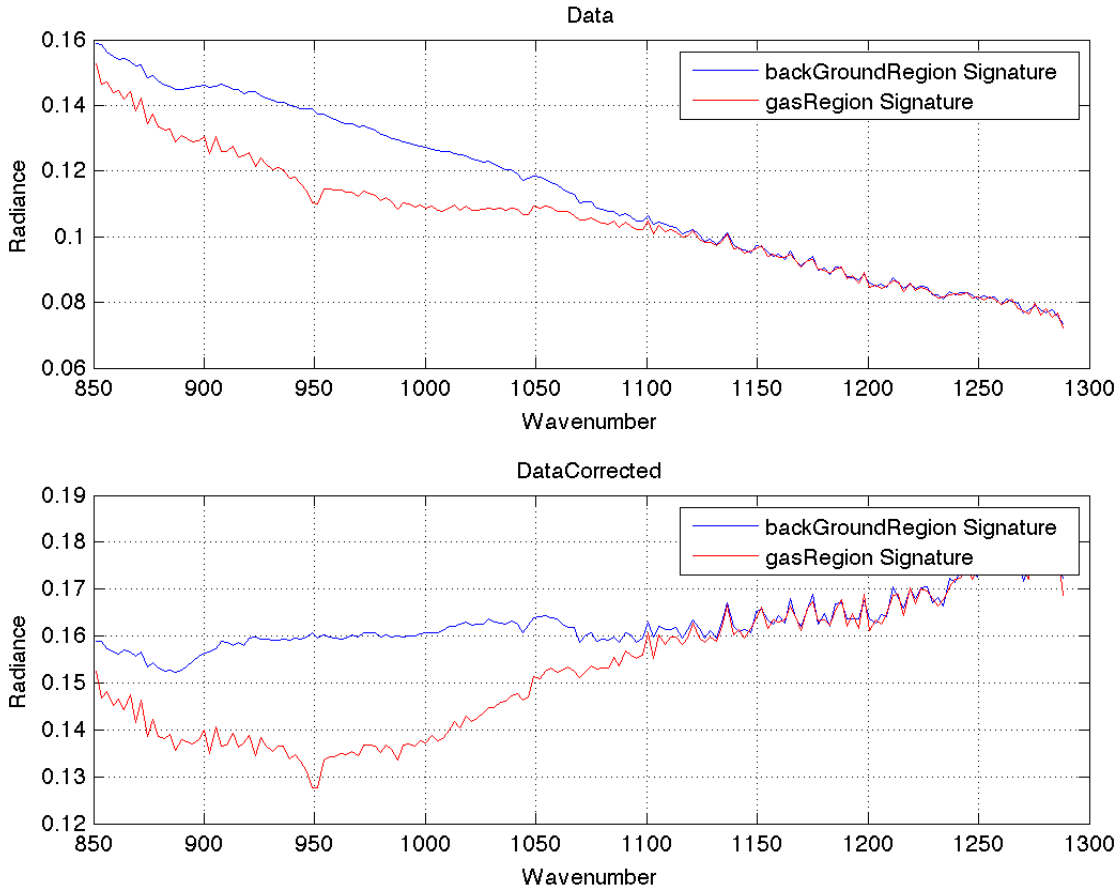

Figure 87 Background&Gas Including Pixel Spectrums

4.2.2.5.Calculated Transmittance and Absorbance Values of Gas Including Pixels

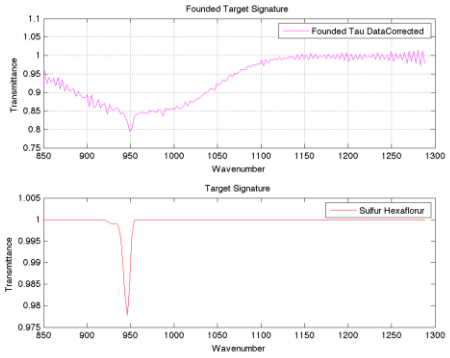

Figure 88 Data cube 2 Calculated Gas Transmittance Sulfur Hexafluoride

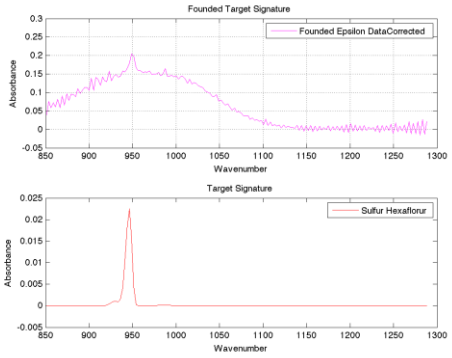

Figure 89 Data cube 2 Calculated Gas Absorbance Sulfur Hexafluoride

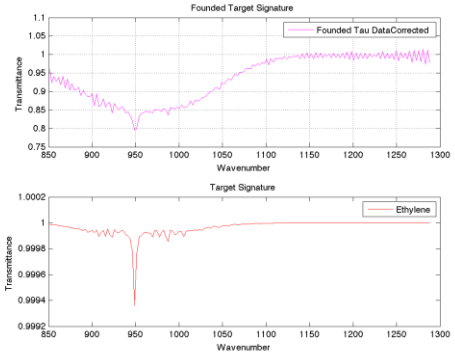

Figure 90 Data cube 2 Calculated Gas Transmittance Ethylene

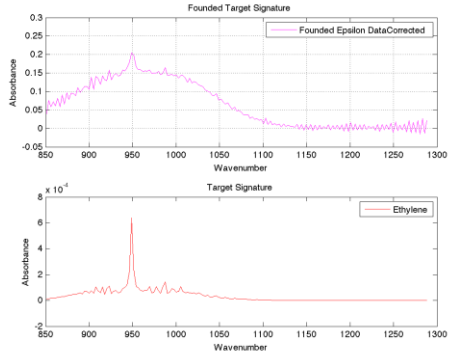

Figure 91 Data cube 2 Calculated Gas Absorbance Ethylene

4.2.3. Data Set 3

In experiment 4.2.3, Butane is oscillated from a cylinder.

Number of segments according to the threshold values are given in below:
Threshold size 50 => 3389 Threshold size 250 => 1741
Threshold size 500 => 1266 Threshold size 1000 => 693

As seen in detection results, Algorithm 1 results does not significantly differentiate between 250 segments result and 500 segments result for Butane. It can be observed that algorithm 1 is successful in detection of Butane gas in the scene. When compared with algorithm 1, algorithm 2 has similar detection results in detection of Butane gas in the scene.

4.2.3.1.Algorithm 1

Table 9 Data cube 3 minCEntropy Results Comparison

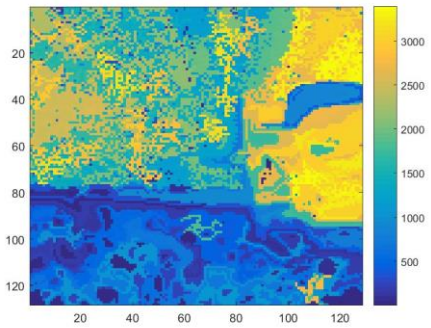

Figure 92 Data cube 3 minCEntropy Results with Threshold 50

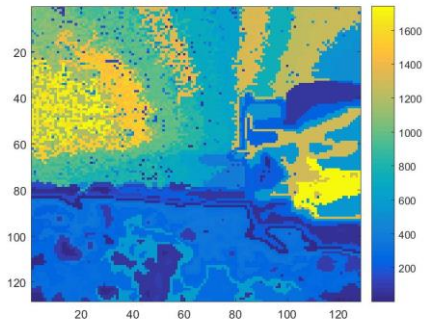

Figure 93 Data cube 3 minCEntropy Results with Threshold 250

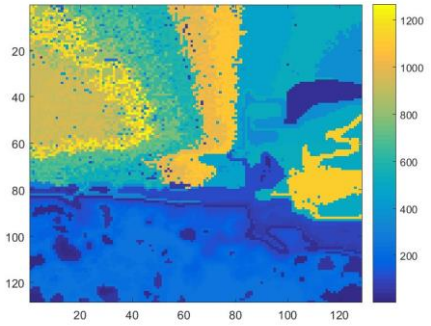

Figure 94 Data cube 3 minCEntropy Results with Threshold 500

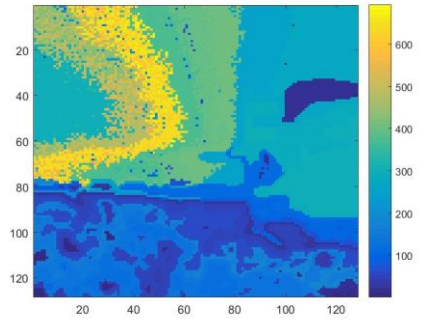

Figure 95 Data cube 3 minCEntropy Results with Threshold 1000

Table 10 Data cube 3 Detection Results Comparison

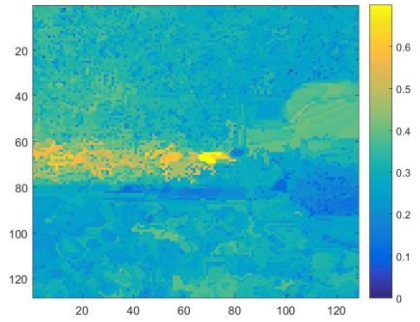

Figure 96 Data cube 3 Detection Results with Threshold 50

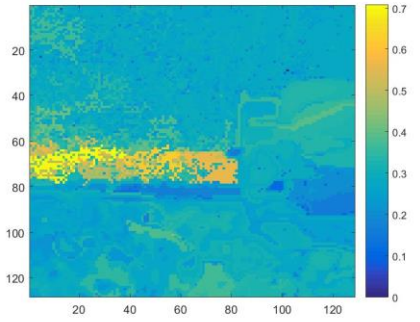

Figure 97 Data cube 3 Detection Results with Threshold 250

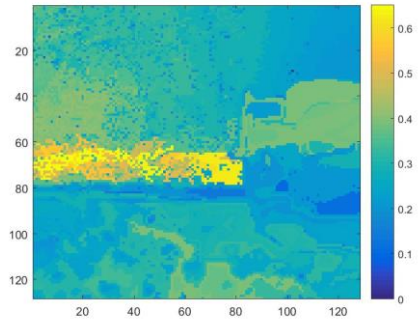

Figure 98 Data cube 3 Detection Results with Threshold 500

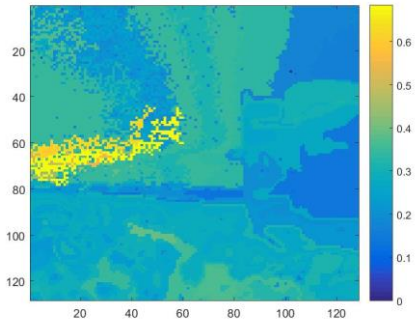

Figure 99 Data cube 3 Detection Results with Threshold 1000

Table 11 Data cube 3 Detection Results Comparison (Otsu)

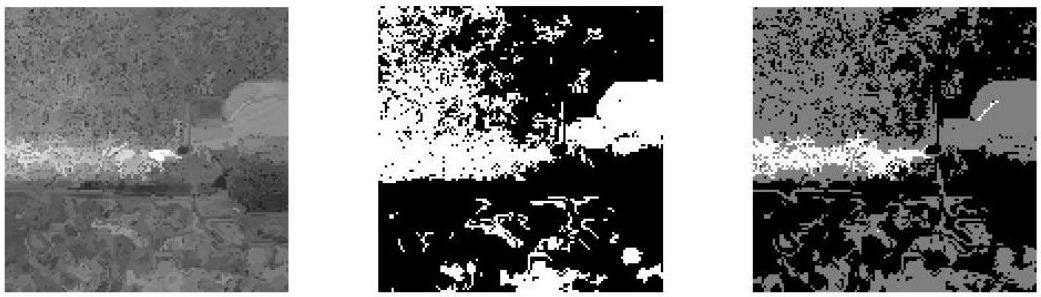

Figure 100 Data cube 3 Detection Results with Threshold 50 (Otsu)

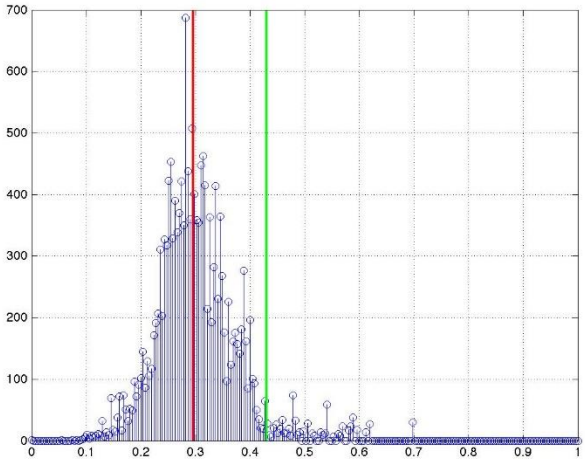

Figure 101 Data cube 3 Detection Results with Threshold 50 (Histogram)

Figure 102 Data cube 3 Detection Results with Threshold 250 (Otsu)

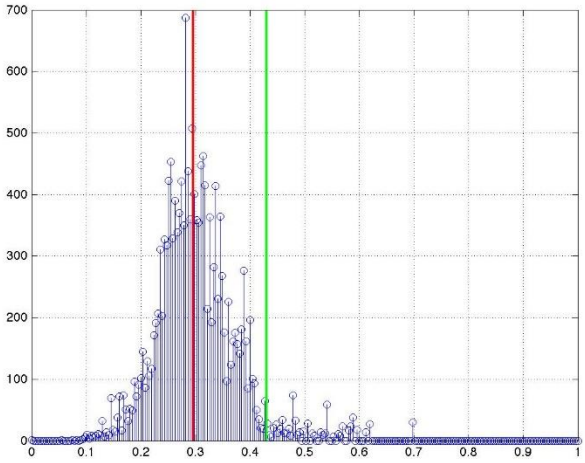

Figure 103 Data cube 3 Detection Results with Threshold 250 (Histogram)

Figure 104 Data cube 3 Detection Results with Threshold 500 (Otsu)

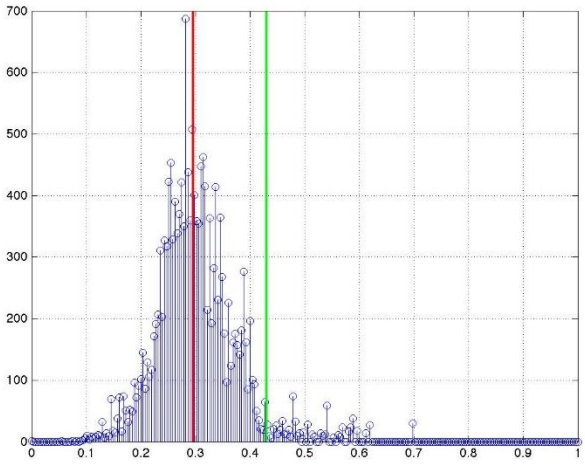

Figure 105 Data cube 3 Detection Results with Threshold 500 (Histogram)

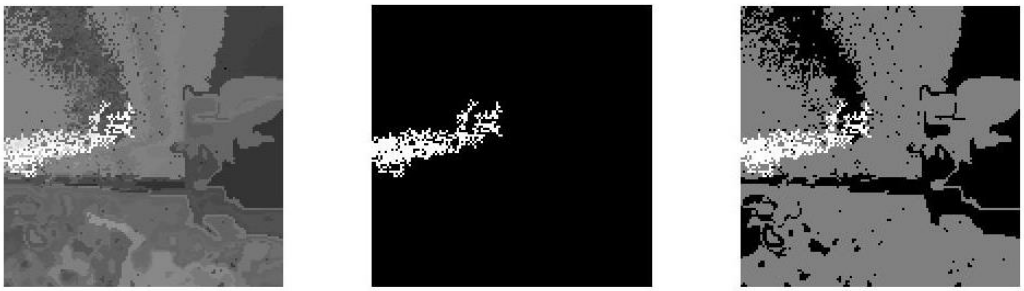

Figure 106 Data cube 3 Detection Results with Threshold 1000 (Otsu)

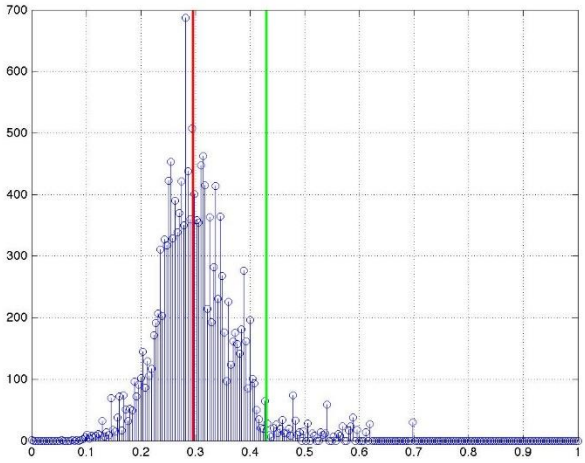

Figure 107 Data cube 3 Detection Results with Threshold 1000 (Histogram)

4.2.3.2.Algorithm 2

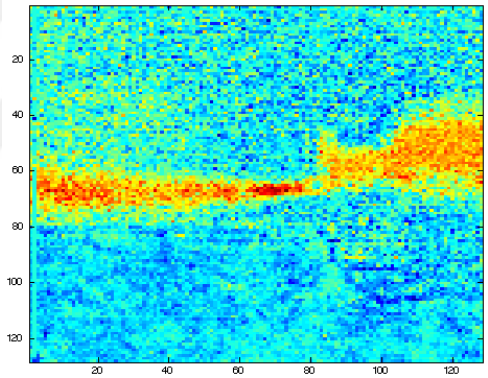

Figure 108 Data cube 3 Detection Results with Algorithm 2

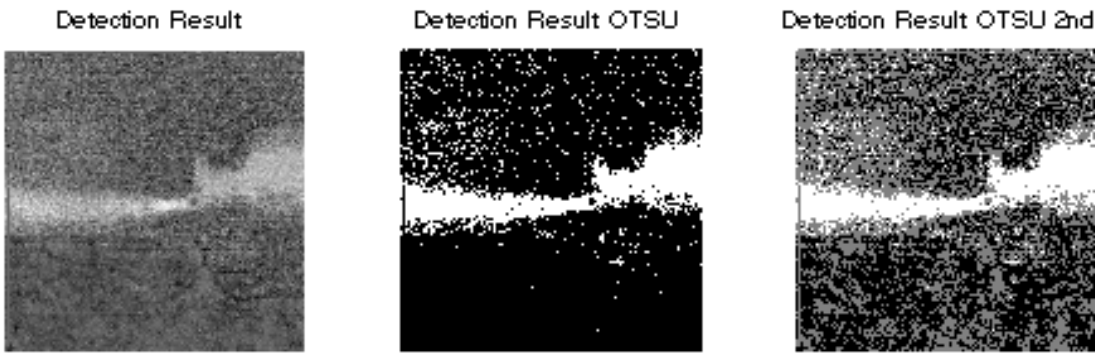

Figure 109 Data cube 3 Detection Results with Algorithm 2 (Otsu)

4.2.3.3.Cropped Target Gas Spectrum

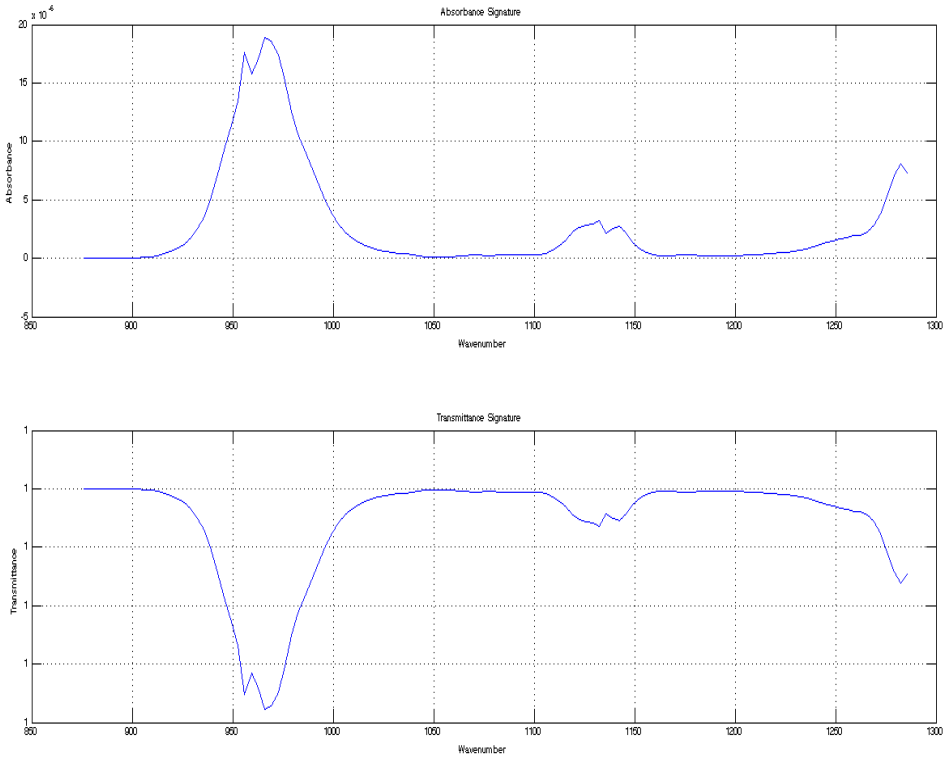

Figure 110 Cropped Target Gas Spectrum Butane

4.2.3.4.Background-Gas Including Pixel Spectrums

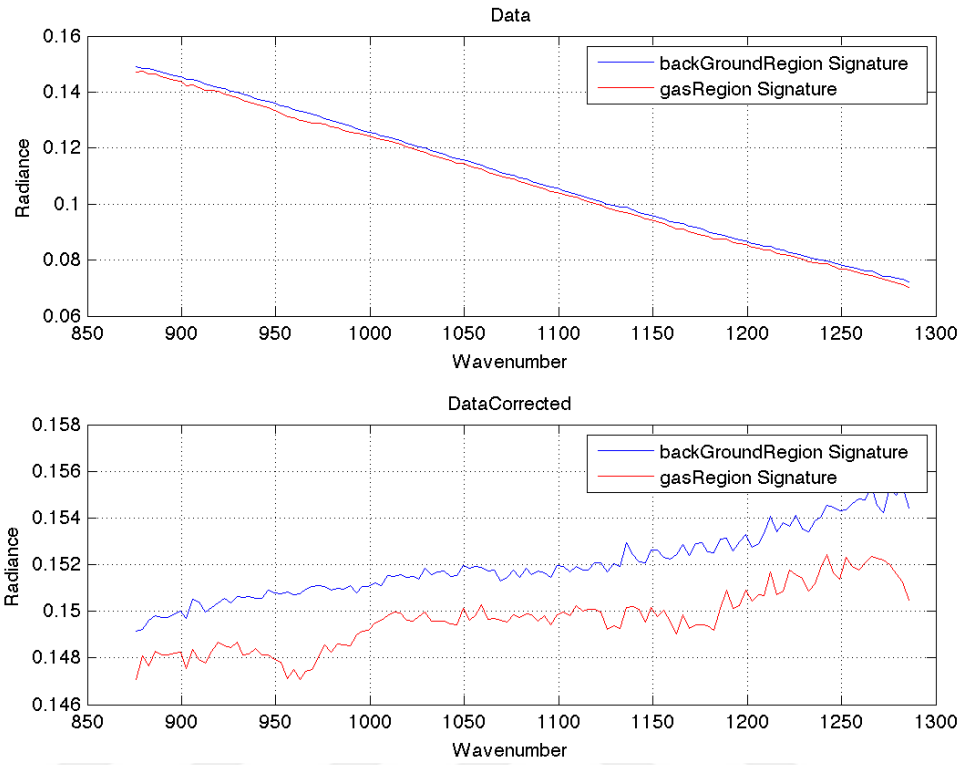

Figure 111 Background&Gas Including Pixel Spectrums

4.2.3.5.Calculated Transmittance and Absorbance Values of Gas Including Pixels

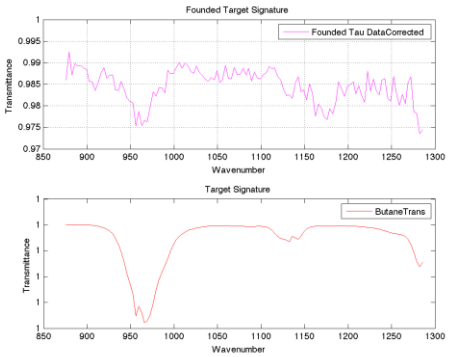

Figure 112 Data cube 3 Calculated Gas Transmittance

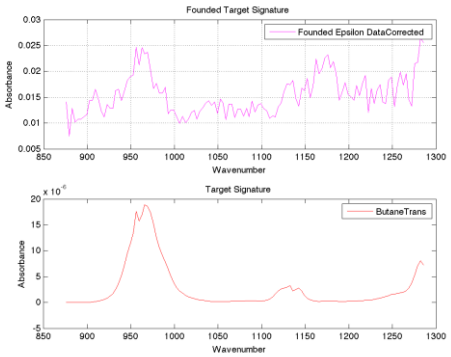

Figure 113 Data cube 3 Calculated Gas Absorbance

4.2.4. Data set 4

In experiment 4.2.4, same scene condition is used as experiment 4.2.3; but there is not any gas oscillated from a cylinder.

Number of segments according to the threshold values are given below:

Threshold size 50	=> 3445	Threshold size 250	=> 1652
Threshold size 500	=> 1270	Threshold size 1000	=> 751

As seen in detection results, Algorithm 1 results do not significantly differentiate between 250 segments result and 500 segments result for Butane. It can be observed that both algorithm 1 and algorithm 2 does not detect any butane gas in the scene as it should be. This situation proves that both detection results are reliable as in the same scene conditions they can detect if gas is oscillated or not.

4.2.4.1.Algorithm 1

Table 12 Data cube 4 minCEntropy Results Comparison

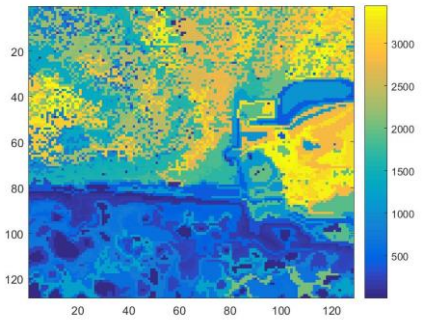

Figure 114 Data cube 4 minCEntropy Results with Threshold 50

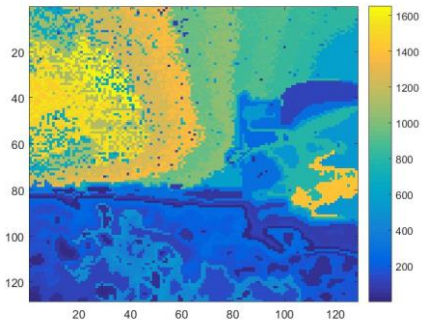

Figure 115 Data cube 4 minCEntropy Results with Threshold 250

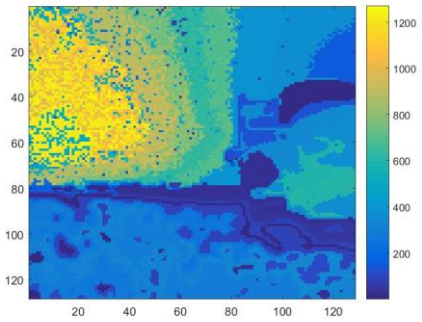

Figure 116 Data cube 4 minCEntropy Results with Threshold 500

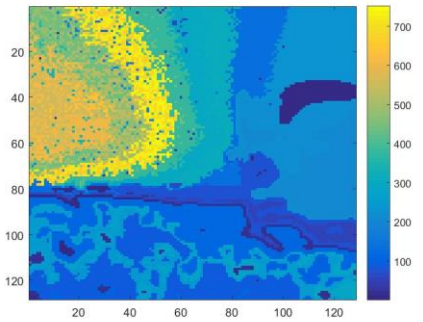

Figure 117 Data cube 4 minCEntropy Results with Threshold 1000

Table 13 Data cube 4 Detection Results Comparison

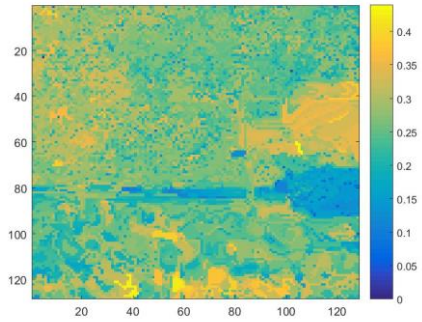

Figure 118 Data cube 4 Detection Results with Threshold 50

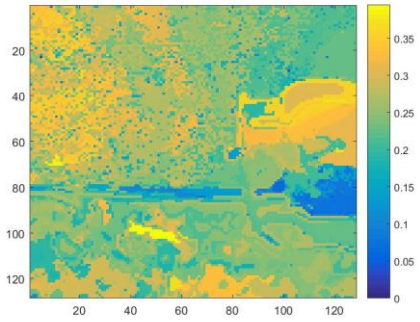

Figure 119 Data cube 4 Detection Results with Threshold 250

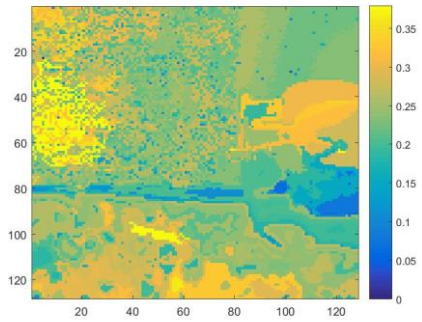

Figure 120 Data cube 4 Detection Results with Threshold 500

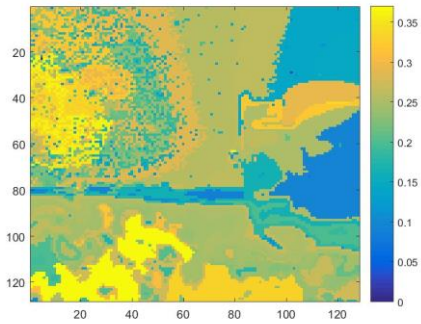

Figure 121 Data cube 4 Detection Results with Threshold 1000

Table 14 Data cube 4 Detection Results Comparison (Otsu)

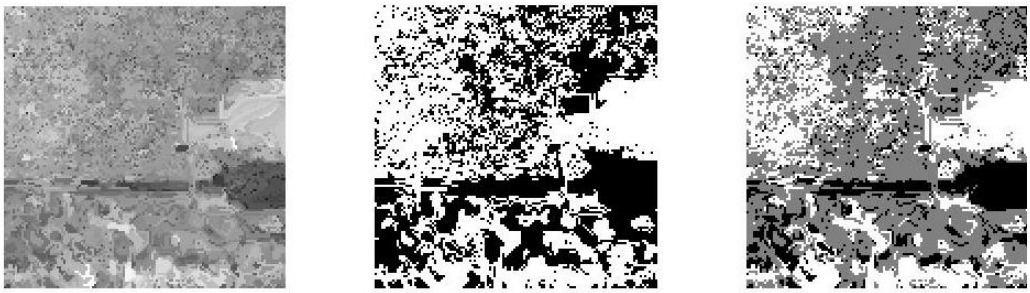

Figure 122 Data cube 4 Detection Results with Threshold 50 (Otsu)

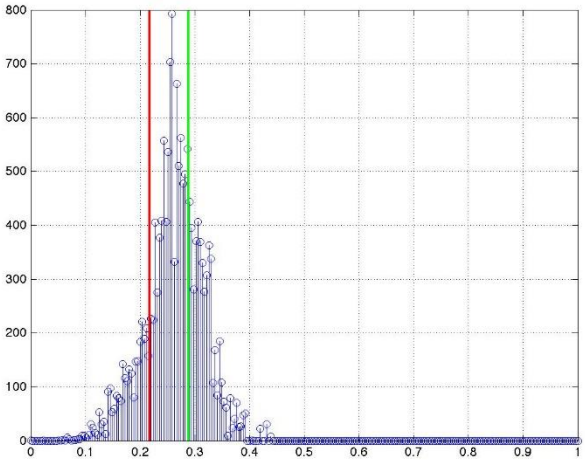

Figure 123 Data cube 4 Detection Results with Threshold 50 (Histogram)

Figure 124 Data cube 4 Detection Results with Threshold 250 (Otsu)

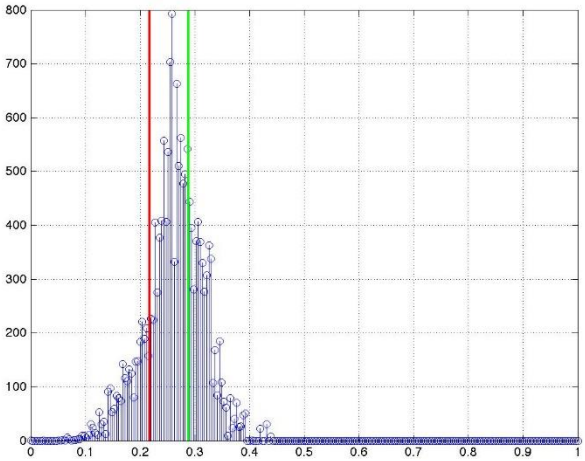

Figure 125 Data cube 4 Detection Results with Threshold 250 (Histogram)

Figure 126 Data cube 4 Detection Results with Threshold 500 (Otsu)

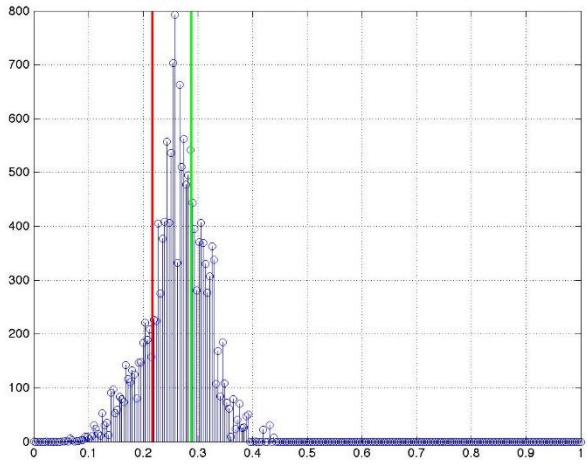

Figure 127 Data cube 4 Detection Results with Threshold 500 (Histogram)

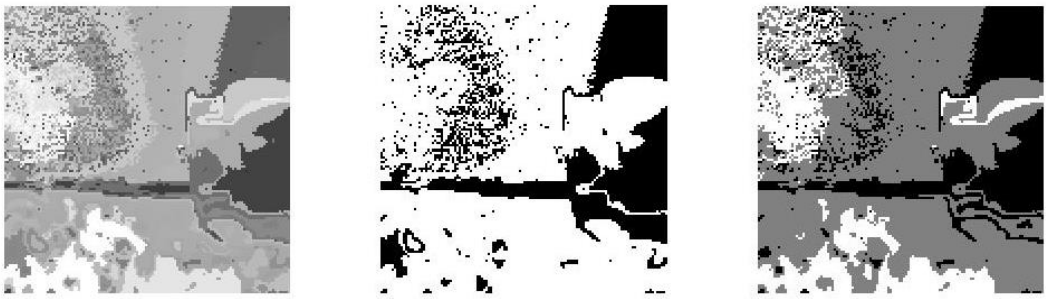

Figure 128 Data cube 4 Detection Results with Threshold 1000 (Otsu)

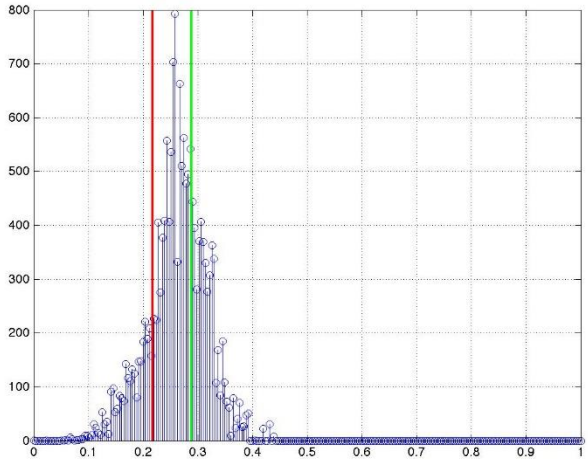

Figure 129 Data cube 4 Detection Results with Threshold 1000 (Histogram)

4.2.4.2.Algorithm 2

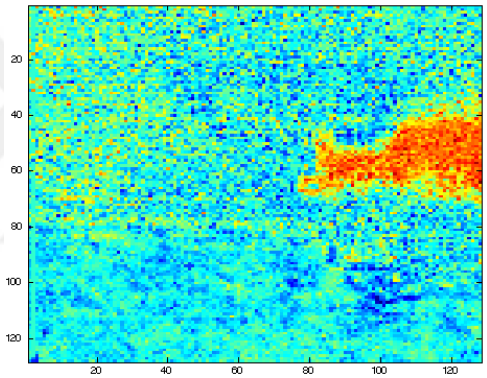

Figure 130 Data cube 4 Detection Results with Algorithm 2

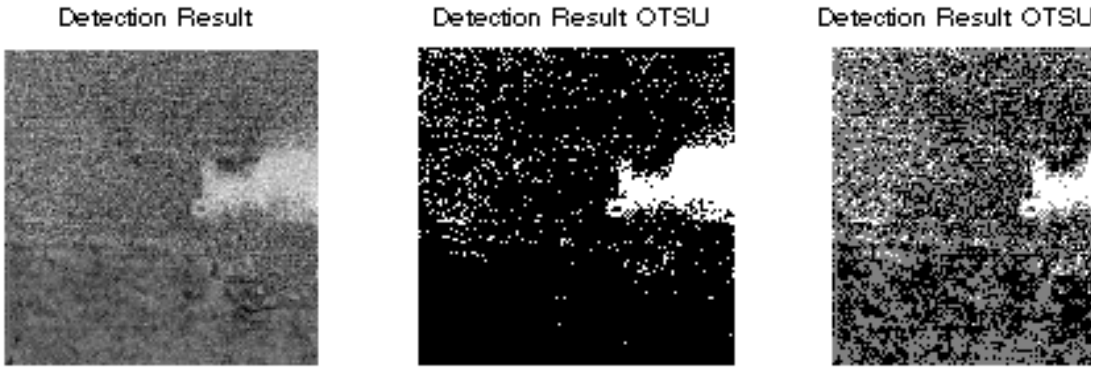

Figure 131 Data cube 4 Detection Results with Algorithm 2 (Otsu)

4.2.4.3.Cropped Target Gas Spectrum

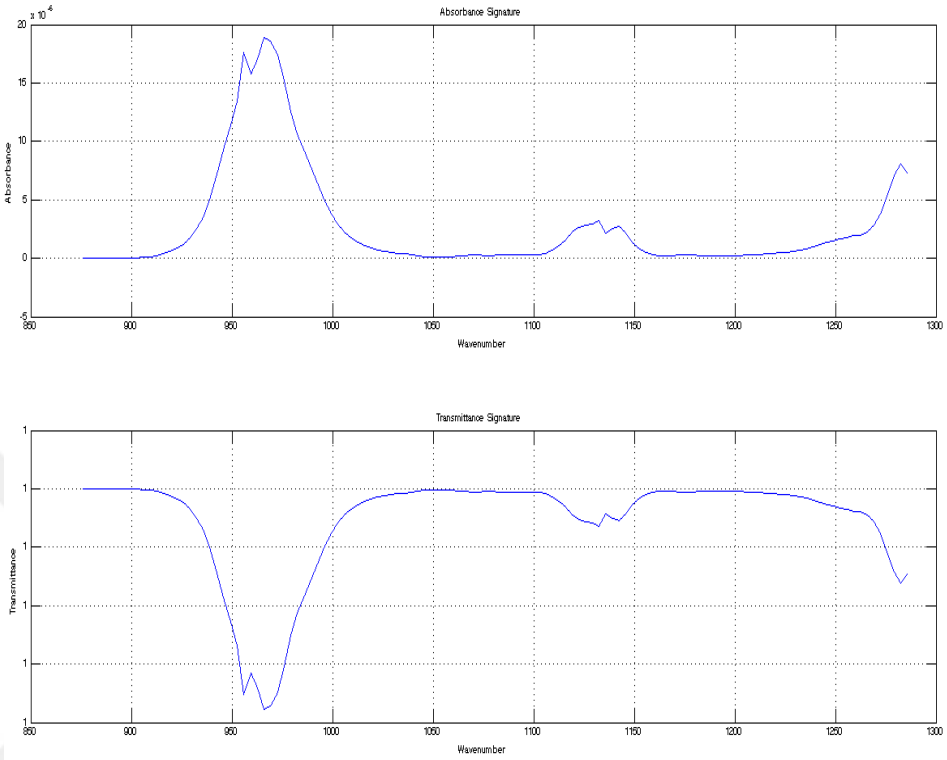

Figure 132 Cropped Target Gas Spectrum

4.2.4.4.Background-Gas Including Pixel Spectrums

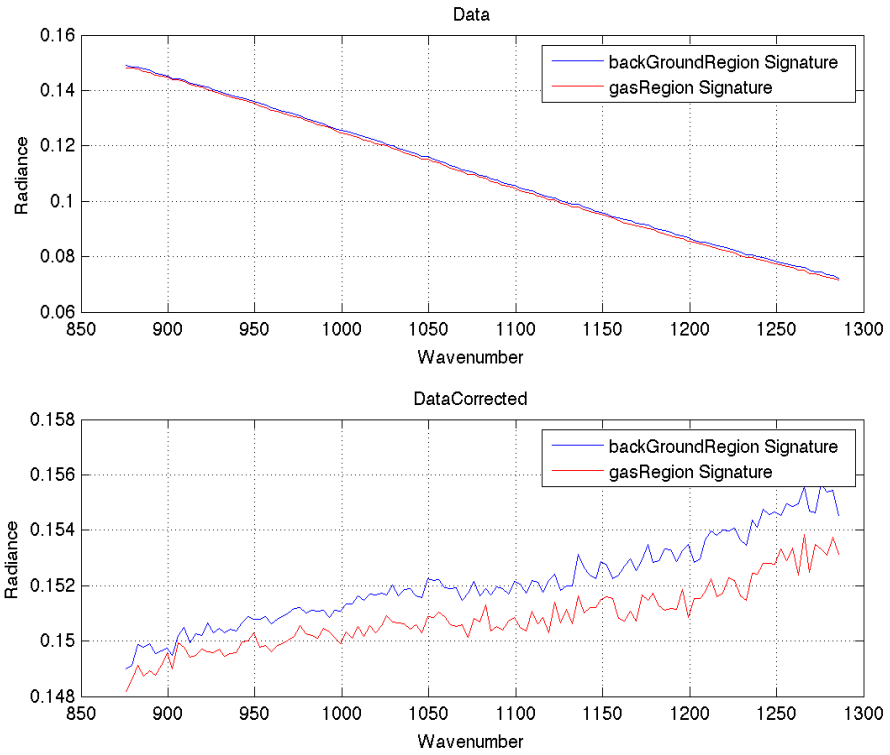

Figure 133 Background&Gas Including Pixel Spectrums

4.2.4.5.Calculated Transmittance and Absorbance Values of Gas Including Pixels

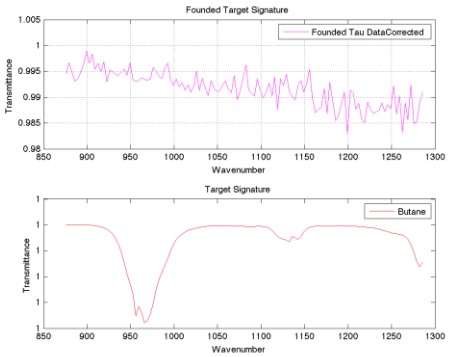

Figure 134 Data cube 4 Calculated Gas Transmittance

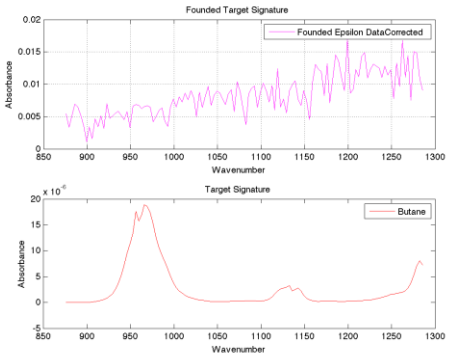

Figure 135 Data cube 4 Calculated Gas Absorbance

4.2.5. Data set 5

In experiment 4.2.5, carbon dioxide is oscillated from a cylinder.

Number of segments according to the threshold values are given below:

Threshold size 50	=> 10335	Threshold size 250	=> 8930
Threshold size 500	=> 8875	Threshold size 1000	=> 8830

It can be observed that algorithm 1 results are unsatisfactory in detection of carbon dioxide gas in general. On the other hand, better results achieved according to the 500 segments and 1000 segments results. When compared with algorithm 1, algorithm 2 has similar results in detection of carbon dioxide gas in the scene but detected segments are scattered excessively. It is evaluated that the reason of detection failure is about the carbon dioxide characteristics. Atmosphere initially has widely carbon dioxide and also atmospheric transmittance values are almost zero on the spectral bands (2300 cm^{-1} – 2400 cm^{-1}), given in figure 29, that carbon dioxide depicts distinguishing characteristics therefore it gets difficult to differentiate the gas from background. Even tough Algorithm 1 results are consistent with reality it needs to be improved.

4.2.5.1.Algorithm 1

Table 15 Data cube 5 minCEntropy Results Comparison

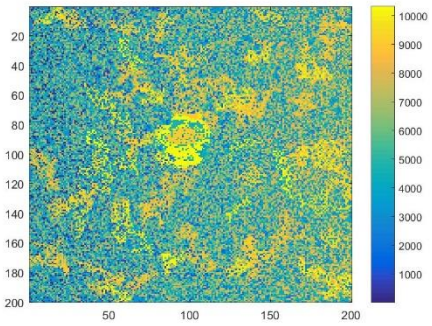

Figure 136 Data cube 5 minCEntropy Results with Threshold 50

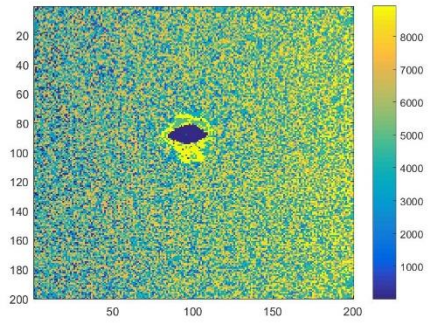

Figure 137 Data cube 5 minCEntropy Results with Threshold 250

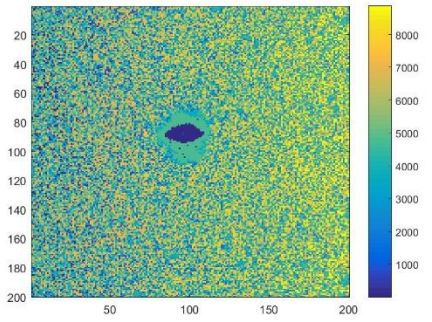

Figure 138 Data cube 5 minCEntropy Results with Threshold 500

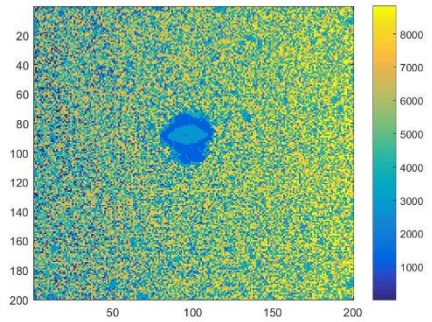

Figure 139 Data cube 5 minCEntropy Results with Threshold 1000

Table 16 Data cube 5 Detection Results Comparison

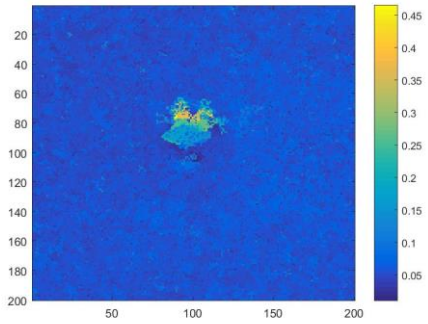

Figure 140 Data cube 5 Detection Results with Threshold 50

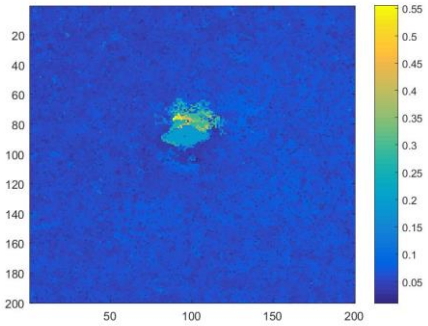

Figure 141 Data cube 5 Detection Results with Threshold 250

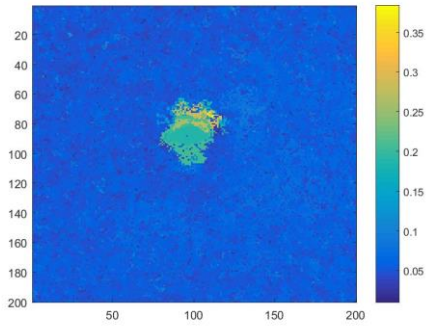

Figure 142 Data cube 5 Detection Results with Threshold 500

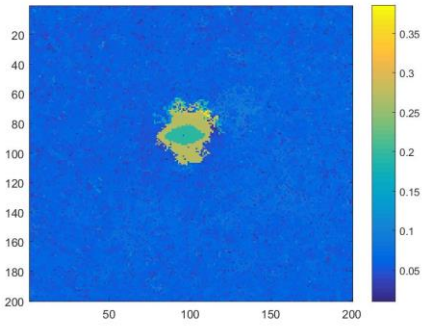

Figure 143 Data cube 5 Detection Results with Threshold 1000

Table 17 Data cube 5 Detection Results Comparison (Otsu)

Figure 144 Data cube 5 Detection Results with Threshold 50 (Otsu)

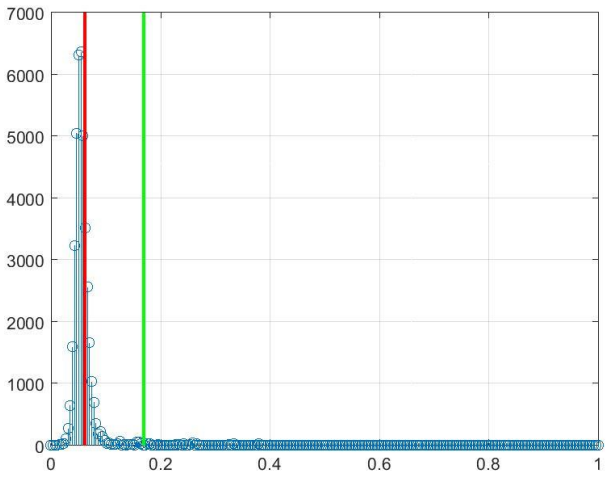

Figure 145 Data cube 5 Detection Results with Threshold 50 (Histogram)

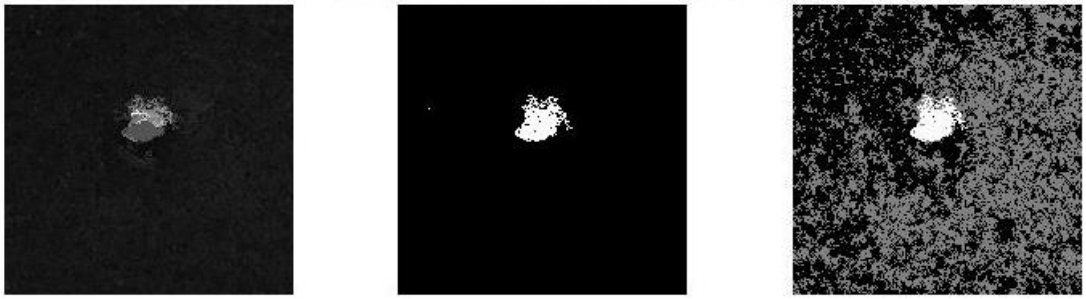

Figure 146 Data cube 5 Detection Results with Threshold 250 (Otsu)

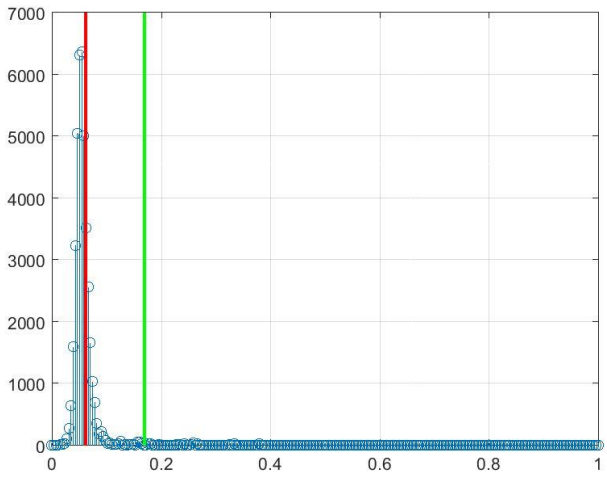

Figure 147 Data cube 5 Detection Results with Threshold 250 (Histogram)

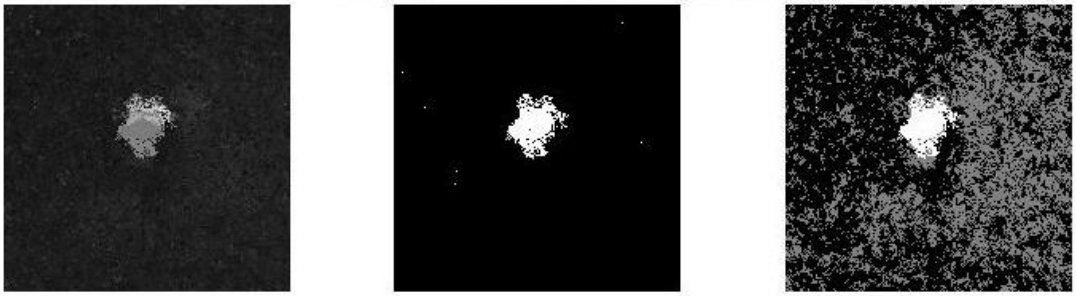

Figure 148 Data cube 5 Detection Results with Threshold 500 (Otsu)

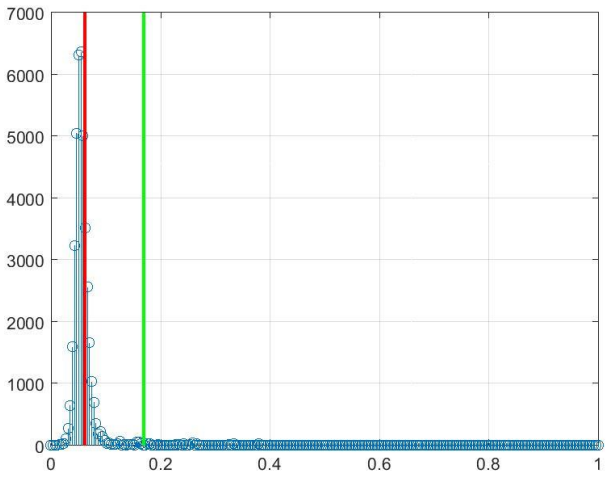

Figure 149 Data cube 5 Detection Results with Threshold 500 (Histogram)

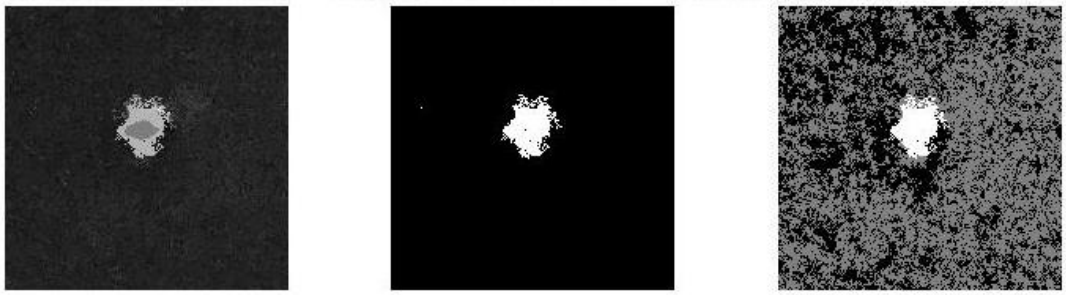

Figure 150 Data cube 5 Detection Results with Threshold 1000 (Otsu)

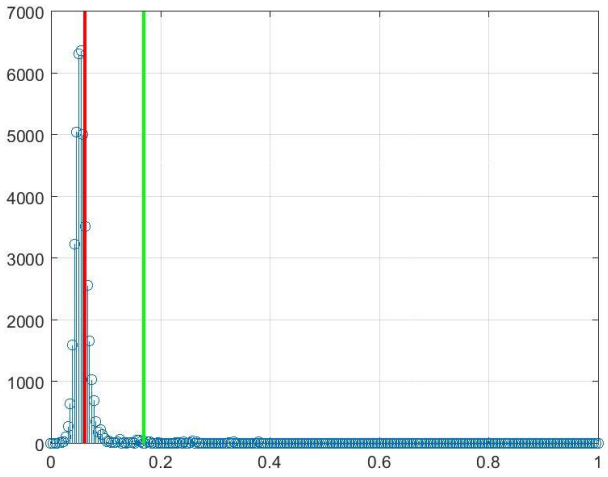

Figure 151 Data cube 5 Detection Results with Threshold 1000 (Histogram)

4.2.5.2.Algorithm 2

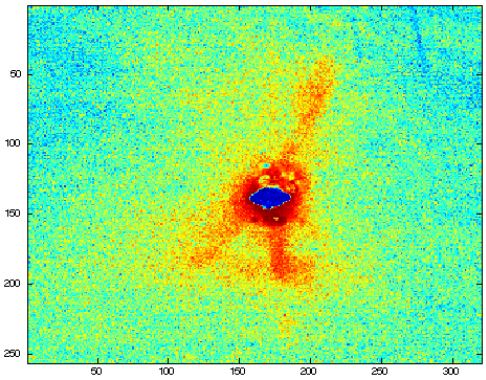

Figure 152 Data cube 5 Detection Results with Algorithm 2

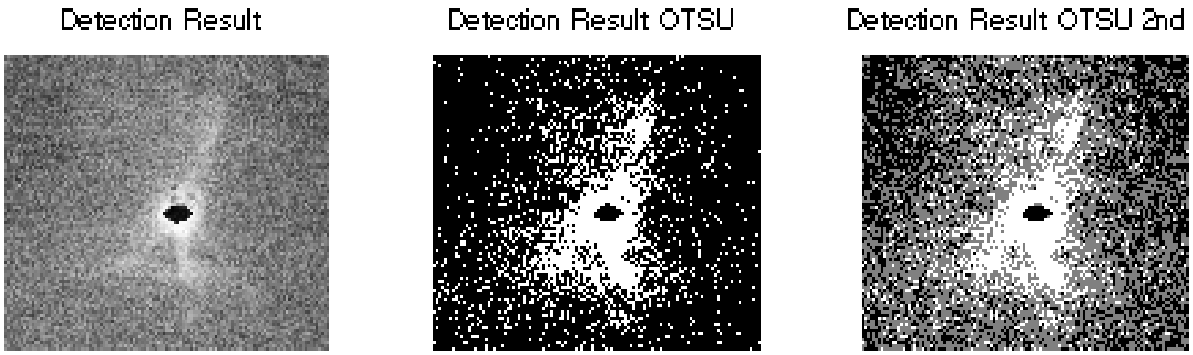

Figure 153 Data cube 5 Detection Results with Algorithm 2 (Otsu)

4.2.5.3.Cropped Target Gas Spectrum

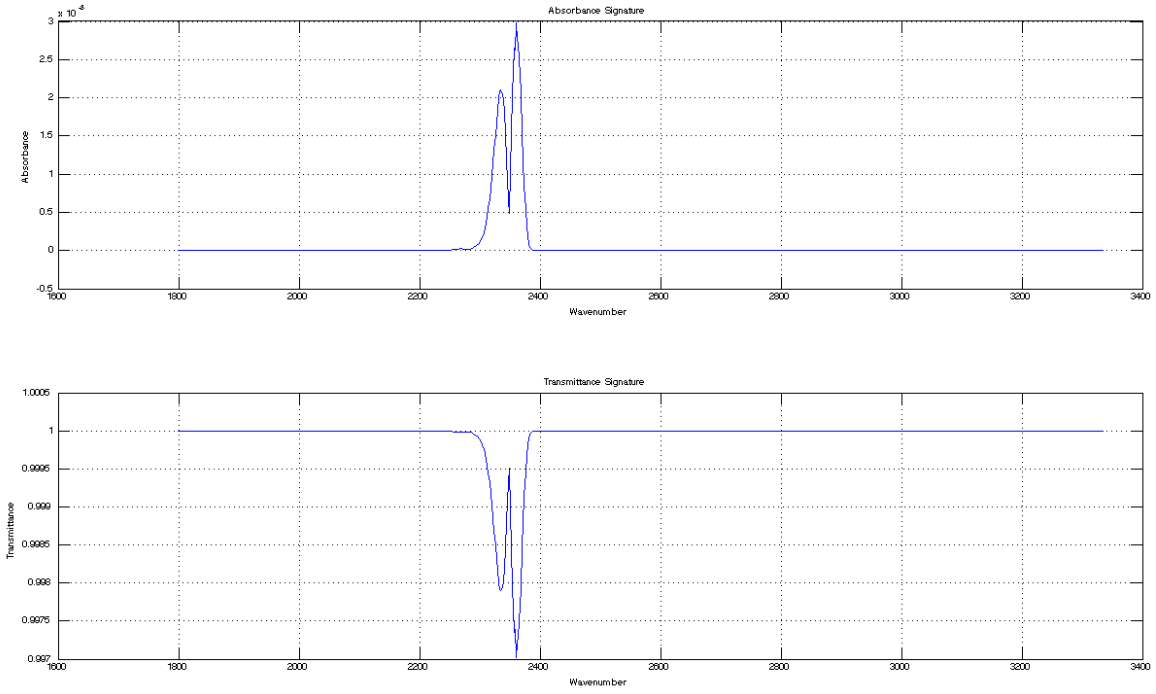

Figure 154 Cropped Target Gas Spectrum

4.2.5.4.Background-Gas Including Pixel Spectrums

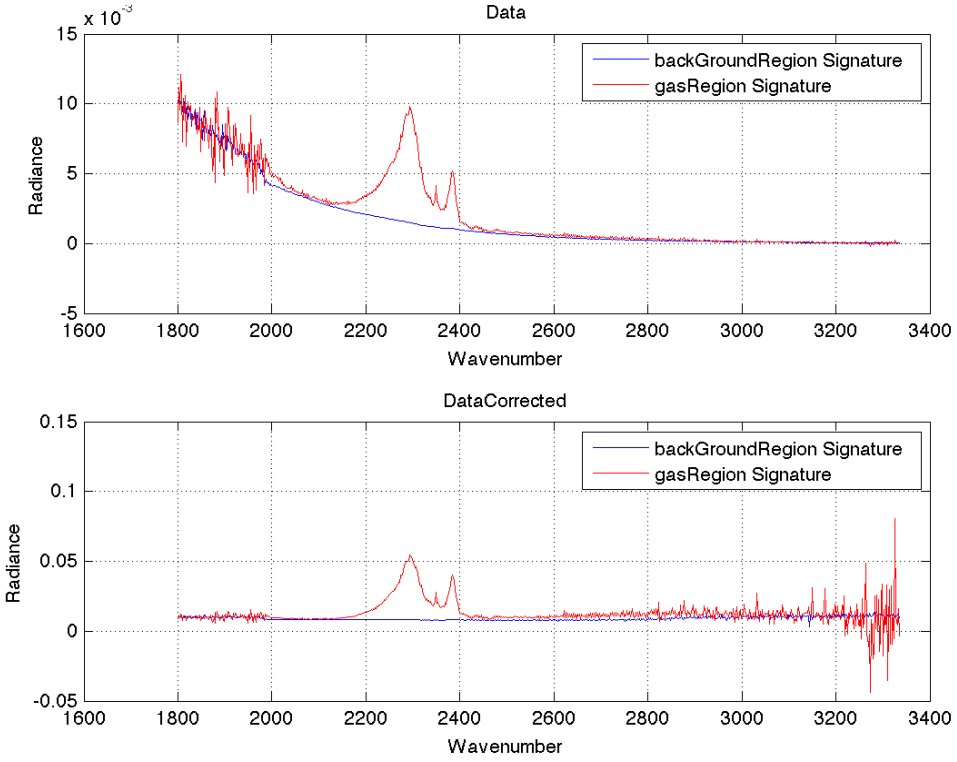

Figure 155 Background&Gas Including Pixel Spectrums

4.2.5.5.Calculated Transmittance and Absorbance Values of Gas Including Pixels

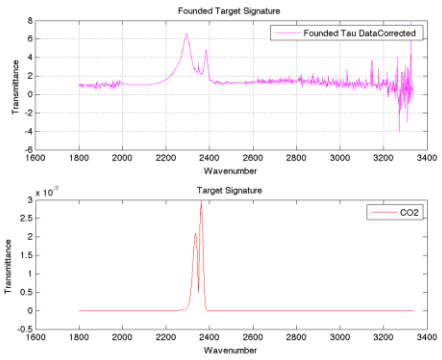

Figure 156 Data cube 5 Calculated Gas Transmittance

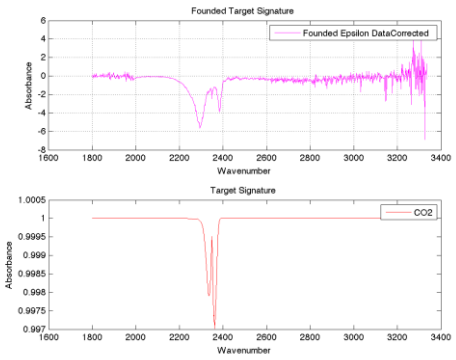

Figure 157 Data cube 5 Calculated Gas Absorbance

4.2.6. Data set 6

In experiment 4.2.6, carbon dioxide is oscillated from a car exhaust.

Number of segments according to the threshold values are given below:

Threshold size 50	=> 6286	Threshold size 250	=> 3488
Threshold size 500	=> 2432	Threshold size 1000	=> 1749

As seen in detection results, Algorithm 1 results do not significantly differentiate according to the segment sizes. It can be observed that algorithm 1 is unsuccessful in detection of carbon dioxide gas in the scene. When compared with algorithm 1, algorithm 2 is also unsuccessful but better than algorithm 1 results in detection of carbon dioxide gas in the scene. It can be observed that target gas is detected with high false alarm rate. It is evaluated that the reason of detection failure is about the carbon dioxide characteristics. Atmosphere initially has widely carbon dioxide and also atmospheric transmittance values are almost zero on the spectral bands (2300 cm^{-1} – 2400 cm^{-1}), given in figure 29, that carbon dioxide depicts distinguishing characteristics therefore it gets difficult to differentiate the gas from background. Also, the temperature difference which directly effects the detection rate can be very low.

4.2.6.1.Algorithm 1

Table 18 Data cube 6 minCEntropy Results Comparison

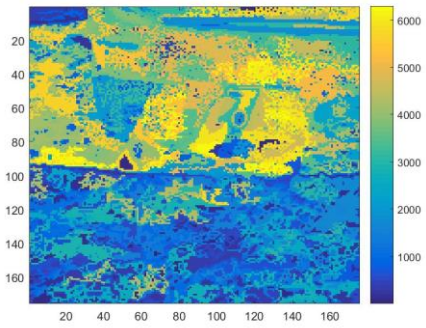

Figure 158 Data cube 6 minCEntropy Results with Threshold 50

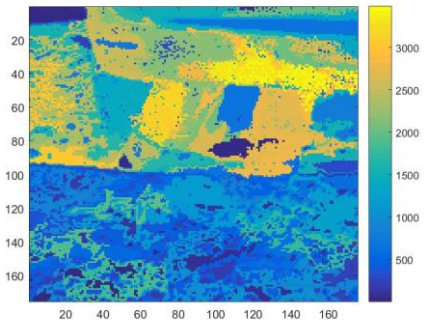

Figure 159 Data cube 6 minCEntropy Results with Threshold 250

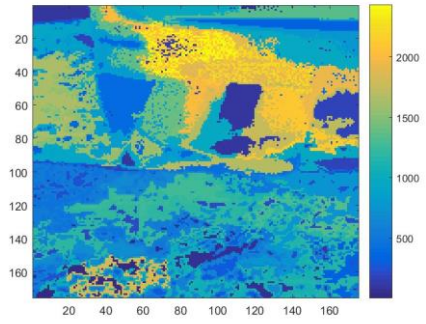

Figure 160 Data cube 6 minCEntropy Results with Threshold 500

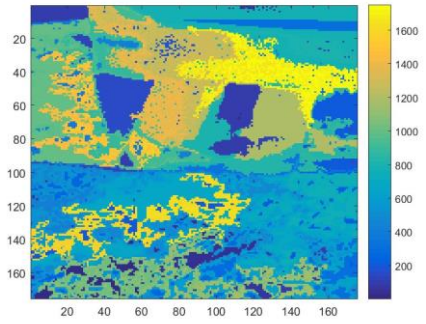

Figure 161 Data cube 6 minCEntropy Results with Threshold 1000

Table 19 Data cube 6 Detection Results Comparison

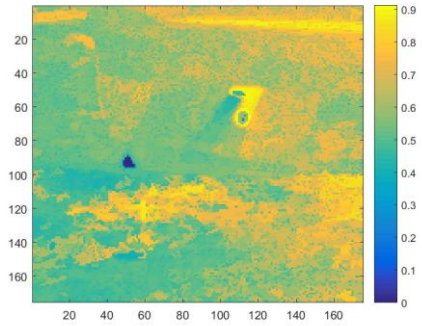

Figure 162 Data cube 6 Detection Results with Threshold 50

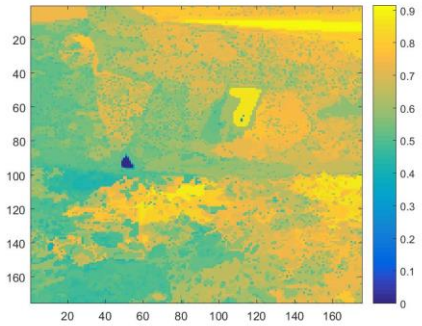

Figure 163 Data cube 6 Detection Results with Threshold 250

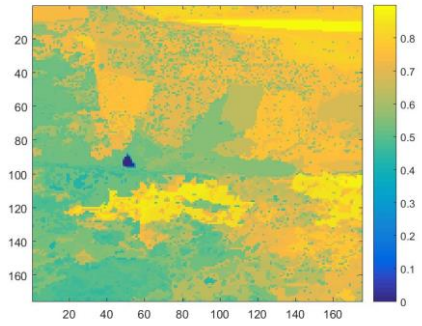

Figure 164 Data cube 6 Detection Results with Threshold 500

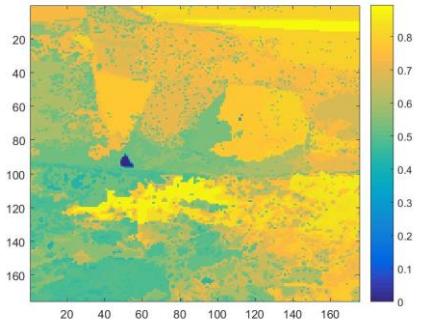

Figure 165 Data cube 6 Detection Results with Threshold 1000

Table 20 Data cube 6 Detection Results Comparison (Otsu)

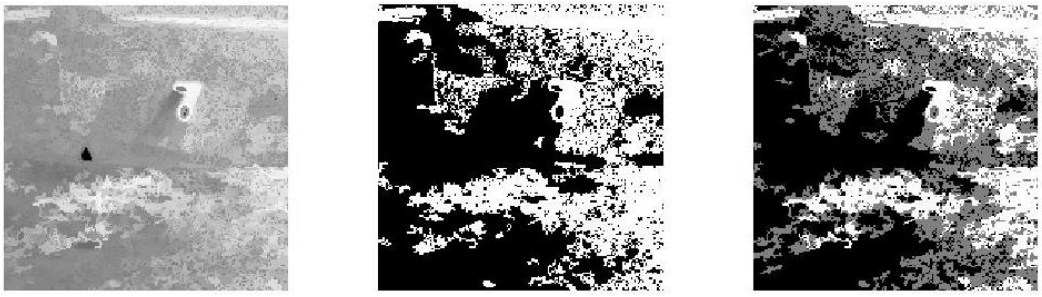

Figure 166 Data cube 6 Detection Results with Threshold 50 (Otsu)

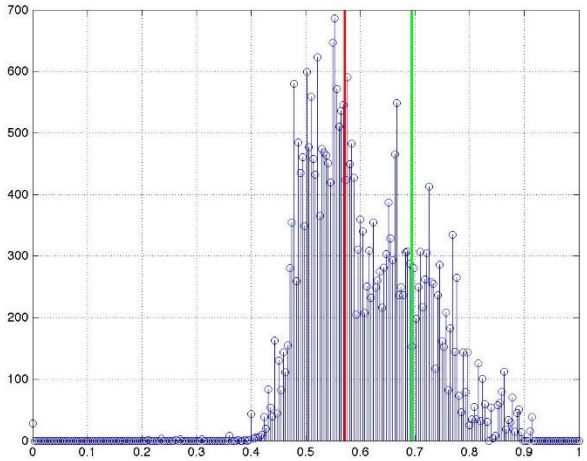

Figure 167 Data cube 6 Detection Results with Threshold 50 (Histogram)

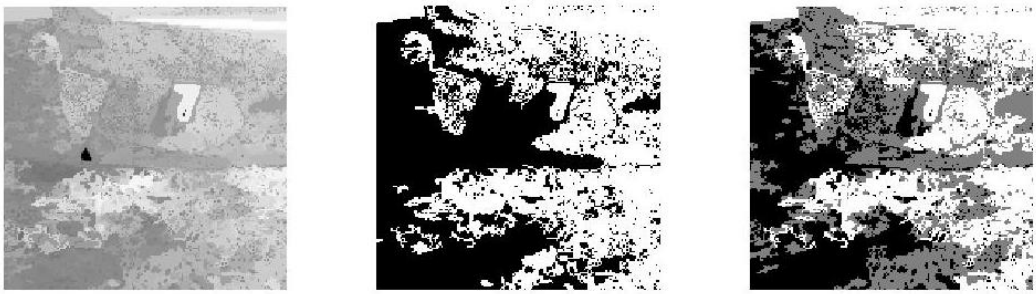

Figure 168 Data cube 6 Detection Results with Threshold 250 (Otsu)

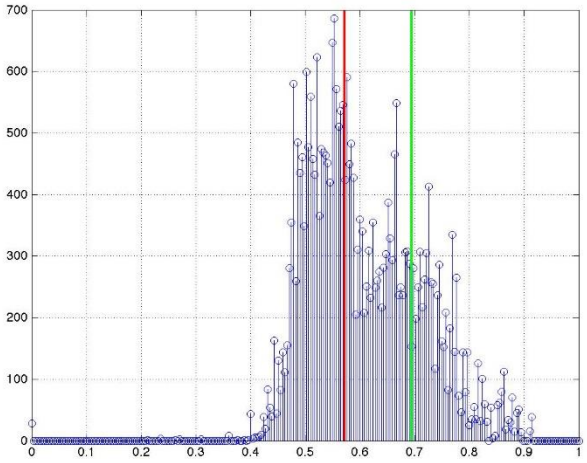

Figure 169 Data cube 6 Detection Results with Threshold 250 (Histogram)

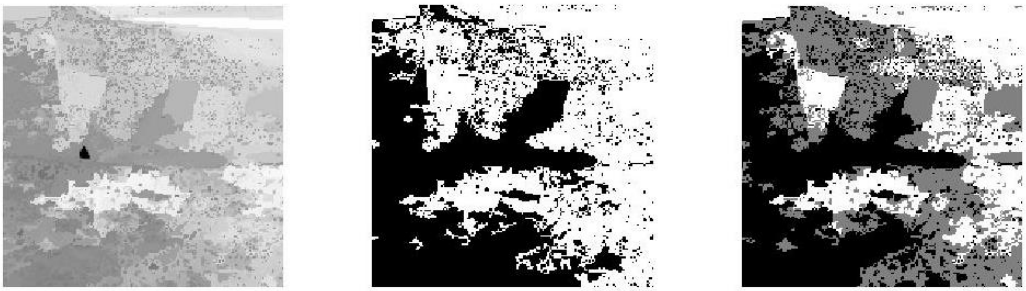

Figure 170 Data cube 6 Detection Results with Threshold 500 (Otsu)

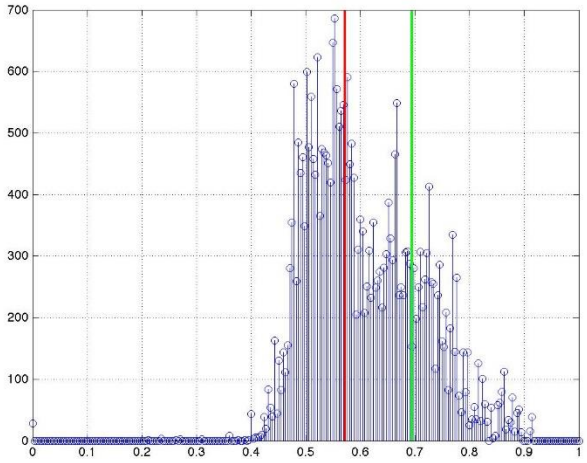

Figure 171 Data cube 6 Detection Results with Threshold 500 (Histogram)

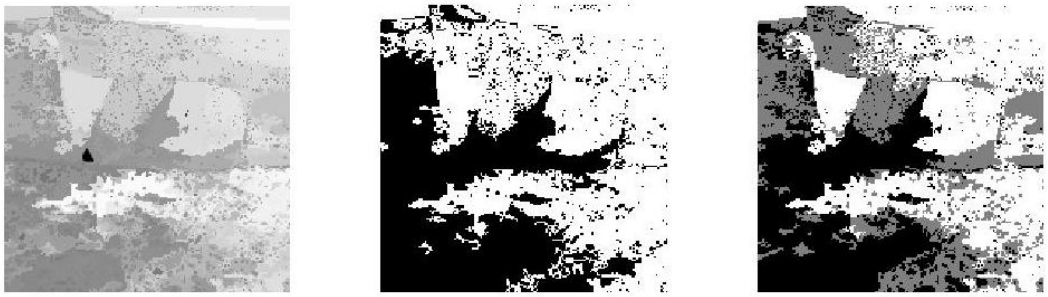

Figure 172 Data cube 6 Detection Results with Threshold 1000 (Otsu)

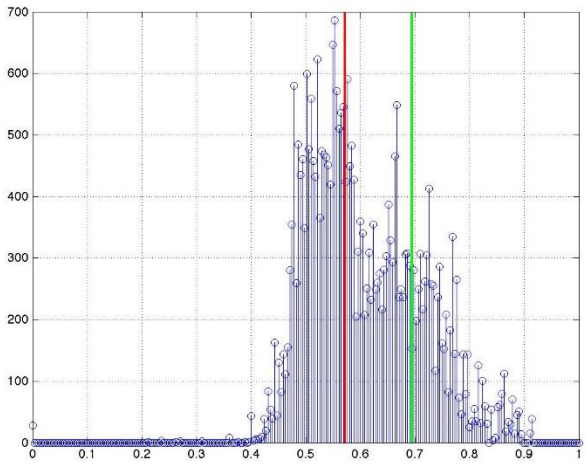

Figure 173 Data cube 6 Detection Results with Threshold 1000 (Histogram)

Algorithm 2

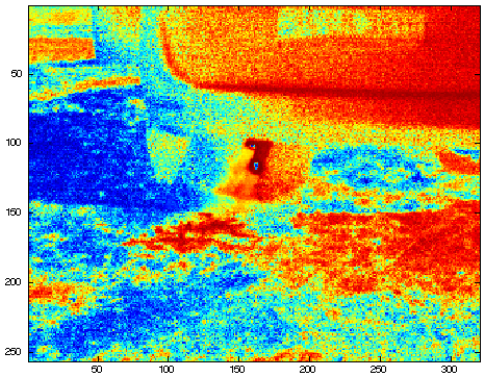

Figure 174 Data cube 6 Detection Results with Algorithm 2

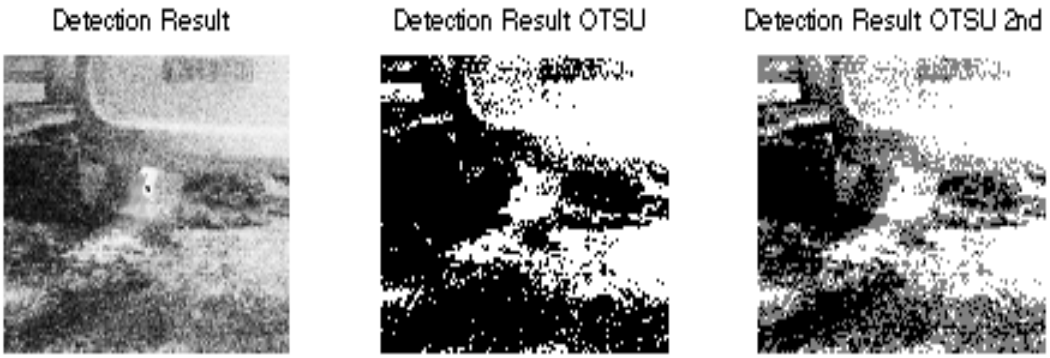

Figure 175 Data cube 6 Detection Results with Algorithm 2 (Otsu)

4.2.6.2.Cropped Target Gas Spectrum

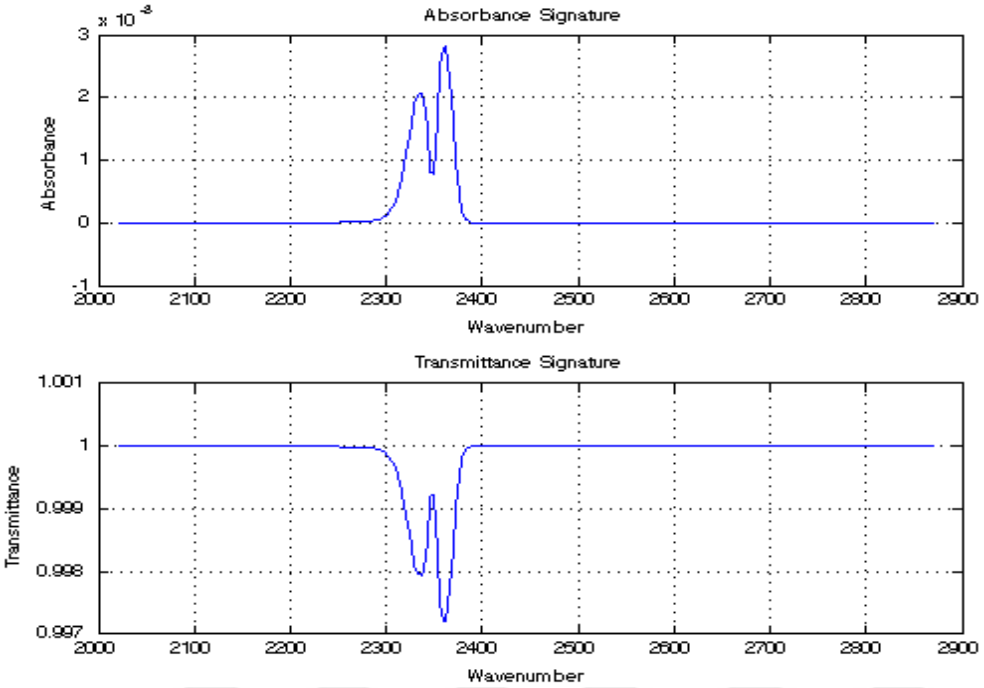

Figure 176 Cropped Target Gas Spectrum

4.2.6.3.Background-Gas Including Pixel Spectrums

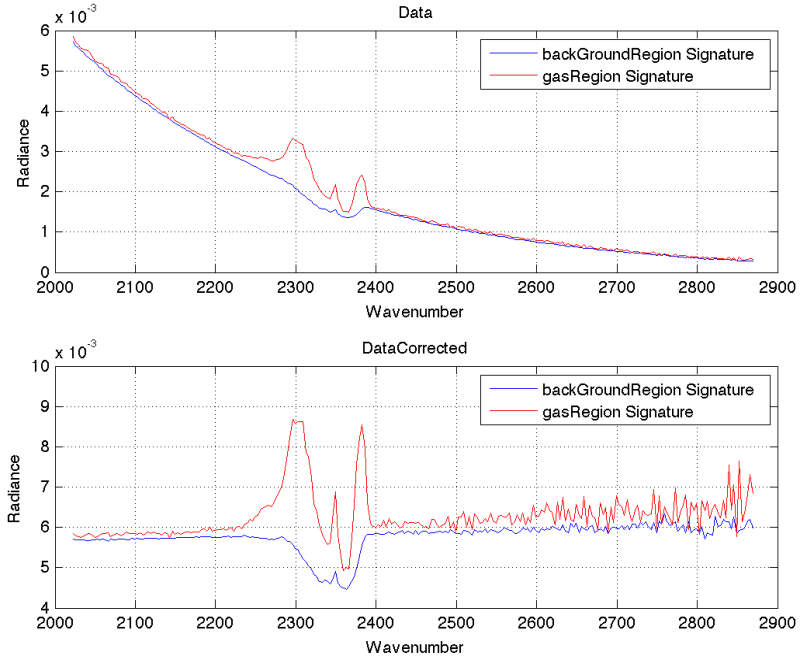

Figure 177 Background&Gas Including Pixel Spectrums

4.2.6.4.Calculated Transmittance and Absorbance Values of Gas Including Pixels

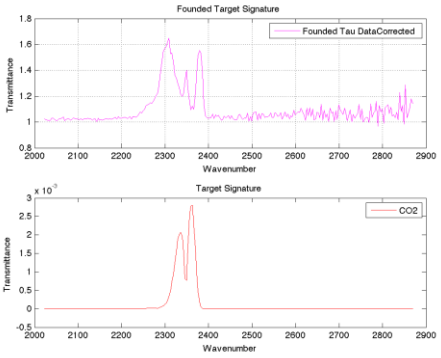

Figure 178 Data cube 6 Calculated Gas Transmittance

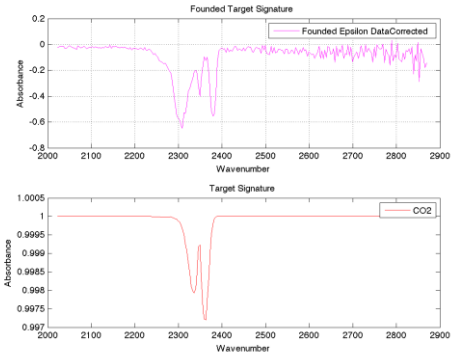

Figure 179 Data cube 6 Calculated Gas Absorbance

CHAPTER 5

CONCLUSION

Target spectral signature for solid and liquids substances are searched on datacubes by resolving the degradation although target gas substances' spectral signatures are not searched directly. The decompositions on the signatures of the materials on the back of the gas are identified in order to determine which gas can cause those decompositions. This decomposition can be in both directions (absorption or emission) according to the temperature differences between gas cloud and background.

It is also possible that this decomposition has a constantly different effect on the same background even if we include the assumption that the temperature of the gases gets equal to the atmospheric temperature as they move away from the source, and that it falls exponentially in its construction as they move away from the source.

In addition, the same gas can be seen on different background signatures in the same scene which makes the problem even more complicated and making it very difficult. Finally, the atmospheric effects are negatively affecting the detection rate as the target gases can be present in atmosphere initially and transmittance of the atmosphere can be very low in the bands that target gases depicts its characteristics.

Although many studies in the literature have mentioned that atmospheric effects are eliminated by various algorithms and that atmospheric effects can be ignored in the near distance, these algorithms require many parameters besides the captured image. For modeling of the atmosphere at the time datacube is obtained, getting the temperature, humidity, gas availability, etc. parameters on the same time has great importance.

In this thesis, as different from studies in the literature a new method is suggested for detection and identification of target gases automatically in hyperspectral imagery without any assumption of variables in the scene or the size/position of plume. Despite previous studies make assumptions about temperature equalities like gas temperature and ambient temperature is equal, we do not deal with this equality by using BB Radiation Curve Compensation algorithm to drop the temperature variables for detecting target gases on image. After this preprocessing step, hierarchical spectral-spatial clustering is implemented to decompose the data into small segments for detection and identification of the plumes if present in the scene. By using all other segments in order to calculate the possible gas transmittance for a segment, we do not deal of separate background and gas regions. It is a fully automatic method to detect gases in the scene. The datacubes are processed with various different gas signatures and it is seen that false alarm rate for detecting the wrong gas in the scene is comparably low.

The other distinguishing specialty is implementing the Otsu thresholding (see (Otsu, 1979)) with 3 level on the resulting detection data which separate data in more than two class in order to get better results. As the first thresholding provide separating the data according to maximum variance difference, second thresholding differentiate gas including region from the background region with high accuracy.

The data set provided by UDI using Telops FTIR Hypercam is used to test the proposed algorithm. Algorithm is implemented on 6 different hyperspectral images. One image

includes methanol gas, one image includes sulfur-ethylene gases mixture, two image includes carbon dioxide gas, one image includes butane gas and last image does not include any gas. One of the other greenhouse gas Nitrous Oxide cannot be tested since we do not have a hyperspectral image including Nitrous Oxide.
Proposed algorithm had prospering and decisive results except carbon dioxide gas. Even though the effect of atmospheric temperature on the hyperspectral image is eliminated by the applied black-body radiation curve compensation algorithm, the temperature difference between the background and the gas temperature still has a great effect on gas detection. Because of this, we consider that the target gas cannot be detected in CO_2 containing image which has a car on the scene in addition the atmospheric transmittance gets nearly zero where CO_2 depicts its characteristics.

5.1. Future Works

As future works, carbon dioxide and other greenhouse gases which is not tested can be studied on new hyperspectral images with various different scene compositions. Also For detection of carbon dioxide, unsupervised atmospheric compensation can be implemented on those hyperspectral images as the major limitation on detecting those gases is atmospheric effects on the data. After atmospheric compensation, quantitative analysis of greenhouse gases on hyperspectral imagery will be conducted.
Also, in order to measure the results metrically, data that has ground truth can be used for getting F-measure results. This can be provided by fully controlled environment and fully controlled oscillation.
For the final detection results we implemented Otsu thresholding twice on detection result data. Another method can be utilized for obtaining more prospering results by testing more hyperspectral images.

REFERENCES

Farley, V., Vallieres, A., Villemaire, A., Chamberland, M., Lagueux, P., & Giroux, J. (2007). Chemical agent detection and identification with a hyperspectral imaging infrared sensor. *Proc. SPIE*, *6739*(418), 1–12. https://doi.org/Artn 66610l\rDoi 10.1117/12.736731

Feinmesser, Y., & Rotman, S. R. (2010). Iterative Approach for Gas Detection and Identification, 73–76.

Gatti, E., & Donati, S. (1971). *Optimum signal processing for distance measurement with lasers. Applied optics* (Vol. 10). https://doi.org/10.1364/AO.10.002446

Hagen, N., & Kudenov, M. W. (2013). Review of snapshot spectral imaging technologies. *Optical Engineering*, *52*(9), 90901. https://doi.org/10.1117/1.OE.52.9.090901

Harig, R., & Matz, G. (2001). Toxic Cloud Imaging by Infrared Spectrometry: A Scanning FTIR System for Identification and Visualization. *Field Analytical Chemistry and Technology*, *5*(1–2), 75–90. https://doi.org/10.1002/fact.1008

Hirsch, E., & Agassi, E. (2010). Detection of gaseous plumes in IR hyperspectral images-performance analysis. *IEEE Sensors Journal*, *10*(3), 732–736. https://doi.org/10.1109/JSEN.2009.2038188

Jähne, B. (1991). *Digital image processing: concepts, algorithms and scientific applications*. *US Patent 6,240,217*. https://doi.org/10.1007/978-3-662-03174-2_13

Kastek, M., Piatkowski, T., & Polakowski, H. (2011). Infrared imaging Fourier-transform spectrometer used for standoff gas detection. *WIT Transactions on Ecology and the Environment*, *147*, 161–172. https://doi.org/10.2495/AIR110151

Kuflik, P., & Rotman, S. R. (2012). Band selection for gas detection in hyperspectral images A . Building a Synthetic Hyperspectral Cube, 2–5.

Manolakis, D., Marden, D., & Shaw, G. a. (2003). Hyperspectral Image Processing for Automatic Target Detection Applications. *Lincoln Laboratory Journal*, *14*(1), 79–116.

Messinger, D. W. (n.d.). Detection of Gaseous Effluents From Airborne Lwir. *Imaging*, 712–723.

Niu, S. (2013). Quantification of Chemical Gaseous Plumes On Hyperspectral Imgery, (August).

Niu, S., Golowich, S. E., Ingle, V. K., & Manolakis, D. G. (2011). Design and evaluation of robust matched filters for chemical agent detection, *8186*(February 2016), 81860R–81860R–10. https://doi.org/10.1117/12.898094

O'Donnell, E. M. (2004). Identification and detection of gaseous effluents from hyperspectral imagery using invariant algorithms. *Proceedings of SPIE*, *5425*, 573–582. https://doi.org/10.1117/12.542426

Omruuzun, F., & Yardimci Cetin, Y. (2015). Endmember signature based detection of flammable gases in LWIR hyperspectral images, *9486*, 948612.

https://doi.org/10.1117/12.2182060
Otsu, N. (1979). A Threshold Selection Method from Gray-Level Histograms. *IEEE Transactions on Systems, Man, and Cybernetics*, *9*(1), 62–66. https://doi.org/10.1109/TSMC.1979.4310076
Planck, M. (1914). The Theory of Heat Radiation. *Search*, *30*, 85–94. https://doi.org/10.1038/123755a0
Pogorzala, D. R. (2004). Gas plume species identification by regression analyses. *Proceedings of SPIE*, *5425*, 583–591. https://doi.org/10.1117/12.541641
Sabbah, S., Harig, R., Rusch, P., Eichmann, J., Keens, A., & Gerhard, J.-H. (2012). Remote sensing of gases by hyperspectral imaging: system performance and measurements. *Optical Engineering*, *51*(11), 111717–1. https://doi.org/10.1117/1.OE.51.11.111717
Sagiv, L., Rotman, S. R., & Blumberg, D. G. (2008). Detection and identification of effluent gases by long wave infrared (LWIR) hyperspectral images. *IEEE Convention of Electrical and Electronics Engineers in Israel, Proceedings*, 413–417. https://doi.org/10.1109/EEEI.2008.4736560
Spisz, T. S., Murphy, P. K., Carter, C. C., Carr, A. K., Vallières, A., & Chamberland, M. (2007). Field test results of standoff chemical detection using the FIRST, *6554*, 655408-655408–12. https://doi.org/10.1117/12.719677
Systems, Measurement, Mariusz Kastek, Tadeusz Piątkowski, P. T. (2011). Infrared Imaging Fourier Transform Spectrometer As The Stand-Off Gas Detection System, *XVIII*(4), 607–620. https://doi.org/10.2478/v10178-011-0058-4.Unauthenticated
Tremblay, P., Savary, S., Rolland, M., Villemaire, A., Chamberland, M., Farley, V., … Padia, T. (2010). Standoff gas identification and quantification from turbulent stack plumes with an imaging Fourier-transform spectrometer. *Proc. SPIE*, *7673*(April), 76730H–76730H–12. https://doi.org/10.1117/12.850127
Vallières, A., Villemaire, A., Chamberland, M., Belhumeur, L., Farley, V., Giroux, J., & Legault, J.-F. (2005). Algorithms for chemical detection, identification and quantification for thermal hyperspectral imagers. *Proceedings of SPIE*, *5995*(418), 59950G–59950G–11. https://doi.org/10.1117/12.632114
Vinh, N. X., & Epps, J. (2010). MinCEntropy: A novel information theoretic approach for the generation of alternative clusterings. *Proceedings - IEEE International Conference on Data Mining, ICDM*, 521–530. https://doi.org/10.1109/ICDM.2010.24
Zhang, R. Z. R., & Rudnicky, a. I. (2002). A large scale clustering scheme for kernel K-Means. *Object Recognition Supported by User Interaction for Service Robots*, *4*, 289–292. https://doi.org/10.1109/ICPR.2002.1047453

APPENDICES

APPENDIX A

GLOSSARY

Radiance:
Radiant intensity measured in a specific direction per unit projected area. Measured in watts/steradian/m2.

Reflectance:
The ratio of a given wavelength of light reflected by a surface to the light incident on a surface, expressed as a percentage.

Blackbody:
Blackbody is a body whose absorbs all radiation incident upon it. Blackbody radiation at a given wavelength depends only on the temperature and a blackbody emits more radiation than any other type of an object at the same temperature;

Planck Function:
Planck Function gives the intensity (or radiance) emitted by a blackbody having a given temperature.

Brightness Temperature:
Brightness Temperature is defined as the temperature of a blackbody that emits the same intensity as measured. For a blackbody: brightness temperature = kinetic temperature (Tb= T)

Transmittance:
The fraction of radiation that remains after the radiation has traveled a certain path in the medium.

Emissivity:
The ratio of the emission of a real body to the emission of the blackbody is called (specific) emissivity ε and depends on the wavelength.

TEZ FOTOKOPİ İZİN FORMU

ENSTİTÜ

Fen Bilimleri Enstitüsü [ ]

Sosyal Bilimler Enstitüsü [ ]

Uygulamalı Matematik Enstitüsü [ ]

Enformatik Enstitüsü [X]

Deniz Bilimleri Enstitüsü [ ]

YAZARIN

Soyadı : GÜR

Adı : Yusuf

Bölümü : Bilişim Sistemleri

TEZİNADI (İngilizce): Detection and Identification of Greenhouse Gases Using Infrared Hyperspectral Imagery

TEZİNTÜRÜ: YüksekLisans [X] Doktora [ ]

1. Tezimin tamamı dünya çapında erişime açılsın ve kaynak gösterilmek şartıyla tezimin bir kısmı veya tamamının fotokopisi alınsın. [X]

2. Tezimin tamamı yalnızca Orta Doğu Teknik Üniversitesi kullancılarının erişimine açılsın. (Bu seçenekle tezinizin fotokopisi ya da elektronik kopyası Kütüphane aracılığı ile ODTÜ dışına dağıtılmayacaktır.) [ ]

3. Tezim bir (1) yıl süreyle erişime kapalı olsun. (Bu seçenekle tezinizin fotokopisi ya da elektronik kopyası Kütüphane aracılığı ile ODTÜ dışına dağıtılmayacaktır.) [ ]

Yazarın imzası ..... Tarih 14 Aralık 2017